**Ph.D. Dissertation of Science**

# Vertical distribution and optical properties of aerosols in a polluted environment (Seoul, Korea) from multiple lidar measurements

다중 라이다 관측을 통한 대기오염지역(서울)의
에어로졸 연직 분포 및 광학 특성 분석

**August 2023**

**School of Earth and Environmental Sciences**
**Graduate School**
**Seoul National University**

**Soojin Park**

# Vertical distribution and optical properties of aerosols in a polluted environment (Seoul, Korea) from multiple lidar measurements

**Supervisor Sang-Woo Kim, Professor**

**Submitting a Ph.D. Dissertation of Science**

**May 2023**

**School of Earth and Environmental Sciences**
**Graduate School**
**Seoul National University**

**Soojin Park**

**Confirming the Ph.D. Dissertation written by**
**Soojin Park**
**July 2023**

| | | |
|---|---|---|
| Chair | Rokjin J. Park | (Seal) |
| Vice Chair | Sang-Woo Kim | (Seal) |
| Examiner | Jhoon Kim | (Seal) |
| Examiner | Byung Gon Kim | (Seal) |
| Examiner | Ali H. Omar | (Seal) |

# Abstract

Accurate simulation of surface air quality and the assessment of the radiative and climate effects of aerosols heavily rely on obtaining information on the vertical distribution of aerosols and their specific optical properties. Due to the substantial variability of aerosol emission sources and the intricate pathways through which aerosols are transported, ground-based remote sensing measurements, such as lidar, have proven to be valuable in capturing continuous, vertically-resolved measurements of the atmosphere. This study investigated the vertical distribution and optical properties of aerosols from multiple ground-based lidar measurements in Seoul, Korea. The classification of aerosols based on lidar measurements has been a persistent challenge when it comes to accurately determining their properties. Consequently, it is crucial to achieve precise aerosol classification in order to obtain accurate aerosol retrievals using remote sensing measurements. The University of Wisconsin-Madison's High Spectral Resolution Lidar (HSRL) measurements during a 23-month deployment, in conjunction with a Mie-scattering lidar situated at Seoul National University (SNU) in Korea were used in this study to calculate the lidar ratio and mass extinction efficiency specific to different types of aerosols.

Surface $PM_{2.5}$ and $PM_{10}$ in-situ measurements from the Sillim

AirKorea site (located 3.6 km from the SNU site) were used to infer the aerosol type: pollution, dust, pollution and dust mixture, and clean. Using the surface PM size distribution information (e.g., $PM_{10-2.5}$ and $PM_{2.5}/PM_{10}$) as references, lidar ratios measured by the HSRL were then classified into each respective aerosol type. The resulting mean lidar ratios of each aerosol type were reported to be 48 sr, 57 sr, 42 sr, and 49 sr for clean continental particles, pollution particles, dust particles, and mixed particles, respectively.

Aerosol extinction coefficients from the Mie-scattering lidar were retrieved by applying the predefined type-specific lidar ratios. The lidar signals were initially classified into different aerosol types based on observations of the range-corrected signal and depolarization ratio. Subsequently, the corresponding lidar ratio values were applied in the calculation of aerosol extinction. A significant improvement in aerosol extinction coefficients was observed compared to the conventional method, which utilizes a single lidar ratio regardless of aerosol type. The new approach reduced errors in aerosol extinction coefficient retrievals by 7 $Mm^{-1}$ when compared to collocated HSRL measurements. This decrease in mean bias of extinction coefficient from -0.026 $km^{-1}$ to -0.019 $km^{-1}$ led to a reduction of 0.042 error in aerosol optical depth (AOD; approximately 10% of the mean AOD in Seoul).

Using the continuous aerosol extinction coefficient observations

from 2-year HSRL measurements, the temporal variability of AOD was investigated and the contributions of boundary layer (BL) and free troposphere (FT) aerosols to AOD were estimated. HSRL AOD showed good agreement with co-located AERONET sun/sky radiometer AOD observations, with a mean bias of -0.00 and an $R^2$ value of 0.87. Nighttime AOD displayed a larger mean and standard deviation (0.45 ± 0.47) than daytime (0.40 ± 0.29). Hygroscopic growth of aerosols under humid conditions was a key factor in the relative enhancement of nighttime AOD. AOD reached its peak at 04 local standard time (LST) and subsequently declined gradually to its minimum at 13 LST. The variation between daytime and nighttime AOD resulted in significant disparities in the daily mean AOD, as observed through 24-hour HSRL measurements and the AERONET sun/sky radiometer's daytime measurements.

Taking advantage of the HSRL's vertically resolved measurements, the contribution of aerosols within the boundary layer (BL) and free troposphere (FT) to AOD and its temporal variation were investigated. Unlike the diurnal AOD variation, AOD within the BL ($AOD_{BL}$) showed closer diurnal variations with the mixing layer height (MLH), displaying lower nighttime values and a peak around 14–15 local standard time. However, the low correlation between MLH and $AOD_{BL}$ ($R^2$ = 0.06) implied that MLH was not the sole deterministic factor of $AOD_{BL}$, and that the day-to-day aerosol concentration within the BL displayed

significantly different temporal variability with the MLH. Although $AOD_{BL}$ was largest around noon, the mean extinction coefficient within the BL ($AOD_{BL}$ divided by MLH) displayed lows during the day, demonstrating the dilution of aerosols due to enhanced turbulent mixing within the mixing layer. The ratio between $AOD_{BL}$ and AOD displayed larger ratios during daytime (42 ± 22%) than nighttime (27 ± 21%).

AOD was largest during summer, followed by spring and fall. Although AOD was the smallest in winter, outlying large AOD values comparable to other seasons were characteristic, implying that although the overall AOD in winter was low, events with AOD values occurred frequently. $AOD_{BL}$ and $AOD_{FT}$ were also larger during summer, which can be attributed to hygroscopic growth of aerosols under high humidity conditions. Larger $AOD_{FT}$ and $AOD_{FT}$-to-AOD ratios during spring coincided with large depolarization ratio values between 2 – 6 km, suggesting the presence of elevated dust layers.

Using the BL mean extinction coefficient and surface $PM_{10}$ concentrations, the mass extinction efficiency (MEE) of aerosols in Seoul was estimated. The $PM_{10}$ MEE showed mean and median values of 5.40 $m^2\ g^{-1}$ and 4.28 $m^2\ g^{-1}$, respectively. MEE displayed significant variability by $PM_{2.5}$-to-$PM_{10}$ ratio, season, ambient relative humidity, and aerosol type. MEE of dust and mixed aerosols displayed a weak correlation with RH, while pollution and clean aerosol MEEs displayed a strong

correlation with increasing RH. The uncertainty of estimated surface $PM_{10}$ concentrations was minimized when the aerosol type-specific, RH-dependent MEE values were used (the mean normalized bias decreased from 10.6% when using a single MEE value, to 3.5%). Using the presented look-up table of aerosol type and RH-specific MEE values, the monthly profiles of $PM_{10}$ concentration were retrieved. Unlike the seasonality of the aerosol extinction coefficients, $PM_{10}$ concentration was largest during spring, demonstrating the differences between aerosol optical properties and mass concentrations.

**Keywords:** High spectral resolution lidar (HSRL), Mie-scattering lidar, lidar ratio, mass extinction efficiency (MEE), particulate mass (PM) concentration

**Student Number:** 2017-34942

# Table of Contents

**Abstract** ..... i

**Table of Contents** ..... vii

**List of Tables** ..... ix

**List of Figures** ..... x

**Chapter 1 Introduction** ..... **1**

1.1 Background and Motivation ..... 1

1.2 Scientific Questions ..... 5

1.3 Objectives of this study ..... 8

**Chapter 2 Instrumentation and Data** ..... 11

2.1 Mie-Scattering Lidar ..... 11

2.2 High Spectral Resolution Lidar ..... 12

2.3 AERONET sun/sky radiometer ..... 14

2.4 Ground-based in-situ measurements ..... 15

**Chapter 3 Retrieval of aerosol extinction coefficient from Lidar measurements** ..... 17

3.1 Aerosol-type-specific lidar ratio for typical aerosol types in Seoul ..... 19

3.2 Improvement of Mie-scattering lidar extinction coefficient retrievals using type-specific lidar ratios ..... 30

**Chapter 4 Diurnal variation of boundary layer and free troposphere aerosol optical depth** ..... 41

4.1 Diurnal variation of AOD ..... 43

4.2 Boundary layer (BL) versus free troposphere (FT) AOD..... 52

**Chapter 5 Aerosol mass concentration profiles from Lidar measurements** ..... 77

5.1 Mass extinction efficiency from lidar and in-situ measurements ..... 79

5.2 Estimating surface PM mass concentration from lidar observations..... 85

**Chapter 6 Summary and further directions** ..... 95

**References** ..... 101

국문 초록 ..... 123

# List of Tables

**Table 3.1** Type-specific lidar ratios defined from HSRL measurements classified into each aerosol type based on HSRL $\beta$ and dpr observations. ..... 27
**Table 3.2** Type-specific lidar ratios defined from HSRL measurements classified into each aerosol type based on collocated surface PM observations. ..... 27
**Table 5.1** Look-up table of the MEE of $PM_{10}$ specified by aerosol type and ambient RH conditions. ..... 84

# List of Figures

**Figure 2.1** Geological location of Seoul National University (SNU), Sillim ground station, and Jungnang sites in Seoul, Korea..... 12
**Figure 3.1** Scatterplot and probability density functions of $PM_{2.5}$ to $PM_{10}$ ratio (x-axis) and $PM_{10\text{-}2.5}$ concentration (y-axis). ..... 23
**Figure 3.2** Scatterplot and probability density functions of HSRL $\beta$ and dpr measurements by aerosol type, determined using collocated surface PM observations. The whiskers indicate one standard deviation of each variable..... 25
**Figure 3.3** Flowchart of the HSRL aerosol type classification scheme. ..... ..... 26
**Figure 3.4** Global aerosol lidar ratios for representative aerosol types published in previous studies. Lidar ratios from HSRL measurements in this study are plotted in red. ..... 29
**Figure 3.5** Flowchart of the Mie-scattering lidar aerosol type classification scheme..... 31
**Figure 3.6** (a) Time-height plots of Mie-scattering lidar range-corrected signal, (b) time-height plots of Mie-scattering lidar depolarization ratio, and (c) time-height plots of the aerosol type index for 13 to 15 April 2016..... 33
**Figure 3.7** (a) Profile of the number of data points by aerosol type during March 2016 – January 2018. (b) Frequency of each aerosol type by height within the boundary layer. ..... 34
**Figure 3.8** Same as Figure 3.7 but by season. ..... 35
**Figure 3.9** (a) Time-height plot of Mie-scattering lidar extinction coefficient calculated using aerosol type-specific lidar ratios ($\sigma_{ext}^{Mie-type}$). (b) Time-height plot of aerosol types. (c) Profile of the bias between $\sigma_{ext}^{Mie-type}$ and single lidar ratio calculated $\sigma_{ext}$ ($\sigma_{ext}^{Mie-single}$) for 18 LST 13 April to 6 LST 14 April 2016. (d) same as (c) but for 21 LST 14 April to 9 LST 15 April 2016. (e) same as (c) but for 12 to 23 LST 15 April 2016. Differences in lidar ratio are overplotted in red in (c), (d), and (e)..... 39
**Figure 3.10** (a) Scatterplot of HSRL $\sigma_{ext}$ (x-axis) and $\sigma_{ext}^{Mie-singl}$ (y-axis). (b) Scatterplot of HSRL $\sigma_{ext}$ (x-axis) and $\sigma_{ext}^{Mie-type}$ (y-axis). Data period is from March 2016 to January 2018.....

..... 40
**Figure 4.1** Scatterplot of simultaneous AERONET (x-axis) and HSRL (y-axis) AOD at 532 nm. ..... 46
**Figure 4.2** Diurnal variation of HSRL (red diamond) and AERONET (blue circle) AOD at 532 nm. Solid markers indicate the mean AOD and one standard deviation from the mean is shaded in the background. Light bar graphs on the top depict the number of data points. ..... 47
**Figure 4.3** The distribution of data frequency and hourly $AOD_{HSRL}$ binned by each RH decile: (a) the relationship of AOD with surface-level RH, (b) the relationship of daytime AOD with surface-level RH, and (c) the relationship of nighttime AOD with surface-level RH. Whiskers indicate the 5 and 95 percentile values; boxes indicate 25, 50, and 75 percentile values, and the markers indicate mean values. AODs for RH $\geq$ 90% conditions (dashed lines) were excluded from the regression between AOD and RH due to the scarcity of data. ..... 49
**Figure 4.4** Diurnal variation of HSRL (red diamond) and AERONET (blue circle) AOD at 532 nm by season. Solid markers indicate the mean AOD while one standard deviation from the mean is shaded in the background. ..... 50
**Figure 4.5** Scatterplot of AERONET daily AOD mean (y-axis) with HSRL daily mean AOD calculated using (a) temporally-collocated AOD measurements, (b) daytime AOD measurements, and (c) 24-hr AOD measurements. ..... 51
**Figure 4.6** Profiles of (a) aerosol lidar range-corrected backscattered signal (arbitrary units), (b) covariance transform applied to the lidar signal, (c) WDL vertical wind speed standard deviation ($\sigma_w$), and (d) radiosonde potential temperature at 15 LST on 5 October 2016. The horizontal dashed lines represent the MLH determined from each measurement profile. ..... 58
**Figure 4.7** Time-height plots for (a) lidar range-corrected lidar backscattered signals, (b) ceilometer backscattered signals, and (c) vertical wind speed standard deviation ( $\sigma_w$ ) measured from WDL at the Jungnang site on 6 October 2016; MLH values from each instrument are plotted in white squares. Potential temperature profiles (solid black line)

from radiosonde soundings are superimposed at the corresponding flight times and $MLH_{sonde}$ (horizontal dashes) in (a)..... 60
**Figure 4.8** Time-height plots for (a) horizontal wind speed, (b) vector wind shear, and (c) vertical wind speed measured from WDL at the Jungnang site on 6 October 2016..... 61
**Figure 4.9** (a, b) Time–height plots of aerosol $\beta$ signal and $MLH_{lidar}$. (c, d) Time–height plots of $\sigma_w$ and $MLH_{WDL}$. Lidar and WDL measurements from the SNU site. (e, f) Time-height plots of $PM_{2.5}$ concentration from WRF-Chem simulations with MLH. (g, f) Time series of $PM_{2.5}$ concentrations using ground-based measurements from the Sillim site and WRF-Chem simulations for 12 May 2016 (a, c, e, g) and 18 May 2016 (b, d, f, h)..... 62
**Figure 4.10** (a) Time-height plots of HSRL backscatter coefficient overplotted with MLH (magenta) and CBH (white). (b) $AOD_{BL}$ and $AOD_{FT}$ timeseries, (c) Contribution of BL and FT aerosols to AOD. Left and right columns are for July 8 to 9 2016 and October 20 to 21 2017 cases, respectively..... 69
**Figure 4.11** (a) Diurnal variation of aerosol extinction coefficient by height overplotted with hourly mean MLH. (b) Diurnal variation of $AOD_{BL}$ and $AOD_{FT}$ retrieved from HSRL measurements (left y-axis) and hourly mean MLH and one standard deviation (right y-axis)..... 72
**Figure 4.12** (a) Monthly variation of aerosol extinction coefficient by height overplotted with monthly mean MLH and (b) Monthly variation of $AOD_{BL}$ and $AOD_{FT}$..... 74
**Figure 4.13** Monthly mean profiles of HSRL depolarization ratio (532 nm)..... 75
**Figure 4.14** (a) Scatterplot of AOD with $PM_{2.5}$ mass concentration scaled within the ML. (b) Scatterplot of $AOD_{BL}$ with $PM_{2.5}$ mass concentration scaled within the BL..... 76
**Figure 5.1** Histograms of (a) $PM_{10}$ MEE, (b) aerosol type-specific $PM_{10}$ MEE, (c) $PM_{10}$ MEE by $PM_{2.5}$ to $PM_{10}$ ratio, and (d) $PM_{10}$ MEE by season..... 82
**Figure 5.2** The distribution of data frequency and $PM_{10}$ MEE binned by each RH decile by season. All box plots are color-coded by RH conditions. Whiskers indicate 5 and 95 percentiles, boxes

indicate 25, 50, and 75 percentiles and markers indicate the mean MEE values. ..... 83
**Figure 5.3** The distribution of data frequency and $PM_{10}$ MEE binned by each RH decile by aerosol type. All box plots are color-coded by RH conditions. Whiskers indicate 5 and 95 percentiles, boxes indicate 25, 50, and 75 percentiles and markers indicate the mean MEE values. ..... 84
**Figure 5.4** (a) Observed (x-axis) and estimated (y_axis) $PM_{10}$ concentration using a single MEE value; (b), (c), (d), (e), and (f) the same as (a) except the y-axis indicates estimated $PM_{10}$ concentration using MEE values depending on season, RH, seasonal RH, type, and type-RH, respectively. ..... 86
**Figure 5.5** Time-height plots of estimated $PM_{10}$ concentrations from HSRL observations during 13 – 15 April 2016. CBHs and MLHs are overplotted in white and magenta, respectively..... ..... 89
**Figure 5.6** Monthly variation of (a) estimated $PM_{10}$ concentration profiles and (b) extinction coefficient profiles from HSRL observations from March 2016 to January 2018. ..... 91
**Figure 5.7** Monthly mean surface $PM_{10}$ (in black) and $PM_{2.5}$ (in red) observed by ground in-situ measurements from the AirKorea Sillim site in Seoul. Dotted black lines represent the one standard deviation from the means. ..... 92

# Chapter 1 Introduction

## 1.1 Background and Motivation

Atmospheric aerosols are of significant environmental importance because of their effects on air quality, as well as their ability to alter Earth's radiation budget, by contributing to both surface cooling and atmospheric warming by scattering and absorbing solar radiation (Myhre et al., 2013; Allen et al., 2016). Enhanced light scattering and absorption by aerosols have a negative impact on atmospheric visibility and can also stabilize the atmosphere, resulting in the inhibition of cloud formation (Ramanathan et al., 2001).

The vertical distribution of aerosols is an important factor in determining the surface air quality not only in the pollution sources but also in downwind receptor regions (Hung et al., 2020; Lee H. et al., 2019). The direct and indirect radiative effects of aerosols are also strongly dependent on the height of aerosols layers (Gonçalves et al., 2015; Marinescu et al., 2017; Tian et al., 2020). Light absorbing aerosols distributed in the upper atmosphere can increase the atmospheric stability by increasing the atmospheric temperature in the upper layer and decreasing the solar radiation reaching the surface (Dong et al., 2017). Aerosol radiative effects varying by height can in turn affect the vertical distribution and transport pathways of aerosols. Won et al. (2004)

reported that the heating rate in an elevated dust layer advected out of the planetary boundary layer can increase the static stability of the atmosphere which helps maintain the structure of the dust layer for longer periods during its advection.

Meanwhile, due to their diverse emission sources, transport pathways, and relatively short lifetimes, the distribution of aerosols shows great heterogeneity, not only in the horizontal but also in the vertical (Reid et al., 2017; Winker et al., 2013). Therefore, measurement-based information on the vertical distribution of aerosols in diverse regions is necessary for an accurate understanding of the aerosol radiative and health effects. Light Detecting and Ranging (Lidar) instruments provide accurate vertical profiles of aerosol extensive and intensive properties by probing the atmosphere (Ansmann and Müller, 2005; Rogers et al., 2014). Since its launch in 2006, the CALIOP sensor on board CALIPSO is probing the atmosphere and processing profiles of aerosol backscatter, extinction, and optical depth in its path (Winker et al., 2009). Along with CALIPSO, many ground stations equipped with lidars offer continuous observations for information on the vertical aerosol properties of various regions and validation of CALIPSO (Chaikovsky et al., 2016; Papagiannopoulos et al., 2016). Moreover, networks of ground lidar stations around the globe have emerged that aim to provide long-term and continuous observations of large spatial

coverage. The NASA Micro-Pulse Lidar Network (MPLNET) has sites around the globe providing column and vertically resolved aerosol and cloud data (Welton et al., 2021). The European Aerosol Research Lidar Network (EARLINET) covers most parts of Europe with multiwavelength Raman lidar stations (Pappalardo et al., 2014). In Asia, the Asian Dust and Aerosol Lidar Observation Network (AD-Net) targets dust and aerosols in East Asia using polarization-sensitive multi-wavelength Mie-scattering lidars (Nishizawa et al., 2016). While satellite and ground station networks are contributing to global coverage of atmospheric observations, obtaining accurate measurements of the vertical structure of aerosol optical properties is still an ongoing project (Berjón et al., 2019; Painemal et al., 2019).

As an active remote sensing instrument, lidars not only provide vertically-resolved measurements of the atmosphere but also are capable of producing stable nighttime observations. Although it can be perceived that nighttime air quality is better than daytime due to decreased human activity and lower anthropogenic emissions, recent studies have pointed out the deterioration of air quality in the evening hours (Manning et al., 2018). It has been reported that the nighttime chemistry of NOx and ozone is very different from that during daytime (Wang et al., 2023) and that active condensation of organic vapors on particulate matter can result in severe nighttime haze events in heavily polluted regions (Mishra

et al., 2023). The complexity of nighttime chemistry has introduced difficulties in setting regulations for air quality, calling for the need for nighttime measurements of pollutants in regions that require mitigation of atmospheric pollution (Jo et al., 2019).

South Korea is located within the downwind region of the Asian continent and is subject to transboundary transport of aerosols and pollutants due to prevailing Westerlies (Al-Saadi et al., 2015; Kim S. et al., 2014; Peterson et al., 2019). Air quality in the country's capital, Seoul, is the result of a complex interplay between the governing synoptic meteorology, local emissions and transboundary transport of pollutants (Jeon et al., 2019; Kim et al., 2007b; Lee S. et al., 2021). With increasing public awareness of air quality, understanding aerosol dynamics in Korea and its leeward regions is necessary for effective mitigation and accurate modeling of air quality (Lee S. et al., 2019; Lennartson et al., 2018). Although it is well recognized that the vertical structure of aerosol layers above source areas and its downwind areas are important factors in the determination of surface concentration, the vertical structure and mixing status of aerosols are poorly understood due to the lack of long-term vertical measurements in Korea (Lee H. et al., 2019).

During May and June 2016, an international collaboration between Korea and the US to study air quality was executed through the Korea-United States Air Quality Study (KORUS-AQ; Al-Saadi et al., 2015), a field

study performing comprehensive measurements of pollutants with the participation of measurements and modeling experts. From March 2016 to February 2018, the University of Wisconsin-Madison High Spectral Resolution Lidar (HSRL) was deployed on the campus of Seoul National University (SNU) as a part of the KORUS-AQ campaign, where continuous AERONET and Mie-scattering lidar measurements have been in place since 2002 and 2006, respectively. Co-located measurements of the HSRL with the Mie-scattering lidar and AERONET can be a perfect testbed for inter-comparison and improvement of existing issues in the Mie-scattering lidar aerosol extinction coefficient retrieval methods, which will be re-visited in each chapter of this draft.

## 1.2 Scientific Questions

The above background leads to several scientific questions to be studied. Specific scientific questions that will be answered through this study are as follows:

(1) What are the lidar ratio values for aerosols observed in Seoul, and how can they be used to further improve Mie-scattering lidar retrievals of aerosol extinction coefficients?

Elastic backscatter lidars require an *a priori* lidar ratio (i.e., extinction-to-backscatter ratio) value or other means of measurement defining the transmittance of the layer of interest to use as a constraint.

Many previous studies have reported the lidar ratio values for various aerosol types in a variety of locations using methods ranging from in-situ to satellite measurements and models. Although an average bulk lidar ratio value for aerosols has been reported in Kim et al. (2015) and Yeo et al. (2016), an intensive investigation of the lidar ratios of the representative aerosol types observed in Seoul is long overdue.

How lidar ratios are applied to the attenuated backscatter signals of the Mie-scattering lidar is also critical in retrieving accurate extinction coefficients. Assuming a single lidar ratio for a whole column can lead to discrepancies from the true state if the column consists of layers of different aerosol types. Misclassification of aerosol types when applying type-specific lidar ratios can also lead to errors in the extinction coefficient. Therefore, even with the most accurate lidar ratios prepared for use as priori inputs, attention in the calculating processes is required.

(2) What are the characteristics of the diurnal (24-hr) variability of vertically-resolved AOD in Seoul?

In validating aerosol extinction coefficient retrievals, previous studies have had to verify their results by integrating their extinction values and comparing them with well-established AOD measurements (i.e., AERONET, MODIS). However, column AOD values not only partly confirm the accuracy of extinction coefficient retrievals, but also most

remote sensing of AOD only offer measurements during the day.

The HSRL not only provides relatively sound measurements of extinction coefficient profiles, that can be used directly in the verification of Mie-scattering lidar retrievals, but it also provides continuous 24-hr measurements of AOD. Although AERONET and other satellite measurements are making progress in developing methods to retrieve nighttime AOD, they are still on-going projects that are also in need of data sets to use in their validation processes.

Analyses on the 24-hr variation of AOD is also of great interest since it will provide insight on the diurnal behaviour of aerosols, preconvection, prephotochemistry effects, nocturnal mixing layer dynamics, and nighttime aerosol outbreaks. Accounting for the contribution of aerosols within the planetary boundary layer and the free troposphere on the total column AOD is also of interest due to its varying dynamics.

(3) How accurately can PM concentration be estimated using remote sensing measurements?

While the aerosol extinction coefficient is useful when investigating visibility and aerosol radiative effects, the aerosol mass concentration is of great interest due to the demand of accurate air quality modeling considering the increasing interest in health effects of aerosols and air quality. Although ground stations measuring PM concentrations in

populated regions of Korea provide good spatial coverage, the vertical distribution of PM concentrations is essential to validate the vertical advection and transport of elevated aerosols.

Recent studies are trying to measure $PM_{2.5}$ concentrations based on satellite AOD, which will allow us to get global information on surface $PM_{2.5}$ concentrations. Although lidars do not have good spatial coverage, developing an accurate retrieval method for $PM_{2.5}$ with lidar will provide valuable data that can be used for the validation and improvement of air quality models and satellite-based estimates of PM concentration.

## 1.3 Objectives of this study

To answer these scientific questions, the overall goal of this study is to investigate the vertical distribution and optical properties of aerosols in Seoul, Korea using multiple lidar measurements.

The specific objectives of this study are the following:

(1) to distinguish aerosol types based on their intensive optical properties measured by multiple lidar instruments and define a representative lidar ratio value for each aerosol type.

(2) to improve the extinction coefficient retrievals from Mie-scattering lidar observations using type-specific lidar ratio values and validate the results with other well-established sensors.

(3) to investigate the diurnal/monthly variation of aerosol optical

properties (i.e., extinction coefficient, AOD, etc.) and the contribution of boundary layer and free tropospheric aerosols to total column properties.

(4) to define the mass extinction efficiency of aerosols by type and investigate their relationship with other atmospheric conditions.

(5) to compare near surface aerosol mass concentrations from remote sensing measurements with ground-level in-situ PM measurements.

(6) to estimate aerosol mass concentration profiles over Seoul from aerosol extinction profiles and type-specific mass extinction efficiency values.

# Chapter 2 Instrumentation and Data

## 2.1 Mie-Scattering Lidar

The Light Detection and Ranging (Lidar) measures the backscattered laser energy from aerosols elevated within the path of the laser beam to observe the vertical structure of aerosols in the atmosphere. The signal measured by a Mie-scattering lidar can be expressed with aerosol optical properties in the form of the lidar equation (equation (1); Fernald, 1984; Klett, 1981).

$$\mathrm{P(r)} = P_0 \eta \frac{A}{r^2} \mathrm{O(r)} \frac{ct}{2} \beta(\mathrm{r}) \exp\left[-2 \int_0^r \sigma(r')dr'\right] \quad (1)$$

where P(r) and $P_0$ are power received from range r and power transmitted by the lidar, respectively, η, the receiver efficiency, A, the receiver area, O(r), the receiver field of view overlap function, c, the speed of light, t, the laser pulse duration, $\beta$(r), the atmospheric backscatter coefficient, and $\sigma$(r), the atmospheric extinction coefficient.

The Mie-scattering lidar has been making measurements at Seoul National University (SNU) since its deployment in March 2006 (**Figure 2.1**). It was developed and installed by the National Institute for Environmental Studies (NIES, Japan) and uses an Nd:YAG laser at 532 nm and 1064 nm with polarization measurement at 532 nm. It makes

measurements for 5 minutes and rests for 10 minutes, resulting in a temporal resolution of 15 minutes while its vertical resolution is 6 m (Kim et al., 2011; 2015).

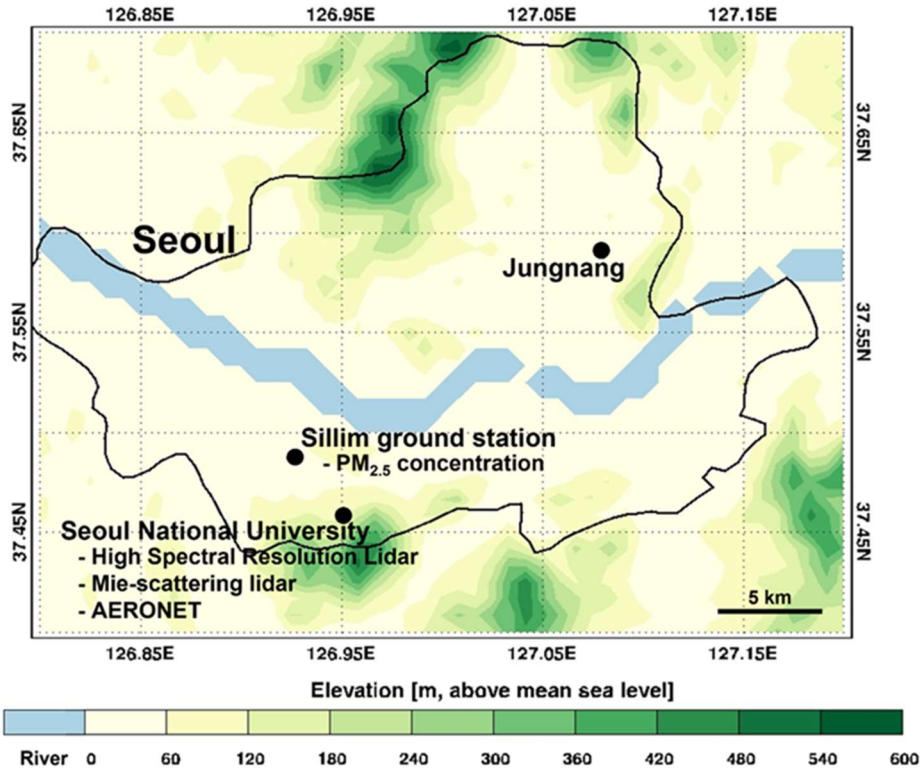


**Figure 2.1** Geological location of Seoul National University (SNU), Sillim ground station, and Jungnang sites in Seoul, Korea.

## 2.2 High Spectral Resolution Lidar

The High Spectral Resolution Lidar (HSRL) differs from other elastic backscatter lidars in that it uses iodine filters to measure incoming signals backscattered from molecules, and particles (aerosols),

separately (Eloranta, 2014). This allows the backscatter and extinction coefficients within the lidar equation to be retrieved without the need to pre-define a lidar ratio or some other type of measurement to use as a constraint as is required for standard elastic backscatter lidar (i.e., Mie-scattering lidar) retrievals.

Similar to the Mie-scattering lidar, the signal measured by the HSRL can be expressed by the lidar equation. However, unlike the Mie-scattering lidar, due to its iodine filters, there are two lidar equations (equations (2) and (3)).

$$P_m(r) = P_0 \eta \left(\frac{A}{r^2}\right) O(r) \left(\frac{ct}{2}\right) \beta_m(r)\, exp\left[-2 \int_0^r \sigma(r')dr'\right] \qquad (2)$$

$$P_a(r) = P_0 \eta \left(\frac{A}{r^2}\right) O(r) \left(\frac{ct}{2}\right) \beta_a(r)\, exp\left[-2 \int_0^r \sigma(r')dr'\right] \qquad (3)$$

where all variables are the same as in equation (1), but the lower subscripts m and a mean molecular and aerosol, respectively.

Dividing equation (2) by equation (3), it is possible to express the aerosol backscatter coefficient in terms of the molecular backscatter coefficient. Because the molecular backscatter coefficient is solely proportional to atmospheric density, the $\beta_m$(r) term in equation (2) is retrievable using temperature and pressure profiles from sounding measurements (Eloranta, 2014; Phillips, 2019).

The aerosol extinction coefficient can be derived by taking the log of

equation (2) and differentiating with respect to range (equation (4)).

$$\sigma(r) = \frac{1}{2}\frac{\partial}{\partial r}\log O(\mathrm{r})\frac{\frac{\eta c t A}{2r^2}\beta_m(r)}{P_m(r)} \quad (4)$$

The University of Wisconsin-Madison HSRL system was deployed at SNU from March 2016 to February 2018 as a part of the KORUS-AQ campaign. It was housed in a temperature and humidity-controlled container on the roof of the Natural Sciences building and made continuous measurements for almost two years. The HSRL system also provides the depolarization ratio at 532 nm wavelength and molecular and particulate backscatter coefficients at 1064 nm wavelength. The data can be accessed through the University of Wisconsin – Madison HSRL Data Archive (hsrl.ssec.wisc.edu, last accessed 18 July 2023) and can be processed to time resolution ranging from 0.5 seconds to 12 hours and vertical resolution ranging from 7.5 meters to 1200 meters.

## 2.3 AERONET sun/sky radiometer

Column integrated AOD measurements from ground-based sun/sky radiometer were used in this study for the evaluation of the HSRL's extinction coefficient retrievals. The Aerosol Robotic Network (AERONET; Holben et al., 1998) provides highly accurate, ground-truth measurements of AOD from Cimel sun/sky radiometers that are

automatically cloud screened and quality checked for instrument anomaly. The typical uncertainty of AERONET AOD is estimated to be from 0.01 to 0.02 (Eck et al., 1999). Specifics on the most recently released V3 algorithm are published in Giles et al. (2019). The AERONET makes routine measurements of direct Sun every 15 minutes at 340, 380, 440, 500, 675, 870, 940, and 1020 nm wavelengths. In this study AERONET V3 Level 2 AOD was used, indicating that the data was cloud-screened and quality-assured (Smirnov et al., 2000), with uncertainty to be reported from 0.01 to 0.02 (Giles et al., 2019).

## 2.4 Ground-based in-situ measurements

Surface $PM_{2.5}$ and $PM_{10}$ concentration measurements from the nationwide air pollution monitoring network (AirKorea; www.airkorea.or.kr, accessed 17 April 2023) and obtained at the Sillim site (126.93 E, 37.49 N, 24 m above sea level) located 3.6 km from SNU, and 0.08 km lower in elevation (**Figure 2.1**), were used. The Ministry of Environment of Korea provides quality-assured and controlled measurements of $PM_{2.5}$ and $PM_{10}$ hourly concentration with uncertainty levels of 1 μg $m^{-3}$ (Ministry of Environment of Korea and National Institute of Environmental Research, 2022). RH data were obtained from the ground-based Automated Synoptic Observing System (ASOS) operated by the Korea Meteorological Administration (KMA), with

measurement uncertainty ranging within $\pm$ 3% ($\pm$ 5% for RH $\geq$ 91%; KMA, 2022). The ASOS provides temperature, RH, pressure, precipitation, and visibility measurements that are accessible via the Open MET Data Portal of KMA (https://data.kma.go.kr, accessed 18 July 2023).

# Chapter 3 Retrieval of aerosol extinction coefficient from Lidar measurements

Aerosol extinction coefficients are calculated from lidar measurements by solving the lidar equation using a priori lidar ratio value or using transmittance measurements as a constraint (Young and Vaughan, 2009). Errors in extinction coefficient are mainly attributable to either mistyping of aerosol layers, or errors in the lidar ratios (Rogers et al., 2014; Young et al., 2018). Lidar ratio for tropospheric aerosols vary over a wide range (from 20 to 100 sr) depending on aerosol size, shape and composition (Anderson et al., 2000; Ferrare et al., 2001). Consideration of the regional variations of aerosol subtype and lidar ratio values are essential for accurate retrieval of aerosol backscatter and extinction coefficients from lidar (Hofer et al., 2017; Kim et al., 2020). Choice of the aerosol type and the corresponding lidar ratio is reported to have substantial effect on the consequent extinction coefficient and AOD retrievals. Winker et al. (2009) presented the optical depth error ($\Delta\tau$) resulting from an error in lidar ratio $\Delta S$ as the following equation:

$$\Delta\tau = \frac{0.5 * (e^{2\tau} - 1)\Delta S}{S} \tag{5}$$

from which it can be concluded that while the relative error in optical

depth is proportional to the relative error in the lidar ratio for small optical depths, the relative error becomes very sensitive to lidar ratio uncertainties when AOD exceeds unity. For a case study validating CALIPSO AOD with overlapping airborne HSRL AOD measurements in Rogers et al. (2014), specified lidar ratio values 45% larger than the observed lidar ratios from the HSRL resulted in a 65% overestimation of AOD by CALIPSO. Therefore, determining accurate lidar ratios for various aerosol types in different regions has been a continuous task not only in-situ field measurements, but also using remote sensing measurements (Flousti et al., 2023; Schuster et al., 2022).

With the measurement of the molecular backscatter channel in the HSRL, the backscatter and extinction coefficient are retrievable without the need for a lidar ratio or transmittance measurements (Eloranta, 2014). Although the University of Wisconsin-Madison HSRL system made successful measurements during its deployment in Seoul, with the end of its mission, we are left with the controversial method of using the Mie-scattering lidar for retrieving continuous near-real time measurements of aerosol extinction coefficient. Therefore, the HSRL measurements during its deployment in Seoul was used to improve and expand the extinction coefficient retrieval methods used with the Mie-scattering lidar. Although an algorithm has been implemented to retrieve extinction profiles from the Mie-scattering lidar in Kim et al. (2015) and

Yeo et al. (2016), a single lidar ratio value is used in their algorithm despite the diversity of aerosol types and complexity of its vertical distribution observed in Seoul. Therefore, application of type-specific lidar ratio values to the Mie-scattering lidar measurements and an intensive comparison of its retrievals with direct measurements of extinction coefficient is called for.

Classifying lidar signals into the correct aerosol type will be of great importance not only in applying lidar ratios in the extinction retrieval process, but also in the actual determining of lidar ratio values from observations. Therefore, developing an effective and accurate algorithm for the classification of lidar signals into their corresponding aerosol types should proceed. Therefore, in efforts to improve the extinction coefficient retrieval algorithm using Mie-scatter lidar measurements, the enhancement was carried out in two steps: first, to determine the lidar ratio values for aerosols mainly observed in Seoul, and second, to improve the application method lidar ratio values in the calculation process of the algorithm.

## 3.1 Aerosol-type-specific lidar ratio for typical aerosol types in Seoul

Lidar ratios can be retrieved using simultaneous observations of attenuated backscatter from lidar and total column aerosol optical depth

from sky radiometer measurements (Kim et al., 2015; 2020). It can also be directly calculated by taking the ratio of extinction coefficient to backscatter coefficient if direct measurements of both parameters are available. While both methods are subject to errors in the input data, the former method is also limited in that it can only retrieve lidar ratios representing the total column aerosols, and only when transmittance measurements are available. Using the extinction ($\sigma_{ext}$) and backscatter ($\beta$) coefficients measured by the HSRL, lidar ratio values were retrieved for typical aerosol types observed in Seoul.

Using a decision tree with specifications on aerosol optical properties as thresholds is a commonly used method (Omar et al., 2009; Kim et al., 2015, 2018; Yeo et al., 2016; Tesche et al., 2009). Here, a common way to define the threshold values is through intensive measurement campaign data focused on specific aerosol types. Using a decision tree for aerosol classification can be controversial since classification results may vary depending on the logical order in which parameters are used to filter out data threads, and the threshold value of the determining variable. Alternatively, using a means of distance metrics with model values for various parameters that represent each aerosol type will eliminate the possibility of errors due to the decision tree construction. Burton et al. (2012) introduced an aerosol classification method using four intensive aerosol optical properties (lidar ratio,

depolarization ratio at 532 nm, backscatter ratio between 1064 nm and 532 nm, spectral depolarization ratio) through which aerosol observations gathered from airborne HSRL measurements throughout the US were classified into ice, pure dust, dusty mix, maritime, polluted maritime, urban, fresh smoke, and smoke.

The air quality in Seoul, South Korea, results from a complex interplay between the governing synoptic meteorology, local emissions, and transboundary transport of pollutants (Jeon et al., 2019; Jordan et al., 2020; Kim et al., 2007b; Kim et al., 2022; Lee G. et al., 2021). Several studies from the joint Korea-United States Air Quality Study (KORUS-AQ) campaign highlighted that aerosol properties in the Seoul Metropolitan Area are largely influenced by transboundary transported aerosols under prevailing westerlies (Al-Saadi et al., 2015; Crawford et al., 2021; Peterson et al., 2019). Shim et al. (2022) reported cases of high $PM_{2.5}$ episodes where influences of Asian dust particles could be detected, implying concurrent transport of anthropogenic pollution aerosols with Asian dust. Accordingly, HSRL signals were classified into clean, dust, pollution, pollution, and dust mixture (hereafter, mixed), and unclassified by implementing a decision tree similar to that of Yeo et al. (2016).

The depolarization ratio (hereafter, dpr) is defined as the ratio between the backscattered lidar signal intensity of perpendicular polarized components to the parallel polarized component (Schotland et

al., 1971). It is an intensive property of light-scattering aerosols and can be used as an indicator for spherical and non-spherical particles (Freudenthaler et al., 2009; Shimizu et al., 2004). However, using dpr as the sole classifier for aerosol type is controversial, since the classification results are highly dependent on the threshold dpr values, especially for pollution and dust mixed features. To establish an objective classification of aerosols depending on their optical properties, collocated surface PM observations were used.

**Figure 3.1** shows the distributions of surface $PM_{2.5}$-to-$PM_{10}$ ratio (hereafter, $PM_{2.5}/PM_{10}$) and $PM_{10-2.5}$ concentrations during the period of the HSRL deployment at SNU. The $PM_{2.5}$ threshold for clean aerosols was taken from the Ministry of Environment of Korea and National Institute of Environmental Research, 2022 which defines "good" air quality when the hourly $PM_{2.5}$ concentration is below 15 μg $m^{-3}$. During the period of the HSRL deployment in Seoul, 17 dust days were reported in Seoul by the Korea Meteorological Administration (KMA). While KMA provides dates when dust was detected, PM measurements are provided hourly, therefore, discrimination between hourly PM observations that are pure dust and merely observations taken within a dust day is needed. The red markers in **Figure 3.1** represent the surface PM observations during the reported 17 dust days. From the different $PM_{2.5}/PM_{10}$ and $PM_{10-2.5}$ distribution for dust days and non-dust days in **Figure 3.1**, it can be

inferred that pure dust aerosols display $PM_{2.5}/PM_{10}$ values smaller than 0.4 and $PM_{10\text{-}2.5}$ concentration larger than 75 μg $m^{-3}$. These threshold values are plausible since a majority of dust aerosols display larger size distribution than pollution aerosols (Sugimoto et al., 2016). Similarly, the $PM_{2.5}/PM_{10}$ and $PM_{10\text{-}2.5}$ thresholds for fine-mode dominant pollution aerosols can be concluded as $PM_{2.5}/PM_{10} > 0.6$ and $PM_{10\text{-}2.5} < 75$ μg $m^{-3}$. Dust and pollution mixed aerosols were defined as aerosols displaying $PM_{2.5}/PM_{10} < 0.6$ and $PM_{10\text{-}2.5} < 75$ μg $m^{-3}$.

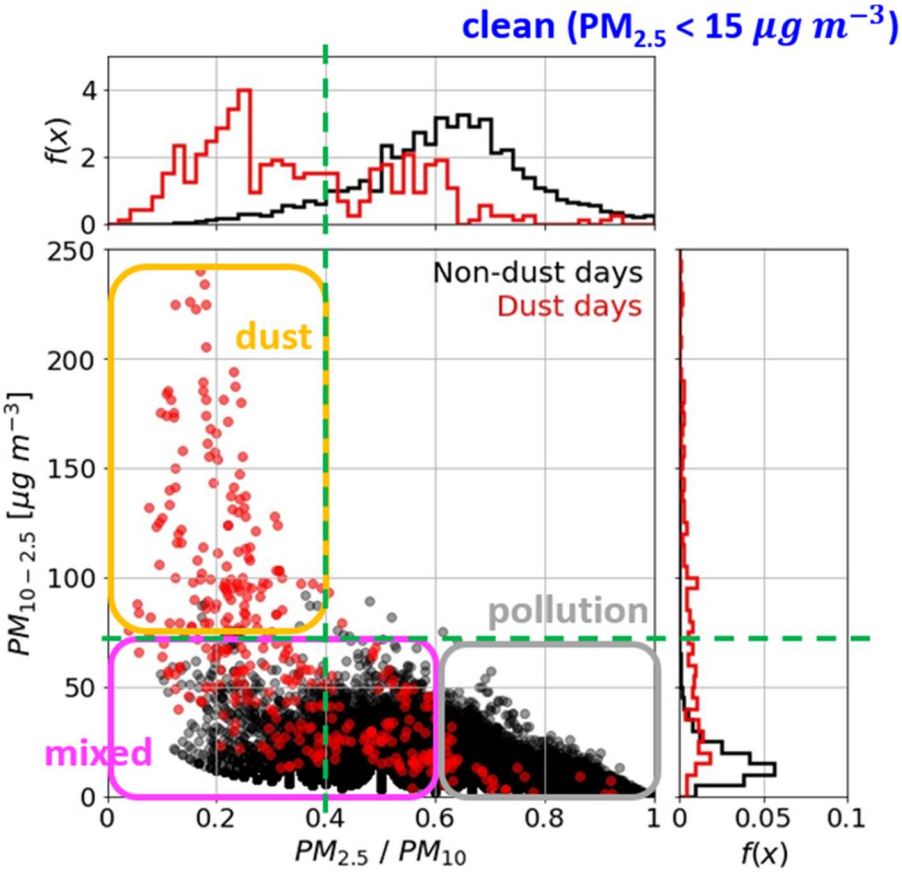


**Figure 3.1** Scatterplot and probability density functions of $PM_{2.5}$ to $PM_{10}$ ratio (x-axis) and $PM_{10\text{-}2.5}$ concentration (y-axis).

Based on the aerosol type classification using $PM_{2.5}/PM_{10}$ ratios and $PM_{10-2.5}$ concentration, the distribution of corresponding aerosol type-specific HSRL $\beta$ and dpr measurements are shown in **Figure 3.2**. Here, since surface-level measurements of PM concentration were used, HSRL $\beta$ and dpr values within the boundary layer were used. The definition of boundary layer signals was done using the mixing layer height (MLH) definition following the work in Section 3.2.2.

As shown in **Figure 3.2**, clean aerosols display small $\beta$ values with mean and standard deviation $\beta$ of $2.3\times10^{-6} \pm 5.6\times10^{-6}$ $m^{-1}$ $sr^{-1}$. This is considerably smaller than the values displayed by other aerosol types (pollution: $4.4\times10^{-6} \pm 5.8\times10^{-6}$ $m^{-1}$ $sr^{-1}$; mixed: $3.8\times10^{-6} \pm 4.5\times10^{-6}$ $m^{-1}$ $sr^{-1}$; dust: $4.4\times10^{-6} \pm 2.7\times10^{-6}$ $m^{-1}$ $sr^{-1}$). HSRL dpr for dust aerosols displayed larger values as reported in literature (Kim et al., 2010; Sugimoto and Lee, 2006) with mean and standard deviation values of 0.22 ± 0.06. On the other hand, pollution aerosols that are mainly consisted of non-spherical particles displayed the lowest mean dpr values (0.05 ± 0.03). Mixed aerosols displayed intermittent values of dpr (0.07± 0.04). Since $\beta$ is an extensive aerosol property that is dependent on the amount of aerosols, $\beta$ was only used in classifying clean aerosols. Therefore, it should be noted that weak lidar signals were classified as clean aerosols regardless of the intensive properties.

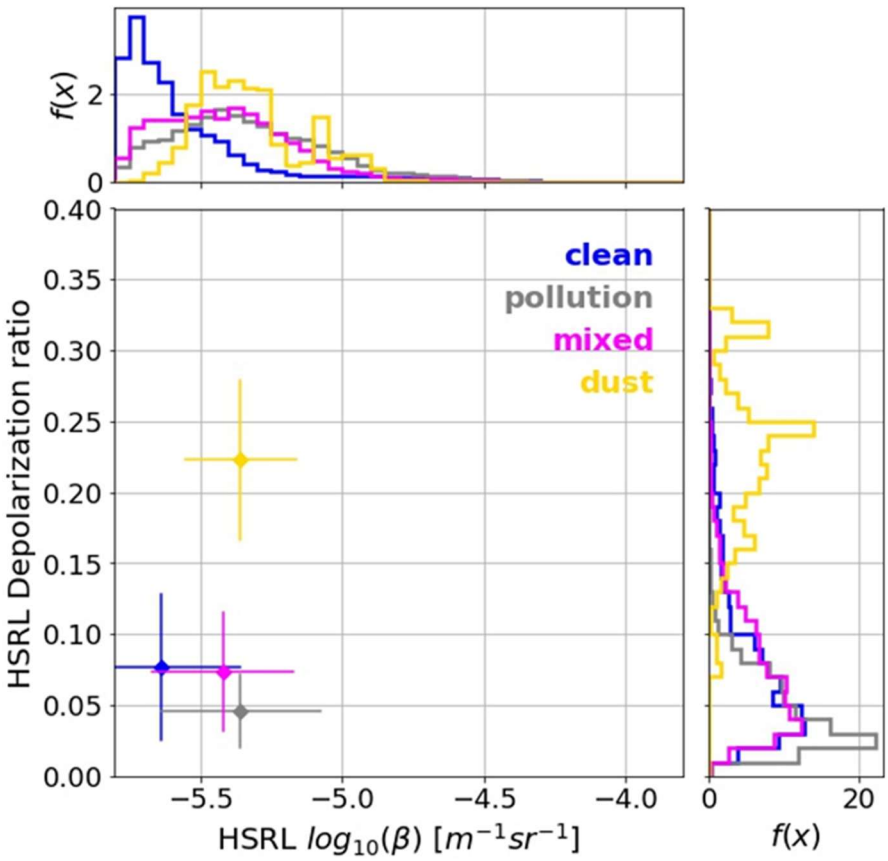


**Figure 3.2** Scatterplot and probability density functions of HSRL $\beta$ and dpr measurements by aerosol type, determined using collocated surface PM observations. The whiskers indicate one standard deviation of each variable.

**Figure 3.3** shows the flowchart of the HSRL aerosol type classification scheme. Input data contaminated by noise were primarily screened out based on the $\beta$ values at 532 nm. Depending on the intensity of the backscattered signal, $\sigma_{ext}$ is known to display uncertainties due to photon counting errors (Eloranta, 2018). The $\beta$ > $10^{-5.8}$ threshold was set empirically after careful analysis of the $\sigma_{ext}$ distribution in relation to $\beta$ when $\sigma_{ext}$ was found to display

discontinuous distributions. Therefore, signals classified as noise were excluded from the analysis. $\beta$ and dpr thresholds for clean, pollution, mixed, and dust aerosols were defined based on the type-specific distributions shown in **Figure 3.2**.

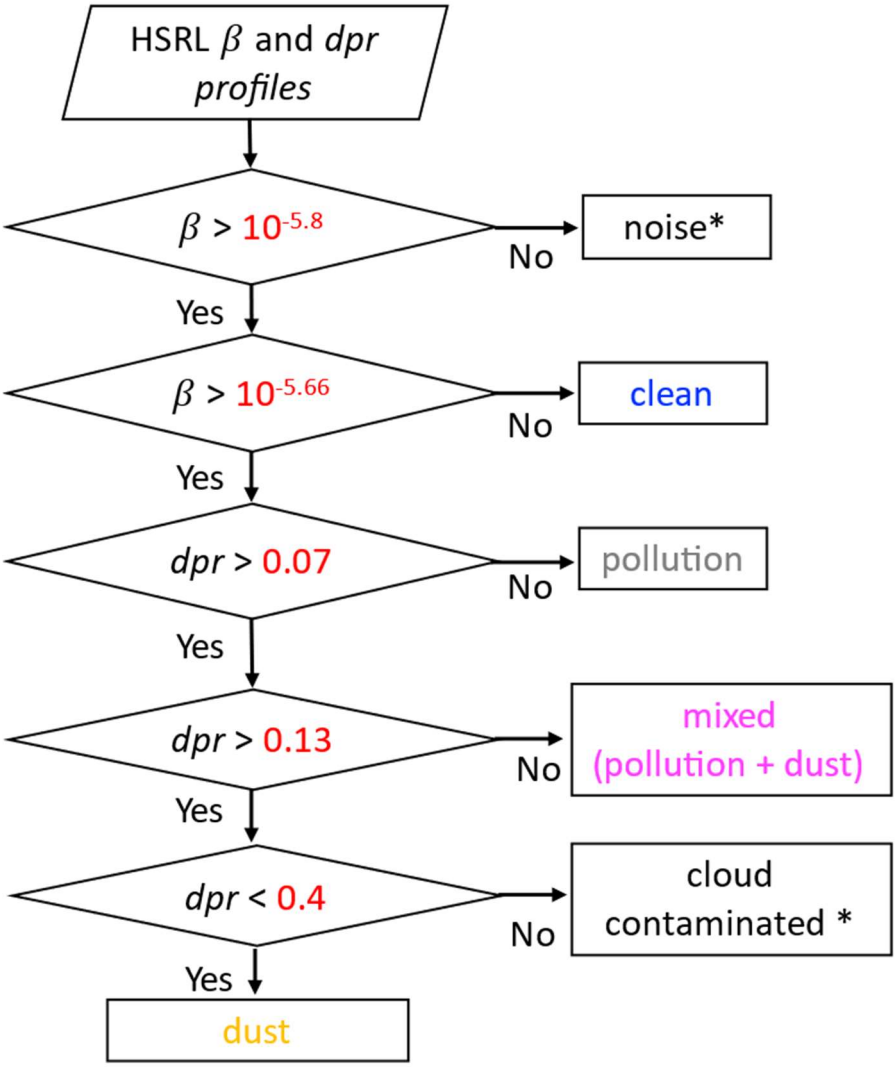


**Figure 3.3** Flowchart of the HSRL aerosol type classification scheme.

**Table 3.1** Type-specific lidar ratios defined from HSRL measurements classified into each aerosol type based on HSRL $\beta$ and dpr observations.

| | Mean $\pm$ standard deviation [sr] | Median [sr] | Mode [sr] |
|---|---|---|---|
| clean | $48 \pm 17$ | 46 | 36 |
| pollution | $57 \pm 15$ | 57 | 56 |
| mixed | $49 \pm 12$ | 49 | 49 |
| dust | $42 \pm 10$ | 42 | 38 |
| total | $52 \pm 16$ | 53 | 56 |

**Table 3.2** Type-specific lidar ratios defined from HSRL measurements classified into each aerosol type based on collocated surface PM observations.

| | Mean $\pm$ standard deviation [sr] | Median [sr] | Mode [sr] |
|---|---|---|---|
| clean | $45 \pm 19$ | 41 | 36 |
| pollution | $57 \pm 15$ | 57 | 58 |
| mixed | $52 \pm 14$ | 51 | 56 |
| dust | $42 \pm 10$ | 42 | 39 |
| total | $52 \pm 16$ | 53 | 56 |

The type-specific lidar ratios calculated by taking the ratio of HSRL $\sigma_{ext}$ and $\beta$ measurements are given in **Table 3.1**. For consistency between the aerosol classification scheme based on surface PM observations, lidar ratios for aerosols within the boundary layer are shown. Overall, the lidar ratios displayed large variations within each aerosol type, which can be attributed to the lidar ratio dependence on relative humidity, chemical composition, and size distribution (Düsing et

al., 2021; Floutsi et al., 2023; Müller et al., 2007) which can vary within the same aerosol type. **Table 3.2** presents the same HSRL lidar ratios as **Table 3.1** but classified into each aerosol type based on collocated surface PM observations. The differences between the two classification methods are prominent in mixed aerosols. This can be attributed to the sensitivity of type classification on the dpr threshold value.

**Figure 3.4** shows the distribution of lidar ratios for various aerosol types, presented in previous studies. The average lidar ratio reported in this study showed values between pollution and dust, indicating the influence of both aerosol types in Seoul. Kim et al. (2015) and Yeo et al. (2016) reported larger mean lidar ratio values in Seoul with means exceeding 60 sr. Both studies used Mie-scattering lidar measurements and collocated sky-radiometer column AOD as constraints, leading to restricted sampling during the day. Therefore, the use of sky-radiometer AOD measurements as constraints leads to limited lidar ratio retrieval during daytime, and when the AOD was significantly large enough to be used as a constraint. In addition, the lidar ratios in Kim et al. (2015) and Yeo et al. (2016) are the column mean lidar ratio values, compared to the lidar ratios of boundary layer aerosols specified in this study. In addition, the HSRL can retrieve lidar ratios under all-sky conditions including nighttime. Therefore, improvement of the accuracy of aerosol backscatter and extinction coefficients is expected through applying the

type-specific lidar ratios of clean, pollution, mixed, and dust of 48 sr, 57 sr, 49 sr, and 42 sr to type-classified lidar signals. Quantification of the improvement of aerosol $\sigma_{ext}$ using type-specific lidar ratios is possible using the co-located HSRL and Mie-scattering lidar measurements in Seoul.

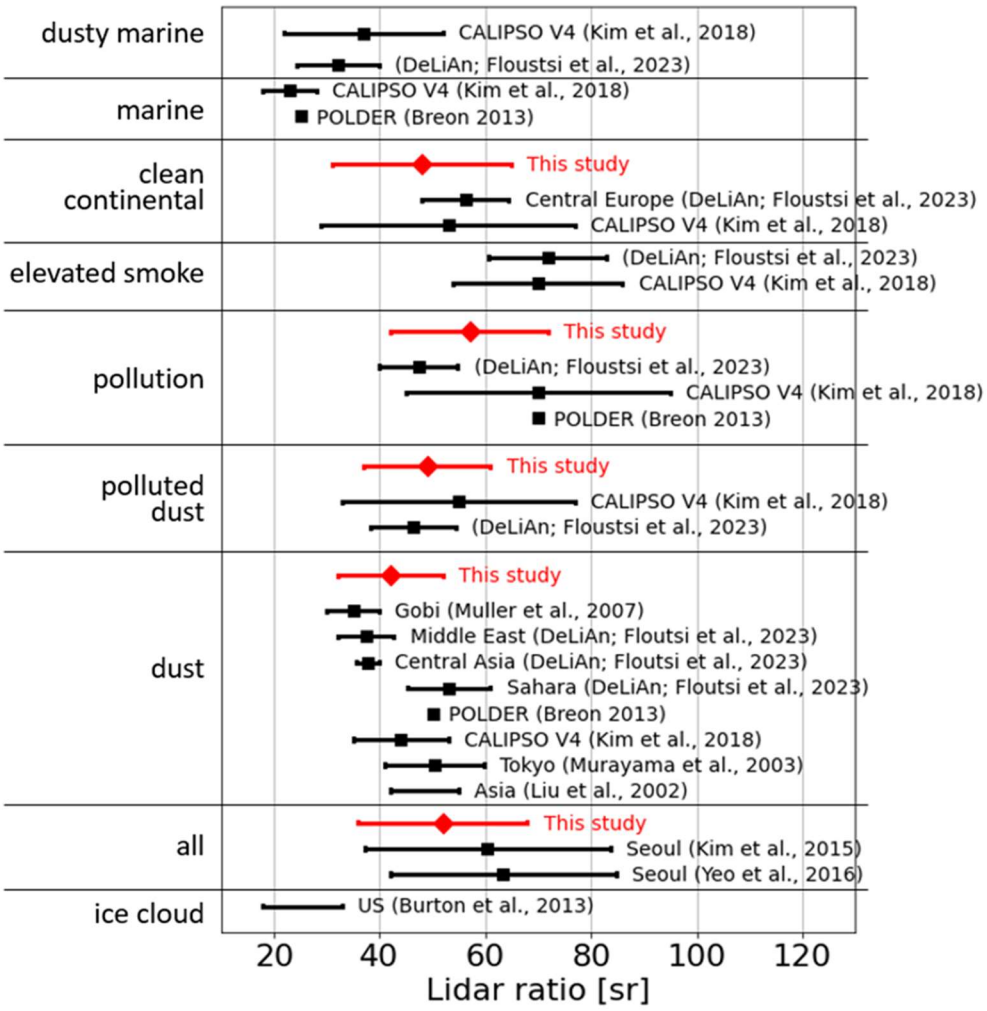


**Figure 3.4** Global aerosol lidar ratios for representative aerosol types published in previous studies. Lidar ratios from HSRL measurements in this study are plotted in red.

## 3.2 Improvement of Mie-scattering lidar extinction coefficient retrievals using type-specific lidar ratios

Prior to application of type-specific lidar ratios to Mie-scattering lidar measurements, an independent aerosol type-classification scheme was required. Based on the flowchart of **Figure 3.3**, thresholds of the range-corrected signal and dpr from the Mie-scattering lidar were separately defined due to the differences in lidar systems. The simplest method would be to take the relationship between the HSRL variables and the Mie-scattering lidar variables and calculate the corresponding range-corrected signal and dpr thresholds from HSRL to the Mie-scattering lidar domain. However, the correlation between the HSRL signals and Mie-scattering lidar signals displayed poor correlation (R = 0.23). Therefore, the Mie-scattering lidar range-corrected signal and dpr threshold values for each aerosol type were primarily defined based on surface PM observations. Secondly, the aerosol type-classification results were compared with the HSRL aerosol type-classification results, and the correlation scores were calculated by changing the range-corrected signal and dpr threshold values. The finalized Mie-scattering range-corrected signal and dpr threshold values for aerosol type classification were chosen based on the Rand Index (RI) score. The RI represents the similarity measure between two clusters by considering all possible pairs of samples and counting the pairs that are assigned to the same of

different clusters in the predicted and true clusters (Hubert and Arabie, 1985). It is defined as the ratio between number of agreeing pairs and the total number of pairs and ranges between 0 and 1, with RI scores of 1 indicating a perfect match. The resulting flowchart of aerosol type classification using Mie-scattering range-corrected signal and dpr profiles as input data is given in **Figure 3.5**.

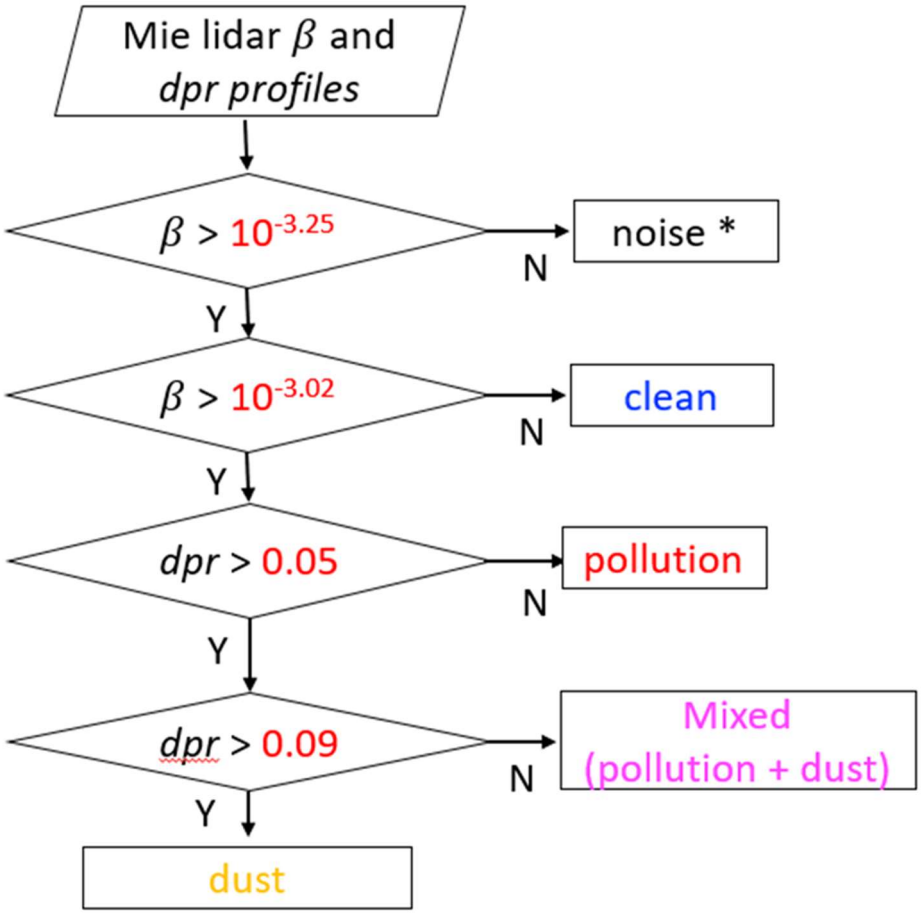


**Figure 3.5** Flowchart of the Mie-scattering lidar aerosol type classification scheme.

An example case of the aerosol type classification results of Mie-

scattering lidar measurements from 13 to 15 April 2016 is given in **Figure 3.6**. Clouds were detected around 1 km during 12 – 15 Local standard time (LST) of 13 April. Low-level clouds accompanied by precipitation were observed during 6-12 LST 14 April. Pollution aerosols were dominant within the boundary layer until 6 LST 15 April. Based on the aerosol type-classification results, mixed aerosols were dominant within the boundary layer after 9 LST 15 April. An elevated dust layer distributed within the free troposphere was detected on 13 April. The conversion from pollution aerosols to mixed aerosols during the morning of 15 April 2016 can be attributed to the intrusion of the elevated dust layer into the boundary layer. An elevated aerosol layer located between 2-3 km from 12 LST 15 April was classified as mixed aerosols.

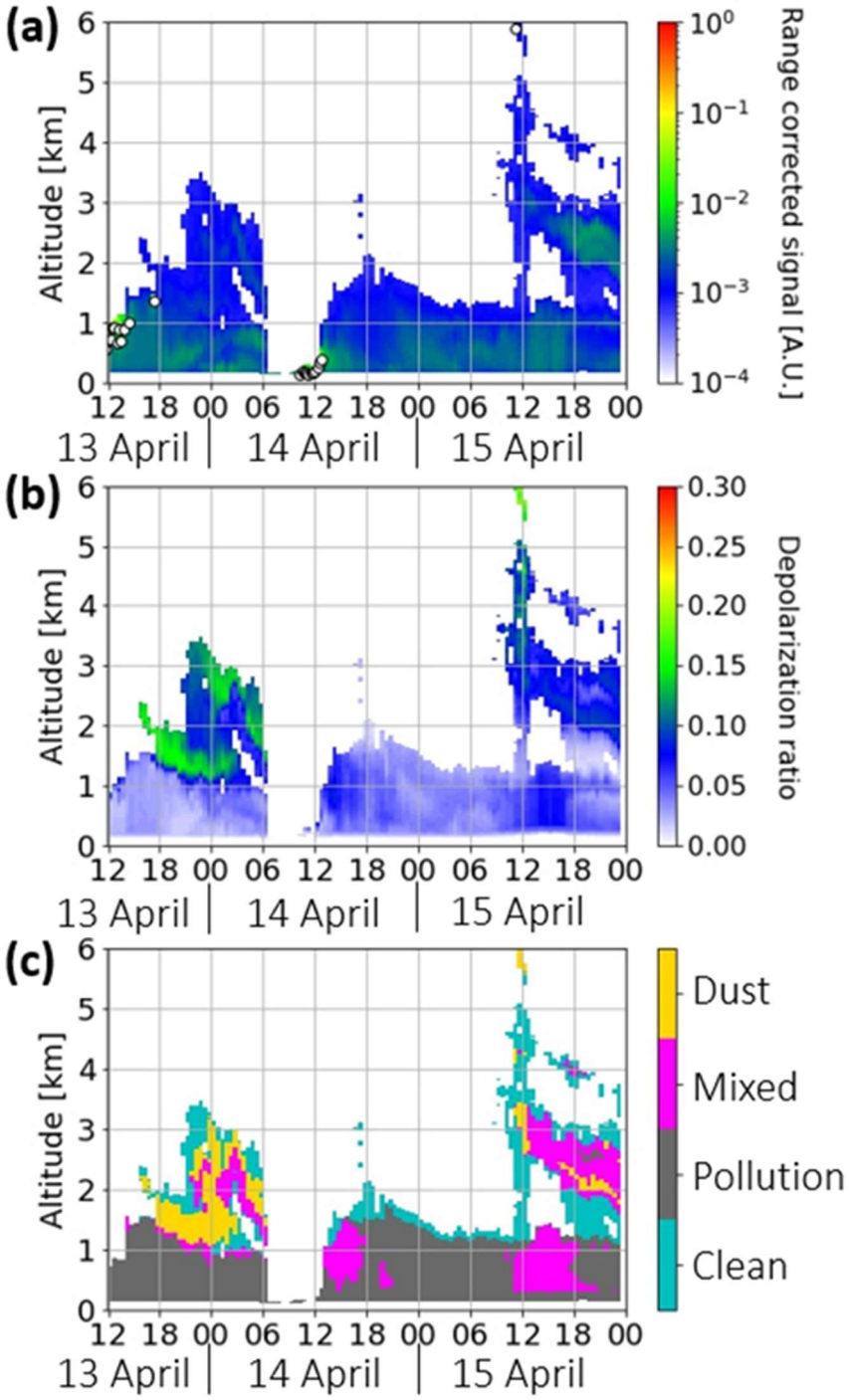


**Figure 3.6** (a) Time-height plots of Mie-scattering lidar range-corrected signal, (b) time-height plots of Mie-scattering lidar depolarization ratio, and (c) time-height plots of the aerosol type index for 13 to 15 April 2016.

**Figure 3.7** displays the frequency distributions of each aerosol type classified using Mie-scattering lidar measurements within the boundary layer during March 2016 to January 2018. The total number of data points used in the type-classification process decreased with height. This is due to the diurnal variation of the MLH that decreases to heights lower than 1 km during the night, increasing to its maximum height after sunrise until the afternoon (Park et al., 2022). Therefore, the frequency of each aerosol type was investigated (**Figure 3.7b**). Overall, pollution aerosols were most frequently observed within the boundary layer, followed by mixed aerosols. Dust aerosols were least frequently observed within the boundary layer.

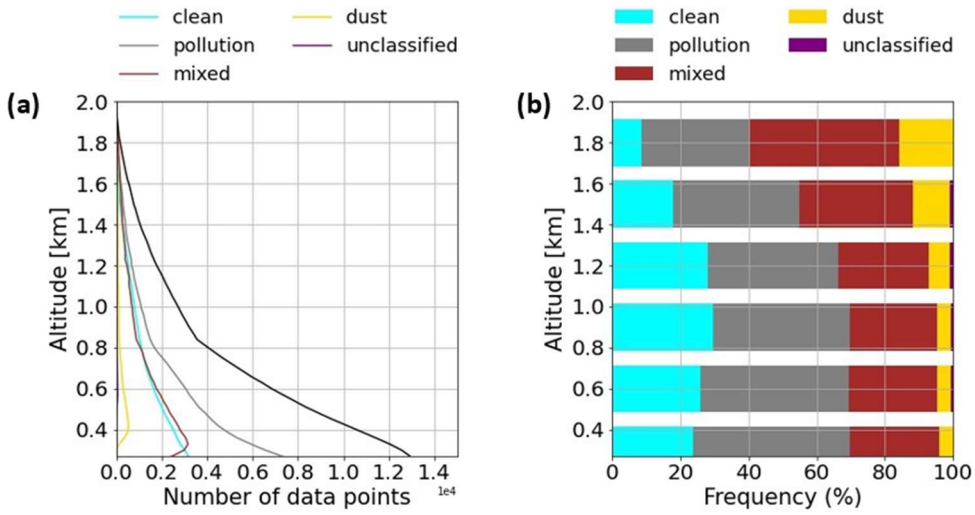


**Figure 3.7** (a) Profile of the number of data points by aerosol type during March 2016 – January 2018. (b) Frequency of each aerosol type by height within the boundary layer.

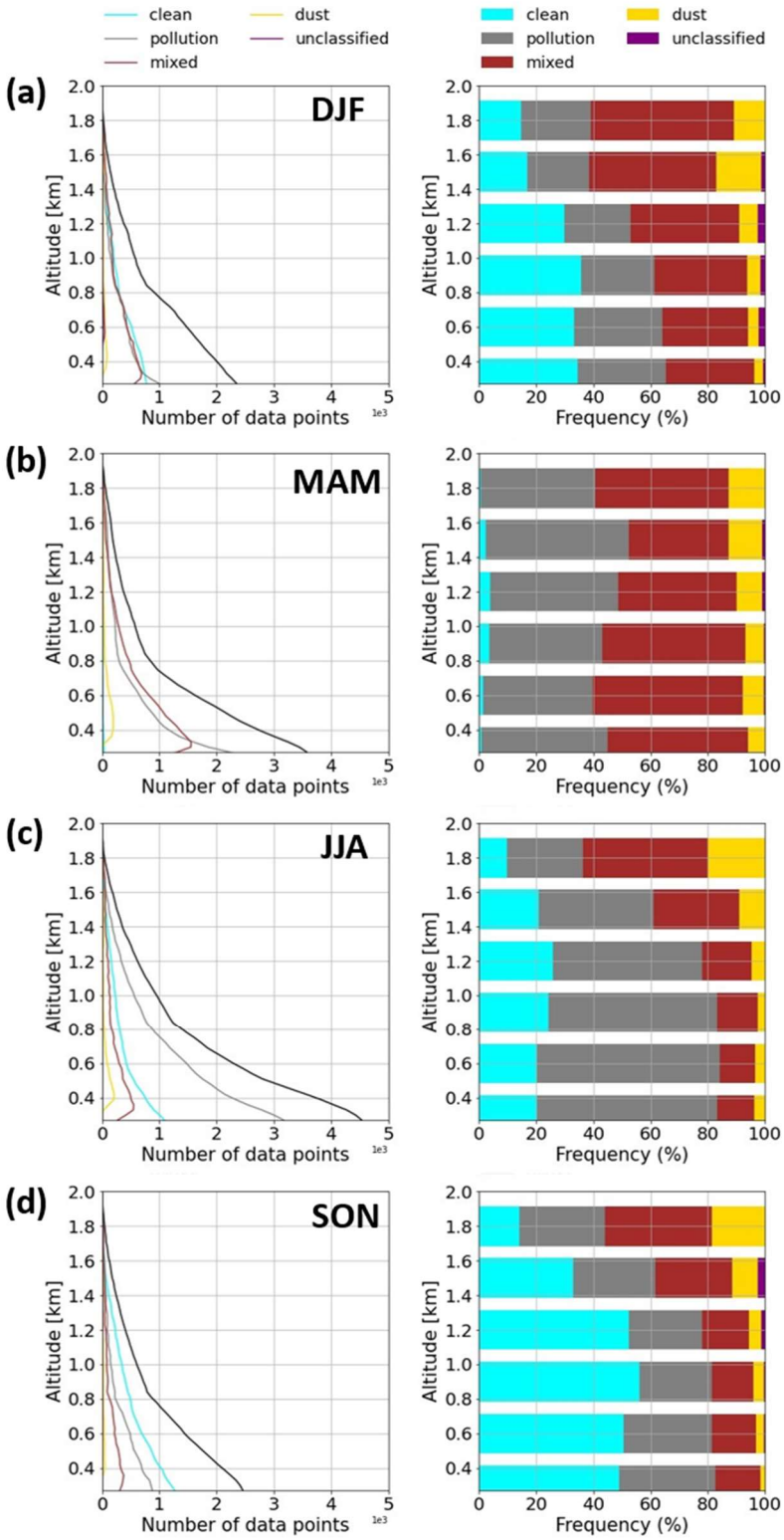


**Figure 3.8** Same as Figure 3.7 but by season.

The frequency of aerosol type displayed significant seasonality since aerosols that are transported to Seoul from upwind regions are influenced by the prevailing winds that vary greatly by seasonal synoptic patterns (**Figure 3.8**). Clean aerosols were most dominant during fall due to the frequent transport of air masses of clean continental origin because of the transition of the prevailing wind direction (Kim et al., 2007a; Park, Kim, et al., 2019). Pollution aerosols were most frequently observed during summer. While studies have reported relatively clean air quality during summer in Korea due to the washout of pollutants by frequent rainfall and the summer monsoon (Kim S. et al., 2014; Yoo et al., 2014; Yoon et al., 2010), we note that the pollution defined using lidar measurements are based on aerosol intensive optical properties, indicating the existence of pollution, not mass concentration.

The relative error in extinction coefficient is known to be considerably higher in the case of complex aerosol distribution (i.e., different aerosol in the vertical, well-mixed layers; Müller et al., 2007). Berjón et al. (2019) assessed the errors that would occur if retrieving extinction from a lidar backscatter signal when assuming a single aerosol type with a corresponding single lidar ratio value for a case with two different aerosol layers. In their study, the AOD of the different aerosol layers were constrained using coherent sky-radiometer measurements located at different altitudes which resulted in significant biases between

the retrieved $\sigma_{ext}$ profiles.

As aerosols from a variety of aerosol sources (e.g., pollution, dust, polluted-dust, biomass burning), are frequently observed in Seoul, extinction profiles retrieved from an elastic backscatter lidar are expected to show great variation depending on the aerosol structure when applying lidar ratios to the lidar equation. Collocated HSRL $\sigma_{ext}$ measurements provide the opportunity to further validate each method and quantify the errors that occur due to assuming a simple atmosphere compared to the actual state.

Therefore, the lidar ratios defined from type-classified HSRL measurements (**Figure 3.4**), were applied to Mie-scattering lidar to examine the differences in extinction profile calculations due to differences in lidar ratios. The $\sigma_{ext}$ profiles were retrieved by solving the lidar equation (equation (1)) following the steps in Klett (1985) and Sasano et al. (1985) where the lidar ratio is given as a function of range. To assess the differences in $\sigma_{ext}$ depending on lidar ratio information, $\sigma_{ext}$ was also calculated using a single lidar ratio value. Here, the overall mean lidar ratio within the boundary layer (52 sr) was applied when calculating the $\sigma_{ext}$ with a single lidar ratio value. Hereafter, the $\sigma_{ext}$ calculated using type-specific lidar ratio will be referred to as $\sigma_{ext}^{Mie-type}$, and the $\sigma_{ext}$ calculated using a single lidar ratio will be referred to as $\sigma_{ext}^{Mie-single}$.

An example case of the $\sigma_{ext}$ calculated from Mie-scattering lidar measurements from 13 to 15 April 2016 using aerosol type-specific lidar ratios is given in **Figure 3.9a**. Larger biases in the $\sigma_{ext}$ according to the retrieval method ( $\sigma_{ext}^{Mie-type}$ - $\sigma_{ext}^{Mie-single}$ ) were found at heights corresponding to the altitude of existing dust and pollution aerosols. Since the lidar ratio used in calculating the extinction coefficient using a single lidar ratio (52 sr) was larger than that of dust lidar ratio (42 sr) and smaller than that of pollution lidar ratio (57 sr), the bias between $\sigma_{ext}^{Mie-type}$ and $\sigma_{ext}^{Mie-single}$ displayed negative values at the heights where dust aerosols were found, and positive values at the heights where pollution aerosols existed (**Figures 3.9c** and **3.9d**).

$\sigma_{ext}$ retrieved from Mie-scattering lidar measurements were ultimately verified using HSRL $\sigma_{ext}$. **Figure 3.10a** shows the scatterplot of $\sigma_{ext}^{Mie-type}$ versus HSRL $\sigma_{ext}$. **Figure 3.10b** is the scatterplot between $\sigma_{ext}^{Mie-single}$ and HSRL $\sigma_{ext}$. Overall, better correlation between HSRL and Mie-scattering lidar $\sigma_{ext}$ was found when type-specific lidar ratios were used in the retrieval process. The decrease in $\sigma_{ext}$ mean bias from -0.026 $km^{-1}$ to -0.019 $km^{-1}$ can result in an error reduction of 0.042 in AOD. Considering that the mean AOD in Seoul is observed to be around 0.40 ± 0.37 (HSRL AOD) and 0.27 ± 0.32 (AERONET AOD), 10% to 16% reduction of total column AOD error can be achieved by using type-specific lidar ratio values by calculating $\sigma_{ext}$ from Mie-scattering lidar

observations.

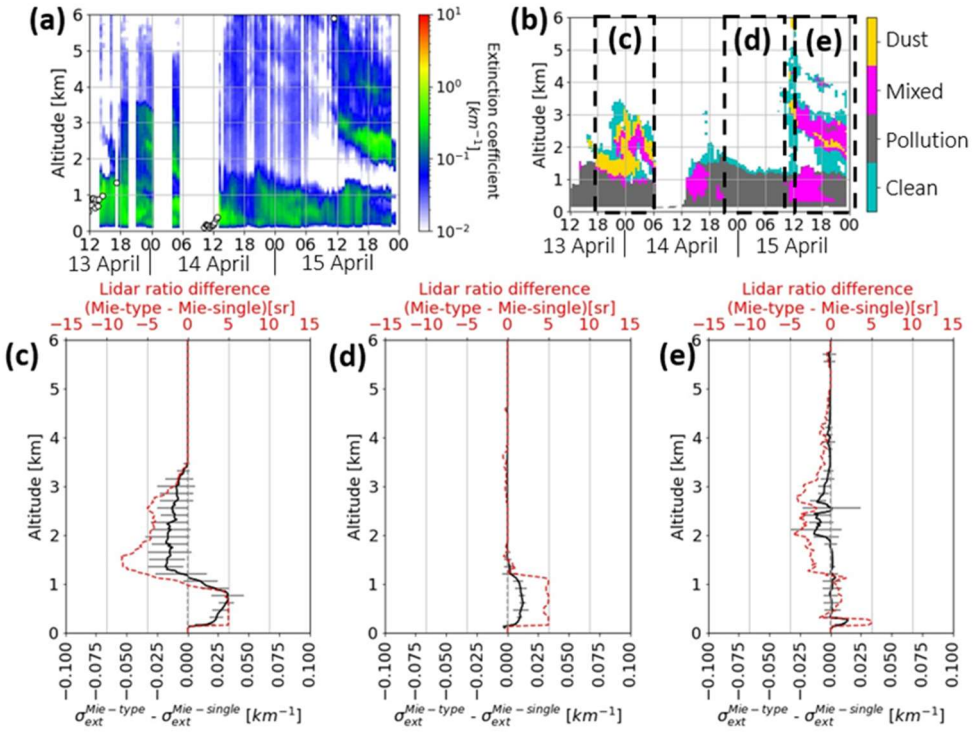


**Figure 3.9** (a) Time-height plot of Mie-scattering lidar extinction coefficient calculated using aerosol type-specific lidar ratios ($\sigma_{ext}^{Mie-type}$). (b) Time-height plot of aerosol types. (c) Profile of the bias between $\sigma_{ext}^{Mie-type}$ and single lidar ratio calculated $\sigma_{ext}$ ($\sigma_{ext}^{Mie-single}$) for 18 LST 13 April to 6 LST 14 April 2016. (d) same as (c) but for 21 LST 14 April to 9 LST 15 April 2016. (e) same as (c) but for 12 to 23 LST 15 April 2016. Differences in lidar ratio are overplotted in red in (c), (d), and (e).

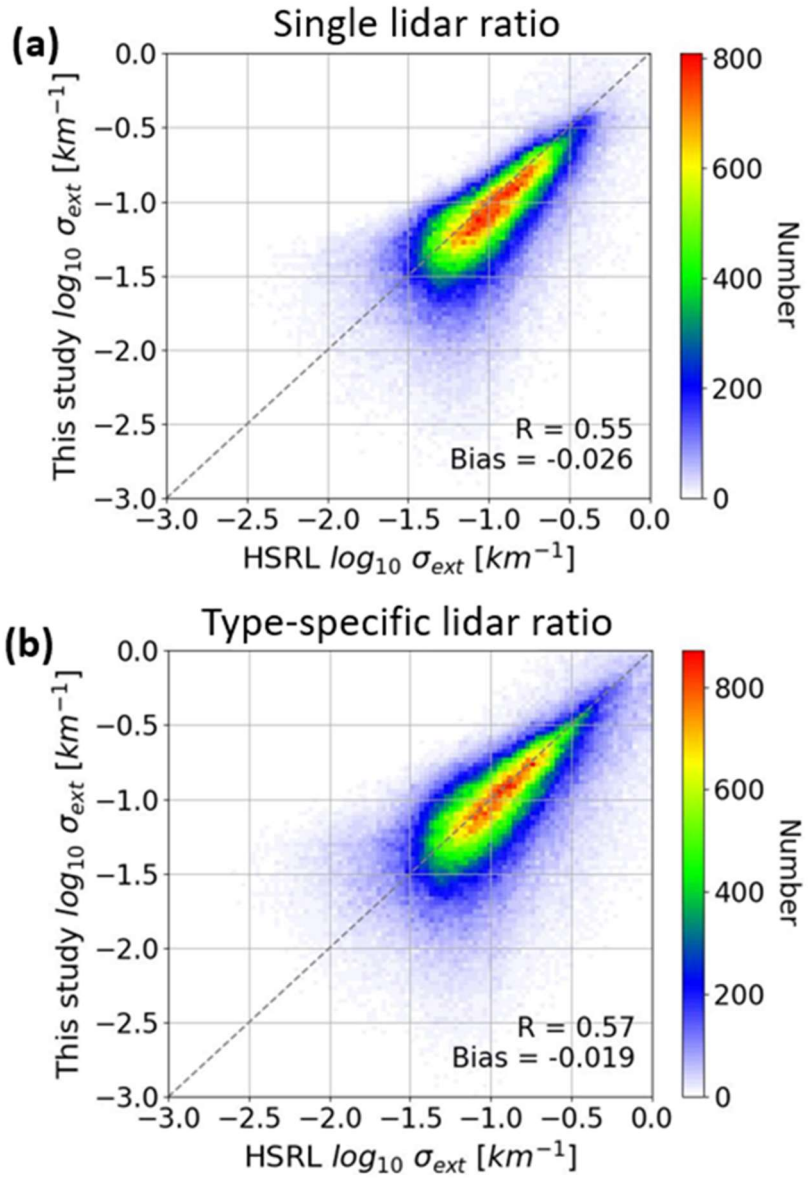


**Figure 3.10** (a) Scatterplot of HSRL $\sigma_{ext}$ (x-axis) and $\sigma_{ext}^{Mie-single}$ (y-axis). (b) Scatterplot of HSRL $\sigma_{ext}$ (x-axis) and $\sigma_{ext}^{Mie-type}$ (y-axis). Data period is from March 2016 to January 2018.

# Chapter 4 Diurnal variation of boundary layer and free troposphere aerosol optical depth

Aerosol optical depth (AOD), defined as the column-integrated amount of solar radiation extinction caused by aerosols, has been widely used in investigating the climate forcing of aerosols (Ma et al., 2014; Shindell et al., 2013). AOD is also used as proxy for estimating surface air quality and for assimilation and evaluation data used in aerosol modeling and forecast (Guo et al., 2017; Li et al., 2013). Previous studies have demonstrated notable improvements in aerosol forecasting through the assimilation of ground-based remote sensing (e.g., AERONET, SKYNET) and satellite aerosol products, mainly by observing daytime aerosol optical properties (Schutgens et al., 2016; Zhang et al., 2008; Xu et al., 2015). In estimating surface PM concentrations from atmospheric parameters, Park, Shin, et al. (2019) identified aerosol optical depth (AOD) as the most significant factor compared to other parameters such as wind speed, solar radiation, and dew-point temperature. Many studies have investigated the temporal and spatial variation of AOD using satellite and sky-radiometer measurements (Lee, S. et al., 2021; Kang et al., 2019; Zhai et al., 2021; Zhang et al., 2012). Using AERONET measurements, Lennartson et al. (2018) reported a diurnal variation of -30 to 20% in AOD at inland sites of South Korea, which was comparably larger than the ± 20% diurnal variation observed at coastal sites. From

the Geostationary Ocean Color Imager (GOCI) and Advanced Himawari Imager (AHI) satellite measurements, Zhai et al. (2021) reported summer maximum and winter minimum in AOD over Northern China and South Korea, but the temporal variation was found to be much weaker in South Korea, as a result of smaller variation in boundary layer depth and less residential coal emissions. In Lee, S. et al. (2021), AOD from GOCI satellite measurements was used to detect the long-range transport of aerosols from upwind regions and its relationship with elevated surface $PM_{2.5}$ in Seoul. As such, satellite and ground-based networks can provide large spatial coverage of aerosol observations.

Nighttime AOD is especially essential in understanding the full diurnal behaviour of aerosols, its pre-convection, pre-photochemistry effects, and the nocturnal mixing layer dynamics (Barreto et al., 2013; Berkoff et al., 2011; Uchiyama et al., 2019). Consequently, observationally-based nighttime aerosol studies have drawn increasing attention from the science community (Campbell et al., 2012; Choo et al., 2016; Johnson et al., 2013). Modified versions of sun photometers were introduced that use lunar measurements to estimate nighttime aerosol optical properties (Li et al., 2016). While AERONET is developing new automatic nighttime direct moon measurements and is providing provisional lunar AOD products, they are still undergoing refinements to the algorithm and do not recommend publishing their data (AERONET

technical document; https://aeronet.gsfc.nasa.gov/new_web/Documents/Lunar_Algorithm_Draft_2019.pdf: last accessed 11 July 2023). There have also been efforts in retrieving nighttime AOD from satellites. McHardy et al. (2015) present an improved method from that of Johnson et al. (2013) by retrieving nighttime AOD from radiance from artificial light sources with the VIIRS Day/Night Band. However, limitations of nighttime AOD measurements through passive instruments exist due to the difficulty in accounting for the changes in light source intensity (Barreto et al., 2013; McHardy et al., 2015). In validating the newly implemented nighttime AOD retrievals, previous studies have either validated their results using co-located lidar attenuated backscatter signals as a proxy to the amount of aerosols in the atmosphere or by straddling the endpoints of daytime AERONET AOD. Although both methods showed to be effective, direct measurements of nighttime AOD will prove to be most effective in establishing the fidelity of inferred nighttime AOD.

## 4.1 Diurnal variation of AOD

From the HSRL molecular signal (equation (2)), the optical depth between two ranges can be retrieved. That is, vertically-resolved AOD can be calculated using the molecular signal ($P_m$) through equation (6).

$$\tau(R_2) - \tau(R_1) = \int_{R_1}^{R_2} \sigma(r')\, dr' = \frac{1}{2}\ln\left[\frac{\beta_m(R_2)P_m(R_1){R_1}^2}{\beta_m(R_1)P_m(R_2){R_2}^2}\right] \qquad (6)$$

where $\tau$ is the optical thickness, $\sigma$, the extinction coefficient, $\beta_m$, the molecular backscatter coefficient, and $P_m$ the molecular return signal. The molecular backscatter coefficient is computed from an independently supplied temperature profile (Eloranta, 2014). Like other elastic lidars, the HSRL experiences incomplete overlap between the backscattered signal and the field of view of the telescope. Although the UW-Madison HSRL includes a wide field of view channel that improves the characterization of the overlap function, additional correction for signals beneath 400 m is required (Eloranta, 2014). In this study, we assumed full mixing of aerosols within the mixing layer (ML) and accounted for the extinction coefficients ($\sigma_{ext}$) beneath 450 m altitude by taking the mean values of HSRL extinction coefficients between 450 m and the ML height (MLH).

HSRL profiles contaminated by clouds were excluded from the analysis by implementing an automated cloud detecting process. Cloud base heights (CBH) were estimated by finding the heights of negative peaks in the wavelet covariance of $\beta$ profiles (i.e., a sharp upward increase of $\beta$). After screening out of cloud-contaminated profiles based on cloud base height information, 55% (271582 of 491760) of HSRL 2-minute profiles were screened out.

**Figure 4.1** shows a scatterplot of AOD from AERONET sun/sky radiometer ($AOD_{AERONET}$) and HSRL ($AOD_{HSRL}$) measured at the SNU site from March 2016 to February 2018. AERONET version 3 level 2.0 measurement data was used and temporal collocation between the two instruments was achieved by taking the mean of 2-minute HSRL measurements within a ±2-minute window from the AERONET observation. To match the wavelength to that of the HSRL, AERONET Direct Sun AOD measurements at 500 nm were converted to AOD at 532 nm using the corresponding 440–675 nm Ångström exponents. AERONET Version 3, Level 2 quality data were used, indicating that the data was cloud-screened and quality-assured (Smirnov et al., 2000), with AOD uncertainty of 0.01 to 0.02 (Giles et al., 2019). Although Level 2 cloud-screened AERONET data were used, additional cloud screening of this data was made based on the cloud-screened $AOD_{HSRL}$. $AOD_{AERONET}$ contaminated by cirrus clouds were effectively removed in this process. As a result, the maximum $AOD_{AERONET}$ at 532 nm from March 2016 to January 2018 was reduced from 3.24 to 1.50, and the mean and median $AOD_{AERONET}$ were reduced from 0.34 to 0.27 and 0.24 to 0.21, respectively. As shown in **Figure 4.1**, the $AOD_{HSRL}$ and $AOD_{AERONET}$ displayed a good correlation with a mean bias of 0.00, root mean square error (RMSE) of 0.07, and $R^2$ value of 0.87. These results show that the AOD calculated from HSRL $\sigma_{ext}$ measurements are an accurate representation.

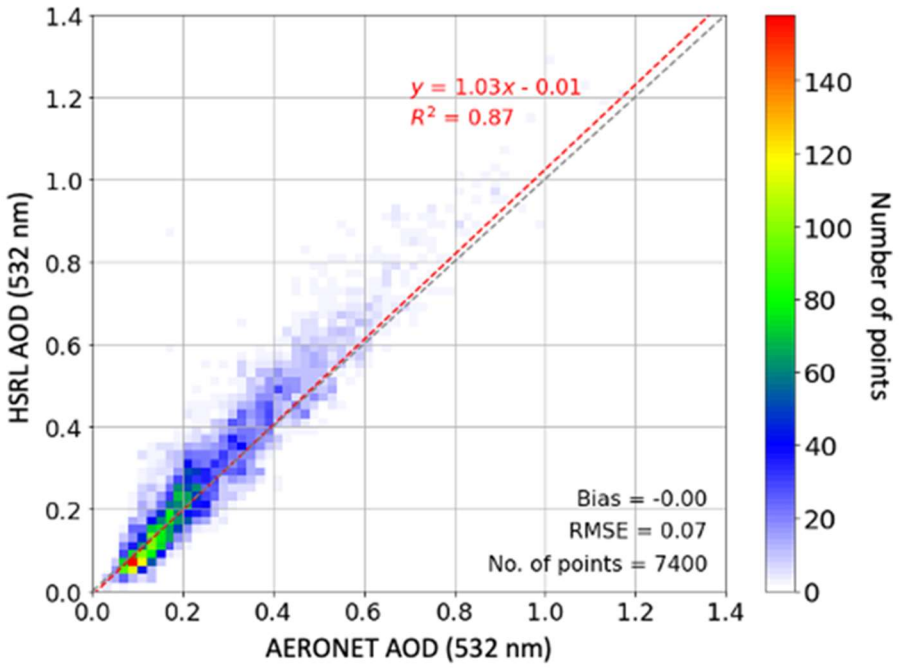


**Figure 4.1** Scatterplot of simultaneous AERONET (x-axis) and HSRL (y-axis) AOD at 532 nm.

The diurnal variation of $AOD_{HSRL}$ is shown in **Figure 4.2**. For comparison, the hourly means of $AOD_{AERONET}$ during the same period are also shown. It should be noted that due to the seasonality of sunlight hours throughout the year, the number of AERONET measurements was considerably low compared to HSRL measurements between 06-07 LST and 17-18 LST. Despite the difference in the number of measurements, $AOD_{AERONET}$ displayed a similar hourly pattern to $AOD_{HSRL}$. Similar patterns in the hourly AOD from long-term AERONET sun/sky radiometer observations at rural sites in Korea were reported by Lennartson et al. (2018) where the peaks in the morning and late evening

were attributed to traffic and transportation. However, the $AOD_{HSRL}$ displayed its peak at 04 LST instead of the apparent maxima at sunrise and sunset hours reported from daytime measurements (i.e., $AOD_{AERONET}$). As a result, nighttime AOD (0.45 ± 0.47) displayed larger mean values than during the day (0.40 ± 0.29). The large mean and standard deviation of nighttime AOD can be attributed to the nighttime formation of nitrate from the nocturnal processing of nitrogen oxides (Kim H. et al., 2018), a build-up of pollutants due to stagnant atmospheric conditions within the nocturnal boundary layer (Ma et al., 2017), and enhancement of aerosol extinction due to hygroscopic growth of aerosols (Eck et al., 2014; Titos et al., 2021; Ziemba et al., 2013).

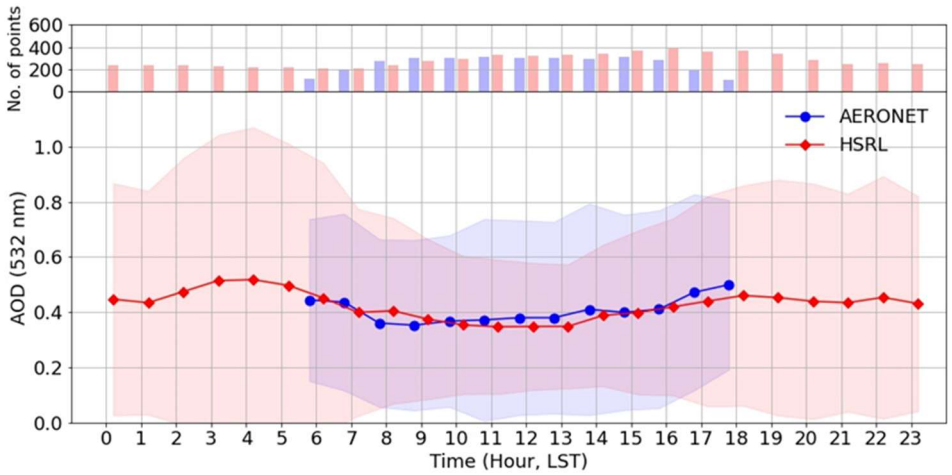


**Figure 4.2** Diurnal variation of HSRL (red diamond) and AERONET (blue circle) AOD at 532 nm. Solid markers indicate the mean AOD and one standard deviation from the mean is shaded in the background. Light bar graphs on the top depict the number of data points.

For further discussion of nighttime AOD enhancement, the relationship between AOD with surface-level RH was investigated. **Figure 4.3a** shows the binned AOD measurements as a function of each RH decile. The AOD displayed a positive correlation with surface-level RH, where the mean AOD of each RH decile resembled a power law function with respect to RH. Enhancement of the AOD due to the hygroscopic growth of aerosols was more prominent during the nighttime, corresponding to higher RH and a steeper curve between RH and AOD compared to the daytime AOD (**Figures 4.3b** and **4.3c**).

The diurnal variation of $AOD_{HSRL}$ and $AOD_{AERONET}$ by season is shown in **Figure 4.4**. AOD in summer was the largest with a mean value of 0.80 compared to winter with the lowest mean AOD value of 0.53. Nighttime AOD was larger than daytime AOD in all seasons, although the magnitude of its variation varied. As shown in **Figures 4.2** and **4.4**, it is possible to define the 24-hour variation of AOD with the HSRL that previous studies using passive sensors could not.

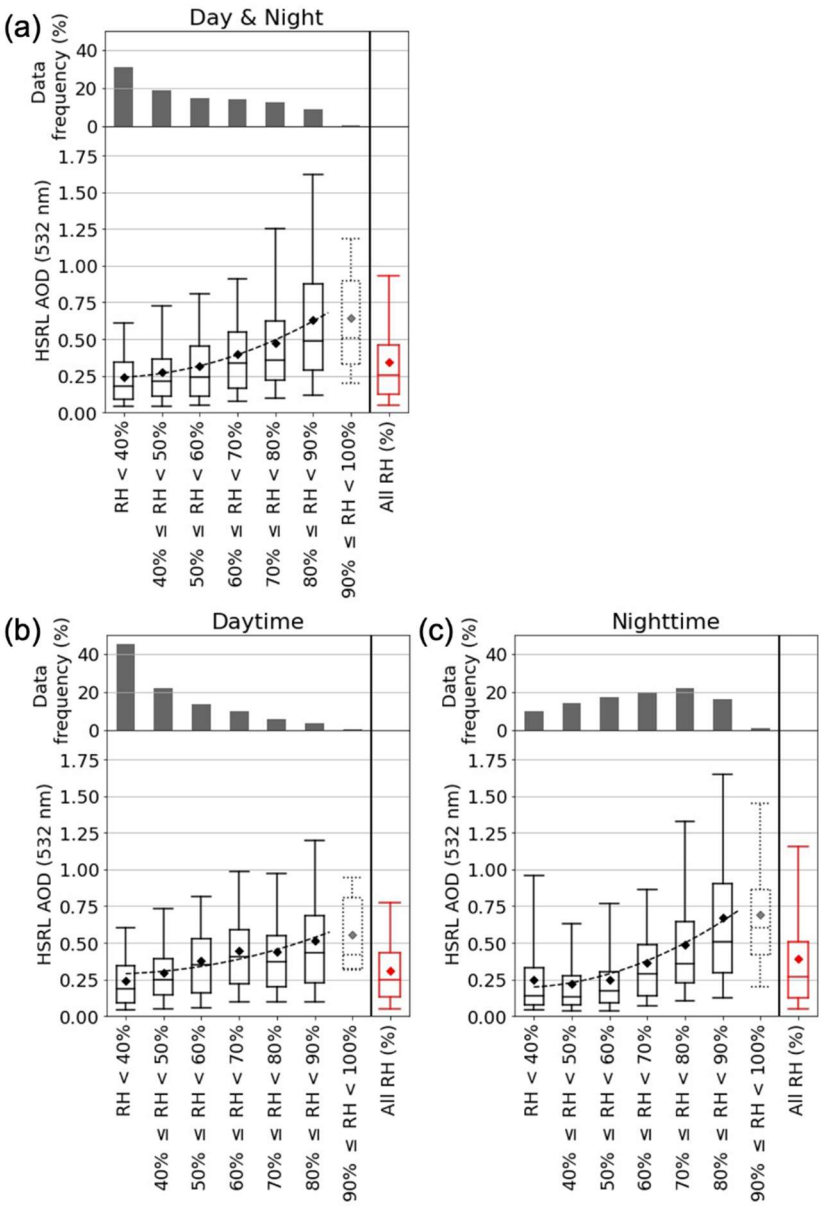


**Figure 4.3** The distribution of data frequency and hourly $AOD_{HSRL}$ binned by each RH decile: (a) the relationship of AOD with surface-level RH, (b) the relationship of daytime AOD with surface-level RH, and (c) the relationship of nighttime AOD with surface-level RH. Whiskers indicate the 5 and 95 percentile values; boxes indicate 25, 50, and 75 percentile values, and the markers indicate mean values. AODs for RH $\geq$ 90% conditions (dashed lines) were excluded from the regression between AOD and RH due to the scarcity of data.

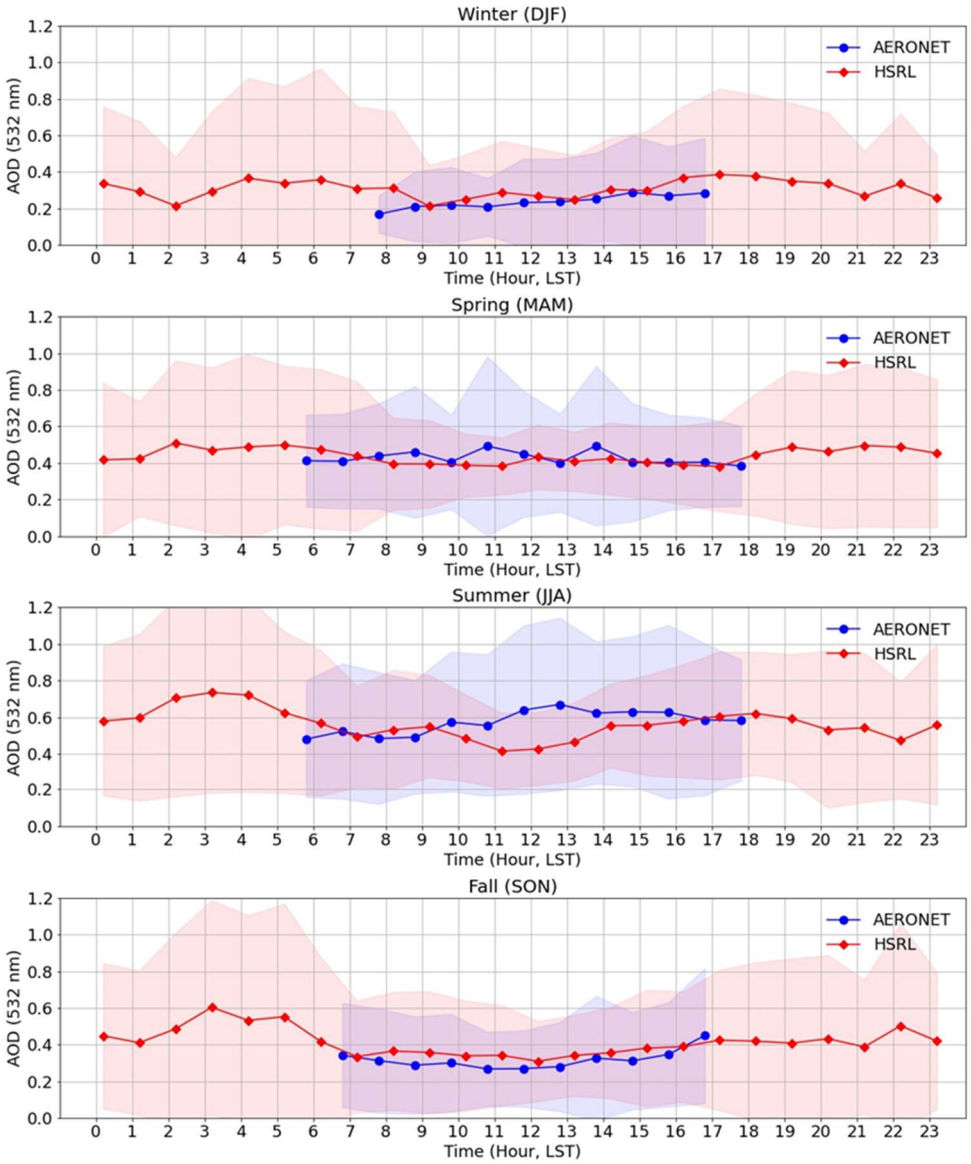


**Figure 4.4** Diurnal variation of HSRL (red diamond) and AERONET (blue circle) AOD at 532 nm by season. Solid markers indicate the mean AOD while one standard deviation from the mean is shaded in the background.

As shown in the box-whisker plots in **Figures 4.3b** and **4.3c**, nighttime AOD displayed a larger spread than daytime AOD; therefore, sampling issues may occur when discussing the mean AOD of scales

exceeding a daily degree. A simple analysis to examine the contribution of the sampling issue to AOD measurements was carried out by comparing the daily mean AOD calculated from AERONET and HSRL measurements. Daily mean $AOD_{AERONET}$ was compared with the daily means of temporally-collocated (**Figure 4.5a**) daytime (**Figure 4.5b**) and 24-hr (**Figure 4.5c**) $AOD_{HSRL}$ to assess the behavior of AOD daily means according to the temporal coverage of the sample. Daily mean $AOD_{AERONET}$ was retrieved only when there were at least three data points, following the recommendation of AERONET. The correlation was worst between the daily mean $AOD_{AERONET}$ and 24-hr daily mean $AOD_{HSRL}$ (mean bias = -0.02, RMSE = 0.1, $R^2$ = 0.78), indicating that nighttime AOD values significantly deviate from the daytime values at the urban site in Seoul.

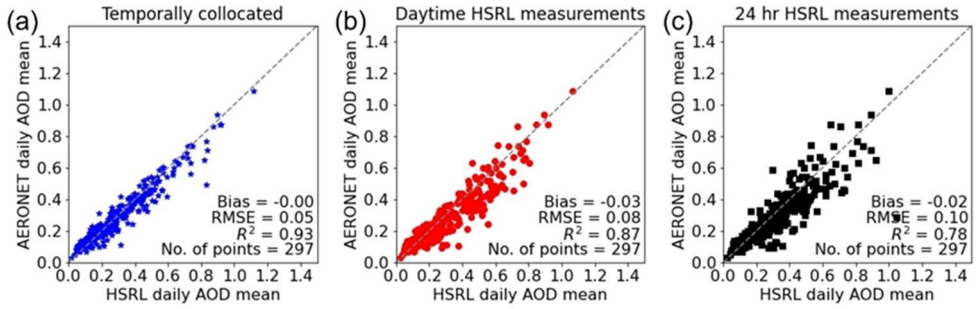


**Figure 4.5** Scatterplot of AERONET daily AOD mean (y-axis) with HSRL daily mean AOD calculated using (a) temporally-collocated AOD measurements, (b) daytime AOD measurements, and (c) 24-hr AOD measurements.

## 4.2 Boundary layer (BL) versus free troposphere (FT) AOD

The climatic effects of aerosols are strongly dependent not only on AOD, but also on the vertical distribution of aerosols and their optical properties. The vertical inhomogeneity of light-scattering or absorbing aerosols is also a driver of changes in the atmospheric stability (Barbaro et al., 2013; Gonçalves et al., 2015). Wu et al. (2016) reported that the aerosol layer height can change the top of the atmosphere reflectance and consequently affect the AOD retrieval from passive satellites. Therefore, realistic aerosol vertical profiles are essential for accurate characterization of the radiative effects of aerosols.

While AOD can be used as a proxy for the columnar aerosol amounts, difficulties exist in using the AOD as an indicator of the near-surface air quality due to the complexity of the vertical distribution of aerosols (Pal et al., 2014; Toth et al., 2014; 2019). Dong et al. (2017) reported different trends in AOD according to height resulting from the feedback between aerosols and planetary boundary layer dynamics based on satellite observations. Reid et al. (2017) reported large decoupling of AOD and surface $PM_{2.5}$ that was indicative of significant variability in aerosol vertical distribution induced by detrainment or mixing of aerosols depending on the atmospheric conditions. Therefore, investigation of the contribution of aerosols at different heights in the atmosphere to the

total column AOD through vertically-resolved measurements is necessary prior to using AOD as a reference for surface air quality.

The aerosol vertical distribution is known to be highly dependent on the height of turbulent mixing of aerosols and its precursors emitted from sources near the surface. The mixing layer height (MLH) is often defined as the height up to which turbulent mixing creates an environment conducive to the redistribution of temperature, aerosol mass, and humidity (Seibert et al., 2000; Stull 1988; Su et al., 2017). Depending on surface conditions, aerosols may be entrained to higher levels, but are mostly trapped within the MLH which contributes to the variance between columnar AOD and near-surface air quality indicators such as PM concentration. In Section 4.2, the contribution of aerosols within the boundary layer (BL) and free troposphere (FT) to columnar AOD is quantified using the 2-year HSRL measurements. The diurnal/seasonal variation of AOD of BL aerosols and FT aerosols is investigated and the implications for BL aerosol AOD on surface PM concentration estimation are discussed. Prior to quantifying the BL and FT aerosol AOD, an accurate estimation of the MLH is required. MLH retrieval methods from remote sensing measurements including lidar are described in Section 4.2.1 the advantages and limitations of each method are discussed.

### 4.2.1 Determination of mixing layer height (MLH)

MLH has been widely investigated to understand its implications on the vertical distribution of pollutants (Du et al., 2013; Zhao et al., 2019), especially in regions suffering from high pollution levels. For example, through ground-based remote sensing measurements, Kim et al. (2007b) noted that the growth and break-down of the MLH affect the surface ozone concentration up to the following day. Accurate simulation of MLH is especially crucial for atmospheric models simulating near-surface concentrations of air pollutants (Seo et al., 2015; Su et al., 2018), since models with inaccurate MLH attempt to compensate the inaccuracy of pollutant concentrations by adjusting other parameters, such as emission rates and atmospheric chemistry (Compton et al., 2013). Tangborn et al. (2021) presented examples of how assimilating MLH observations in WRF model improved the forecast results of model state variables such as wind and mixing ratio. Oak et al. (2019) demonstrated that the use of scaled MLH from elastic aerosol lidar observations in a chemistry transport model significantly improved simulations of surface ozone concentration. As such, an accurate understanding of the temporal behaviour of MLH based on continuous measurements is crucial for numerical modeling studies employing MLH (Lee H. et al., 2019; Lothon et al., 2014).

In this section, through intercomparison of MLH retrievals from co-

located elastic aerosol lidar, ceilometer, and wind Doppler lidar (WDL) measurements obtained in Seoul, the advantages and limitations of each method is discussed. Additionally, the relationship of MLH and vertical distribution of aerosols discussed from remote-sensing measurements is compared with that of chemistry transport model simulations to assess the extent to which mixing defined by various atmospheric variables correlate with actual aerosol vertical distributions in real atmosphere.

Assuming that aerosol concentration is uniformly distributed within the mixing layer and dramatically decreases in the free troposphere (Kim et al., 2007b), MLH from aerosol lidar (hereafter, $MLH_{lidar}$) and ceilometer (hereafter, $MLH_{ceilometer}$) can be determined as the height of strong decrease in $\beta$ measurements. Herein, we adopted the wavelet method, in which the convolution of the Haar function with the $\beta$ profile was used to define sharp increases or decreases in the signal (Brooks, 2003; Caicedo et al., 2017; Davis et al., 2000). Sharp decreases in the $\beta$ were identified by local maximum peaks of the wavelet covariance profile. The $MLH_{lidar}$ and $MLH_{ceilometer}$ were defined as the lowest local maximum peak in the wavelet covariance profile that exceeded a magnitude threshold. Peaks were detected by investigating the changes in the sign of the gradient of the wavelet covariance. A threshold value in the magnitude of the wavelet covariance peak was used to assure that MLH was defined at heights where there were significant decreases in the $\beta$ profile.

Threshold values were set for each individual profile as a ratio value of the maximum wavelet covariance peak value within 3 km from the surface. A ratio value of 0.9 was chosen in this study after analysis of MLH results from ratio values ranging from 0.8 to 1.0 with an increment of 0.05. Too low a ratio value resulted in unreasonable fluctuations in MLH with time, and too large a ratio value resulted in the misclassification of the top height of elevated aerosol layers as the MLH. An example of the $\beta$ profile from an aerosol lidar from 15 LST 5 October 2016 and its wavelet covariance, together with $MLH_{lidar}$ of 1.46 km above ground level (agl, horizontal dashed line), are shown in **Figures 4.6a** and **4.6b**.

A more direct approach to investigate mixing near the surface is possible using WDLs since they directly measure the vertical wind velocity instead of proxies of vertical mixing (Park et al., 2018; Tucker et al., 2009). In this framework, MLH from WDL (hereafter, $MLH_{WDL}$) can be estimated using a threshold value for vertical velocity standard deviation ($\sigma_w$; Barlow et al., 2011; Pearson et al., 2010; Tucker et al., 2009). For the purposes of this study, $\sigma_w$ was calculated following the work of Schween et al. (2014), i.e., every 5 minutes using the data of the surrounding ±15 min interval to sufficiently account for turbulence within the mixing layer. MLH was then defined using a threshold value of 0.2 m $s^{-1}$ (Träumner et al., 2011; Tucker et al., 2009) as the first height where $\sigma_w$ drops below the threshold value. WDL $\sigma_w$ profiles where no

data points exceeded the threshold value were regarded to have low turbulence or to be turbulent only within the height of the lowest range gate. For these cases, the lowest range gate of the WDL (60 m and 100 m for the Mitsubishi LR-S1D2GA and Leosphere's Windcube-200, respectively) was considered as the $MLH_{WDL}$. On the other hand, cases where WDL SNR was too low to provide adequate measurements up to heights where $\sigma_w$ dropped below the threshold value, were excluded from $MLH_{WDL}$ estimation. MLH was estimated as 1.3 km from the profile of $\sigma_w$ from the co-located WDL at 15 LST 5 October 2016 (**Figure 4.6c**).

Evaluation of the MLH retrieved from the afore-mentioned remote sensing instruments was done through comparison of MLH determined from radiosonde θ profiles. Radiosonde soundings from 3 to 7 October 2016, taken from the same site as the co-located lidar and WDL were used. The MLH from radiosonde soundings (hereafter, $MLH_{sonde}$) was defined as the top height of the layer in which a sharp decrease in θ is detected. The decrease in θ was identified by applying the wavelet method as was used in estimating the MLH from $\beta$ profiles. Demonstrated in **Figure 4.6d** is $MLH_{sonde}$ retrieved from the θ profile of 15 LST 5 October 2016 at 1.53 km which showed good agreement with those retrieved by the wavelet method from aerosol backscattered signal profile. On the other hand, discrepancies between the $MLH_{sonde}$ and $MLH_{WDL}$ can be attributed to differences in the methodology used to

define MLH. While $\sigma_w$ measured by WDL is thought to be a direct measurement of the mixing process, measurements from radiosonde and lidar are indicators of the result of the mixing process.

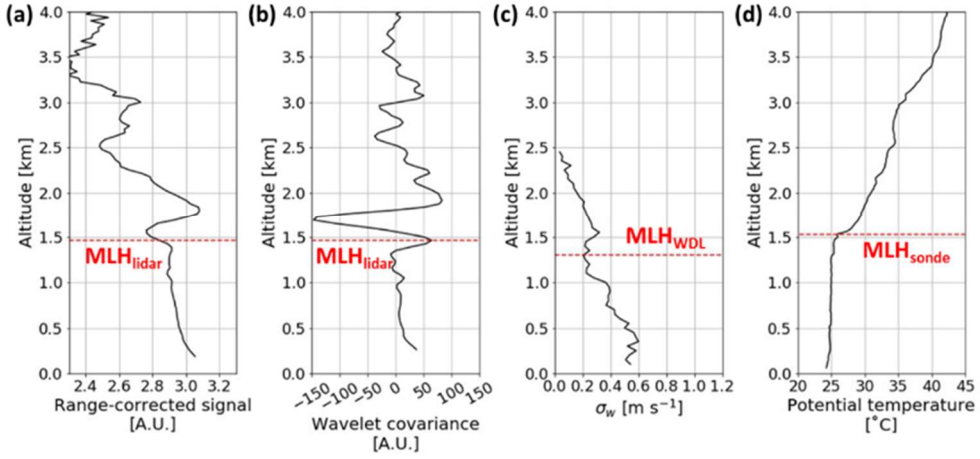


**Figure 4.6** Profiles of (a) aerosol lidar range-corrected backscattered signal (arbitrary units), (b) covariance transform applied to the lidar signal, (c) WDL vertical wind speed standard deviation ($\sigma_w$), and (d) radiosonde potential temperature at 15 LST on 5 October 2016. The horizontal dashed lines represent the MLH determined from each measurement profile.

**Figure 4.7** shows an example of measurements and derived MLHs from co-located three aerosol lidar, ceilometer, and WDL at the Jungnang observation site in Seoul on 6 October 2016. A common pattern of MLH growth after sunrise and decay after sunset was detected, similar to those reported in former MLH studies (Dang et al., 2019; Garratt, 1992; Haman et al., 2012). $MLH_{lidar}$ and $MLH_{ceilometer}$ displayed similar values (mean

bias = -0.03 km, $R^2$ = 0.84); reaching their peak height of 1.43 km and 1.53 km, respectively, at 16 LST. Radiosonde θ profiles closely resembled $\beta$ measured by aerosol lidar and ceilometer, thus resulting in good agreement among $MLH_{sonde}$, $MLH_{lidar}$, and $MLH_{ceilometer}$ (mean bias = -0.08 km; **Figure 4.7a**). On the other hand, $MLH_{WDL}$ from $\sigma_w$ displayed a different diurnal pattern with significantly lower nighttime MLH (**Figure 4.7c**). $MLH_{lidar}$ and $MLH_{ceilometer}$ during the nighttime hours showed heights of approximately 0.82 ± 0.29 km, whereas the $MLH_{WDL}$ averaged about 0.28 ± 0.20 km. The lower values of $MLH_{WDL}$ compared to $MLH_{lidar}$ and $MLH_{ceilometer}$ values reported in this study are consistent with Quan et al. (2013), which reported a difference of approximately 0.25 - 0.45 km between wind Radar and micro-pulse lidar MLH during nighttime. Despite low $\sigma_w$ during nighttime, aerosols were distributed up to heights exceeding 0.5 km. On investigating horizontal wind speed measurements, low-level jets, identified as localized maximum in the vertical profile of the horizontal wind, were observed at heights well corresponding to nighttime $MLH_{lidar}$ and $MLH_{ceilometer}$ (**Figure 4.8**). We could deduce that wind shear below the low-level jet created an environment where aerosols were suspended up to higher heights than where turbulence was measured by $\sigma_w$. Manninen et al. (2018) reported similar boundary layer structures, in which strong gradients in the attenuated backscattered lidar measurements at heights above 0.5 km

correlated with shear-driven turbulence were observed during nighttime, while convective mixing induced by surface heating only started to have its effect several hours after sunrise. Therefore, it could be deduced that while $\sigma_w$ profiles sufficiently captured convective mixing generated by daytime surface heating, it was not directly correlated with the vertical distribution of aerosols and its diurnal variation.

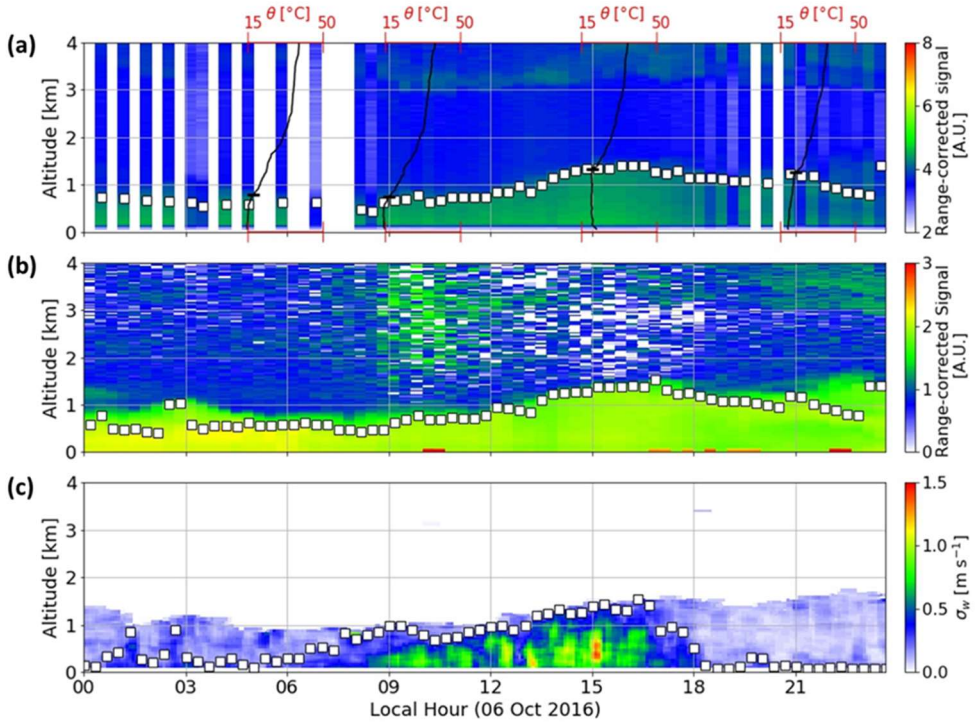


**Figure 4.7** Time-height plots for (a) lidar range-corrected lidar backscattered signals, (b) ceilometer backscattered signals, and (c) vertical wind speed standard deviation ($\sigma_w$) measured from WDL at the Jungnang site on 6 October 2016; MLH values from each instrument are plotted in white squares. Potential temperature profiles (solid black line) from radiosonde soundings are superimposed at the corresponding flight times and $MLH_{sonde}$ (horizontal dashes) in (a).

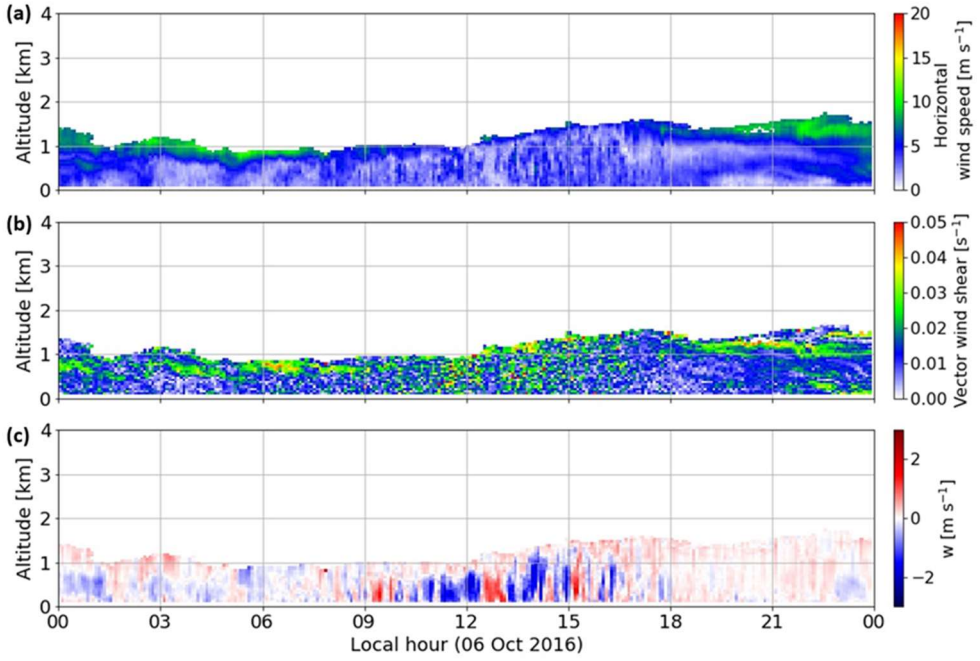


**Figure 4.8** Time-height plots for (a) horizontal wind speed, (b) vector wind shear, and (c) vertical wind speed measured from WDL at the Jungnang site on 6 October 2016.

To assess the extent to which model simulations of MLH correlate to the vertical distribution of aerosols, Weather Research and Forecasting/Chemistry model (WRF-Chem; Grell et al., 2005) simulation results of the MLH were evaluated through comparison with MLH determined from aerosol lidar and WDL measurements. The WRF-Chem model is a fully coupled “online” model widely used in the forecast and analysis of air quality issues (Sicard et al., 2021; Ukhov et al., 2021; Yahya et al., 2017). Simulation results from WRF-Chem version 3.8.1 conducted with three nested domains (27 km, 9 km, and 3 km grid spacing) were

used. For the planetary boundary layer (PBL) representation, the Yonsei University (YSU) PBL scheme (Hong et al., 2006) was employed, which has been reported to show good performance in former comparison studies (e.g., Cuchiara et al., 2014; Yerrailli et al., 2010). Detailed information on the model configurations used in this study is given in Lee et al. (2020).

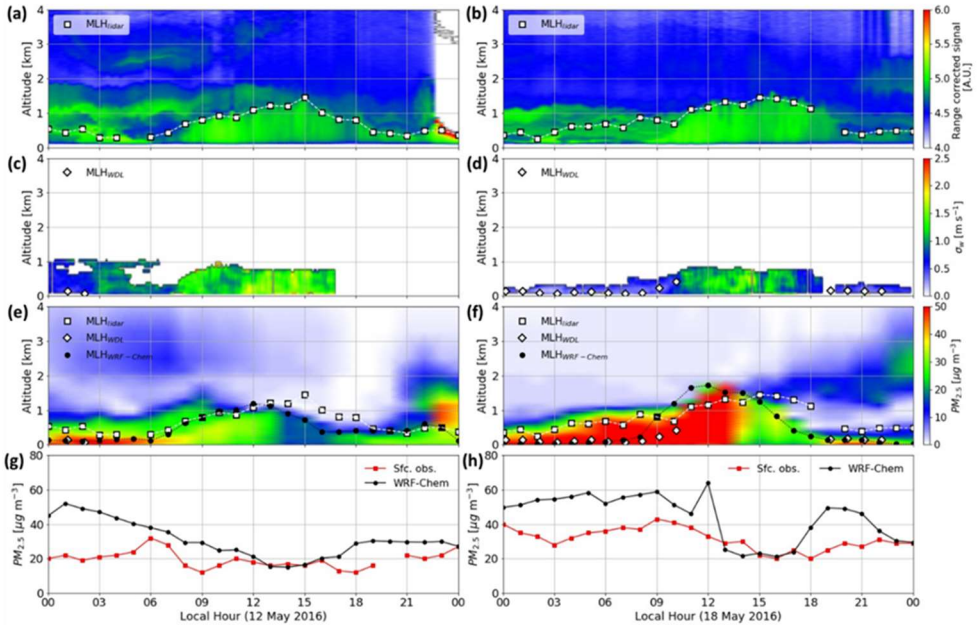


**Figure 4.9** (a, b) Time–height plots of aerosol $\beta$ signal and $MLH_{lidar}$. (c, d) Time–height plots of $\sigma_w$ and $MLH_{WDL}$. Lidar and WDL measurements from the SNU site. (e, f) Time-height plots of $PM_{2.5}$ concentration from WRF-Chem simulations with MLH. (g, f) Time series of $PM_{2.5}$ concentrations using ground-based measurements from the Sillim site and WRF-Chem simulations for 12 May 2016 (a, c, e, g) and 18 May 2016 (b, d, f, h).

**Figure 4.9** displays time-height plots of aerosol lidar $\beta$ (**Figures 4.9a** and **4.9b**) and WDL $\sigma_w$ (**Figures 4.9c** and **4.9d**) measurements from the SNU site with MLH retrieved using the corresponding methods for two cases (12 and 18 May 2016) during the Korea-United States Air Quality (KORUS-AQ) experiment (Crawford et al., 2021). Time-height plots of the WRF-Chem $PM_{2.5}$ concentration simulation results with $MLH_{WRF\text{-}Chem}$ extracted from the model grid embedding the SNU site are shown in **Figures 4.9e** and **4.9f**. The MLH from all observation and simulation datasets exhibited a clear diurnal pattern, i.e., developing after sunrise and decreasing with time throughout the afternoon, but the magnitude and time of the MLH peaks displayed some discrepancies. It should be noted that the $MLH_{WDL}$ was not retrieved at heights where the SNR of WDL was low due to low aerosol concentration, or where $\sigma_w$ exceeded the threshold value throughout the entire profile. Daytime MLH from WRF-Chem ($MLH_{WRF\text{-}Chem}$) displayed maximum heights similar to $MLH_{lidar}$, although the maximum $MLH_{WRF\text{-}Chem}$ were observed at 12 LST for both 12 and 18 May cases, while $MLH_{lidar}$ peaked at latter hours of 15 LST. This is consistent with the results given by Hegarty et al. (2018), which reported WRF-Chem MLH to have faster growth rates attributable to modeled thermodynamic terms such as buoyancy, therefore reaching its peak height earlier than $MLH_{lidar}$.

It is notable that the $MLH_{WRF\text{-}Chem}$ more closely resembles the

$MLH_{WDL}$ than $MLH_{lidar}$, especially during nighttime. $MLH_{WRF\text{-}Chem}$ at night displayed lower values compared to $MLH_{lidar}$. On 12 May 2016, the model simulated an average MLH of 0.12 km from 00 LST to 06 LST, while the aerosol lidar determined the MLH at higher altitudes (average = 0.58 km). Nighttime MLH for the 18 May 2016 case also showed lower values on the WRF-Chem part with a mean bias value of -0.30 km. Therefore, it could be deduced that although the WRF-Chem sufficiently simulates turbulent mixing induced by convection, it had difficulty simulating the nighttime vertical distribution of aerosols shown in lidar measurements. This, in part, corresponds to other studies that reported that MLH represented by aerosol lidars and ceilometers does not always correspond to thermodynamic mixing (Jiang et al., 2021; Ware et al., 2016). Furthermore, it can be deduced that the $\sigma_w$ and the bulk Richardson number display similar diurnal patterns, the latter being the variable with which the YSU PBL scheme defines MLH. Similar speculations were presented in Banakh et al. (2021), in which MLH determined from Doppler lidar measurements showed a good representation of temporal variations of turbulence observed from Richardson number time-height distributions.

Incorporating the former MLH intercomparison results with WRF-Chem simulated $PM_{2.5}$ vertical distribution, it was deduced that low nocturnal MLH by WRF-Chem led to the confined vertical distribution of

aerosols. As shown in **Figures 4.9e** and **4.9f**, $MLH_{WRF\text{-}Chem}$ coincides with heights where strong gradients of WRF-Chem $PM_{2.5}$ concentration exist. Therefore, it can be concluded that due to low MLH during nighttime, WRF-Chem simulations resulted in excessive vertical settling of aerosols and, therefore, overestimation of surface $PM_{2.5}$ concentrations. For verification, timeseries of WRF-Chem simulated $PM_{2.5}$ concentrations compared with surface $PM_{2.5}$ observations are presented in **Figures 4.9g** and **4.9h**. Surface $PM_{2.5}$ concentration measured at the Sillim site was used. The Sillim site is situated 3.6 km from the SNU site, 0.08 km lower in elevation. For the given cases, WRF-Chem overestimated surface $PM_{2.5}$ concentrations up to 270% compared to observation data, especially during nighttime. It is noteworthy to point out that for the case of 12 May 2016, WRF-Chem overestimation of surface $PM_{2.5}$ during 00 – 06 LST coincided with lower MLH relative to $MLH_{lidar}$, while better agreement between WRF-Chem and observed $PM_{2.5}$ during 18 – 24 LST was when $MLH_{WRF\text{-}Chem}$ displayed good correlation with $MLH_{lidar}$. Here, if WRF-Chem were to have simulated nocturnal vertical distribution of aerosols to heights corresponding to $MLH_{lidar}$, we can expect surface $PM_{2.5}$ mass concentration results to decrease. This is plausible since WRF-Chem simulated aerosol concentration above $MLH_{WRF\text{-}Chem}$ is smaller than the surface $PM_{2.5}$ concentrations, therefore, including this in the mixing process within the MLH will result in dilution of $PM_{2.5}$ near the surface.

The mean normalized bias of WRF-Chem compared to $PM_{2.5}$ concentration observations during the two case days was actually found to decrease from 52% to 19% when taking into account WRF-Chem simulated $PM_{2.5}$ profiles below the $MLH_{lidar}$ and assuming vertical dispersion of $PM_{2.5}$ within the ML defined by lidar. Significant improvement of surface $PM_{2.5}$ results was found at night, with the mean normalized bias of WRF-Chem compared to observations decreasing from 53% to 4%. Although lesser in degree, daytime $PM_{2.5}$ also displayed improvement with the use of $MLH_{lidar}$, with mean normalized bias slightly decreasing from 48% to 45%.

In conclusion, WRF-Chem was found to simulate reasonable MLH, especially during the daytime, when thermally driven turbulence induced vigorous vertical mixing of aerosols. However, aerosols were found to be relatively uniformly distributed up to higher heights than $MLH_{WRF\text{-}Chem}$ during nighttime, as shown by the significantly lower values of nocturnal MLH by WRF-Chem compared to $MLH_{lidar}$. To improve aerosol and air quality simulations, efforts to simulate a more realistic vertical distribution of aerosols are necessary. Therefore, direct measurements of the actual vertical distribution of aerosols, especially during nighttime, are essential to fully understand aerosol vertical variability.

### 4.2.2 Contribution of mixed layer and free tropospheric aerosols to AOD

Based on the MLH estimation method using aerosol lidar measurements described in Section 4.2.1, MLHs from the 2-year HSRL measurements in Seoul were retrieved. Using the MLH estimation and HSRL $\sigma_{ext}$ profiles, AODs within the BL ($AOD_{BL}$) and above the MLH ($AOD_{FT}$) were retrievable as the accumulated $\sigma_{ext}$ from the surface to the MLH and the MLH to 10 km altitude, respectively. **Figure 4.10** presents examples of the temporal variation of vertical aerosol distribution (represented by $\beta$) together with the $AOD_{BL}$ and $AOD_{FT}$ from 8 to 9 July 2016 and 20 to 21 October 2017. The MLH displayed a typical diurnal variation with low MLH (0.47 ± 0.14 km) during nighttime that gradually increased after sunrise (daytime mean 1.01 ± 0.52 km) for both cases. Meanwhile, AOD and the contribution of BL and FT aerosols of each case displayed significantly distinct diurnal patterns.

For the period 8–9 July 2016, afternoon cumulus clouds at the top of the BL were indicative of fair weather conditions leading to strong convection of aerosols and water vapor (Lareau et al., 2018; Zhan et al., 2021), favorable conditions for secondary aerosol formation. A maximum AOD was observed around noon (13 - 14 LST) and the rapid increase in the AOD after sunrise can be attributed to the active photochemical formation of secondary aerosols during summer in Seoul (Kim et al., 2016). The $AOD_{BL}$ constituted the majority of the AOD, with

mean $AOD_{BL}$ contributions to AOD of 77 ± 14%, notably larger than the 2-year average contribution of 52 ± 26%. The $AOD_{FT}$ nighttime contribution increased due to the residual aerosols above the BL after the breakdown of the MLH. Aerosols that remain in the residual layer are important for aerosol forecasting since they undergo different chemical and physical processes from BL aerosols and can affect surface aerosol concentrations and properties the following day (Curci et al., 2015; Lampilahti et al., 2021).

In comparison to the abovementioned period, the AOD displayed a smaller temporal variation throughout the period of 20–21 October 2017. However, the $AOD_{BL}$ displayed a clear diurnal pattern with a minimum of 0.05 ± 0.01 during nighttime and a maximum of 0.23 in the afternoon. Conversely, aerosols distributed above the nocturnal MLH and beneath 1.5 km contributed to the nighttime $AOD_{FT}$. Consequently, the $AOD_{FT}$ contribution to the nighttime AOD was 65 ± 21%, larger than the daytime mean (51 ± 20%). Additionally, an elevated aerosol layer observed between 6 to 8 km altitude at 13 LST on 20 October accounted for a mean and maximum AOD layer of 0.05 ± 0.02 and 0.07, respectively, resulting in a notably greater $AOD_{FT}$ contribution compared to the 2-year average (48 ± 26%). This aerosol layer was comprised of non-spherical dust particles with a mean depolarization ratio of 0.18 ± 0.02.

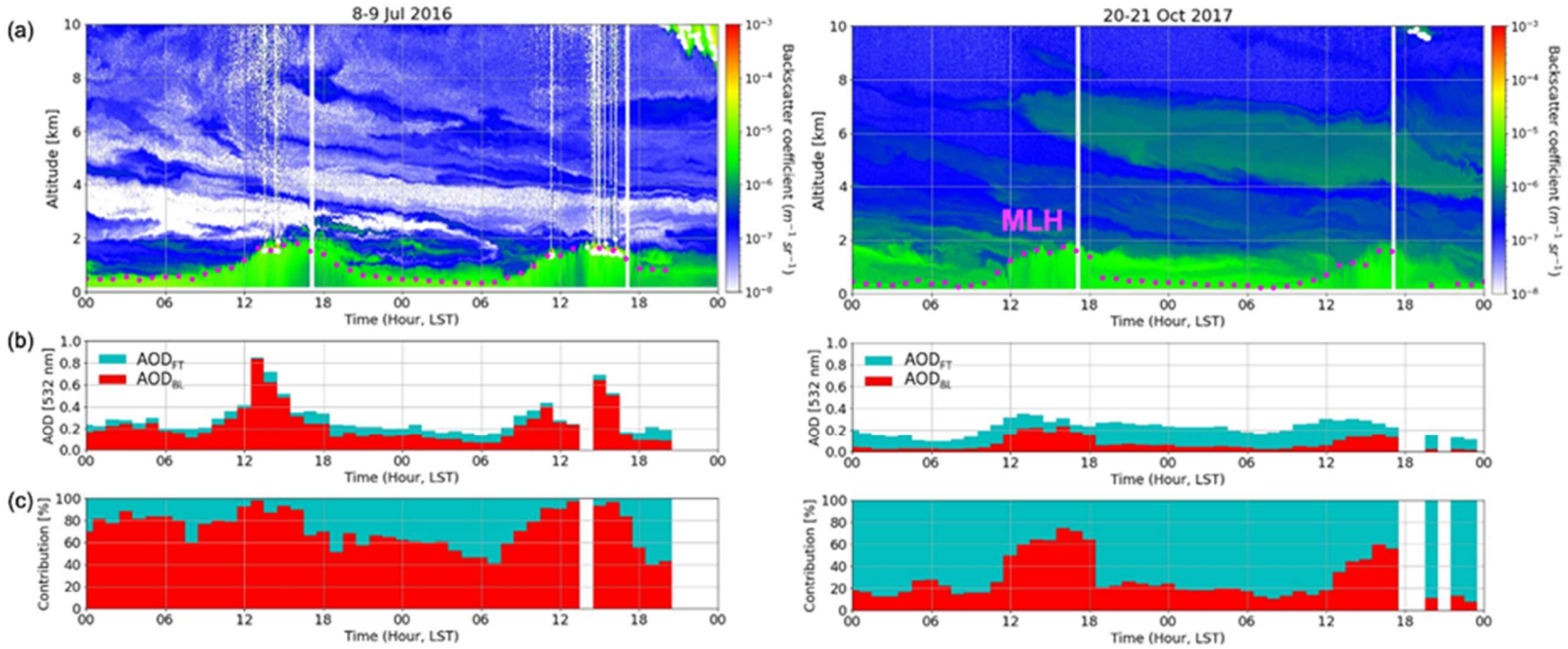


**Figure 4.10** (a) Time-height plots of HSRL backscatter coefficient overplotted with MLH (magenta) and CBH (white). (b) $AOD_{BL}$ and $AOD_{FT}$ timeseries, (c) Contribution of BL and FT aerosols to AOD. Left and right columns are for July 8 to 9 2016 and October 20 to 21 2017 cases, respectively.

The diurnal variation of $\sigma_{ext}$ and MLH from HSRL measurements from March 2016 to January 2018 is shown in **Figure 4.11a**. The MLH increased after sunrise to its peak height of 1.31 ± 0.34 km and decayed after sunset, displaying a nighttime MLH of 0.54 ± 0.17 km, consistent with previous MLH studies (Dang et al., 2019; Park et al., 2022). Aerosol extinction was dominant near the surface with an average 120% larger mean $\sigma_{ext}$ within the BL ($\sigma_{ext}^{BL}$), compared to that in the FT ($\sigma_{ext}^{FT}$). Hourly $\sigma_{ext}^{BL}$ was smallest around noon, with a mean of 0.21 $km^{-1}$ at 13 LST, attributable to the dilution of aerosols within the BL with the development of the MLH after sunrise (Dupont et al., 2016; Lee, J. et al., 2019). Nighttime $\sigma_{ext}^{FT}$ values in the MLH to 1.5 km altitude range were comparable to the mean $\sigma_{ext}^{BL}$ between 12 and 16 LST, indicative of the nocturnal residual layer in which aerosols that were previously dispersed by turbulence during daytime remain aloft (Stull, 1988).

**Figure 4.11b** displays the diurnal variation of the AOD partitioned to $AOD_{BL}$ and $AOD_{FT}$, based on the $\sigma_{ext}$ profiles in **Figure 4.11a**. The hourly $AOD_{BL}$ percent departure from the daily mean ranged from -38 to 42%, significantly larger than that of total column AOD (-13 to 11%). $AOD_{BL}$ displayed a similar diurnal variation with the MLH, with a maximum and minimum value of 0.26 ± 0.22 at 16 LST and 0.14 ± 0.17 at 21 LST, respectively. However, the correlation between $AOD_{BL}$ and MLH was insignificant ($R^2$ = 0.06), reflecting that the $AOD_{BL}$ is not simply

related to the BL depth but to other atmospheric variants, such as aerosol concentration, RH, or the light-extinction efficiency of aerosols within the BL.

The nighttime $AOD_{FT}$ contribution to the total column AOD was greater (57 ± 25%) than that during the daytime (41 ± 26%). Maximum and minimum FT contributions were observed at 21 LST (64 ± 21%) and 13 LST (29 ± 21%), respectively. The greater nighttime contribution can be attributed to residual layers existing above the MLH after the BL breakdown, as well as elevated aerosol layers, such as Asian dust, transported from upwind regions. Increases in the AOD of 81% and up to 265% from the average have been reported due to long-range transported aerosols in Korea (Lee, S. et al., 2021; Park et al., 2014). Due to the low nighttime MLH, transported aerosol layers contributed more notably to the enhancement of $AOD_{FT}$ during nighttime than daytime. These long-range transported aerosols display seasonality due to the varying synoptic patterns predominating over East Asia, resulting in the monthly variability of the $AOD_{FT}$ contribution.

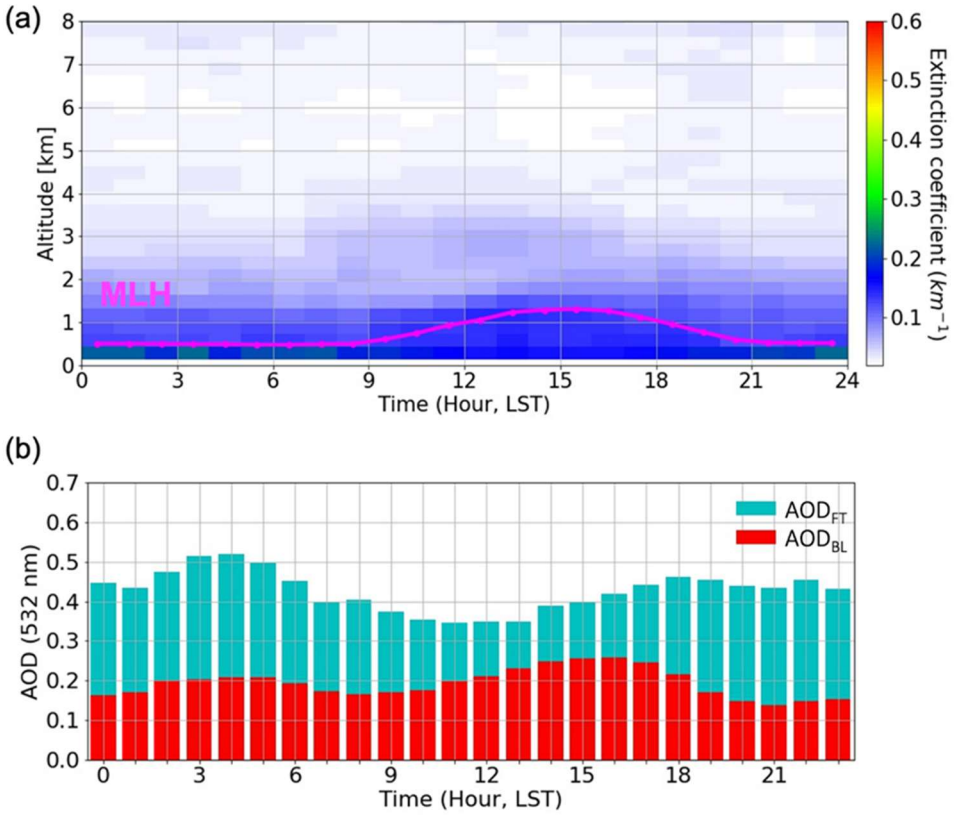


**Figure 4.11** (a) Diurnal variation of aerosol extinction coefficient by height overplotted with hourly mean MLH. (b) Diurnal variation of $AOD_{BL}$ and $AOD_{FT}$ retrieved from HSRL measurements (left y-axis) and hourly mean MLH and one standard deviation (right y-axis).

**Figure 4.12** shows the monthly variation of $\sigma_{ext}$ profiles and that of the AOD partitioned to the $AOD_{BL}$ and $AOD_{FT}$. Large $\sigma_{ext}$ in the BL and the lower FT were prominent during the summer months, resulting in a higher AOD, attributed to stagnant atmospheric conditions favorable for the build-up of pollutants, active formation of secondary aerosols, and hygroscopic growth of aerosols (Kim et al., 2007a; Kim, H. et al., 2014; Nam et al., 2018; Yang et al., 2020). The $AOD_{FT}$ contribution to AOD was

greatest in spring (MAM; 57%), attributable to the frequent transport of elevated dust particles. The depolarization ratio at 532 nm during spring (MAM) displayed overall larger values compared to the other seasons (**Figure 4.13**). In particular, mean depolarization ratios exceeding 0.15 above 3 km altitude were observed, signifying the existence of dust particles. Chen et al. (2009) reported a similarly high $AOD_{FT}$ contribution to AOD during spring (February–May) of 44–50% in Taipei, also due to dust transported from the Asian continent. Conversely, small depolarization ratios during summer indicate that the increase of AOD during the summer months was not related to dust particles, but rather to the formation of secondary aerosols and their hygroscopic growth due to favorable conditions provided by the humid air transported from the Northwestern Pacific (Yang et al., 2020).

Air masses of clean continental origin influence the study region during fall due to the transition of the prevailing wind direction (Kim et al., 2007a; Park, Kim, et al., 2019), resulting in a prominently smaller AOD. Despite frequent high pollution events during winter in Korea (Lee et al., 2011; Shim et al., 2022), both the $AOD_{BL}$ and $AOD_{FT}$ were observed to be lowest in winter. Days with daily mean AOD smaller than 0.1 were most frequently (up to 20%) observed during winter, which is attributable to clean continental air masses reaching the Korean peninsula under strong northwesterly winds from Siberia. Meanwhile, the standard deviation of

the daily mean AOD was greatest in winter, especially in December, with a maximum AOD standard deviation (mean and standard deviation = 0.36 ± 0.38), indicative of the occasional severe pollution events.

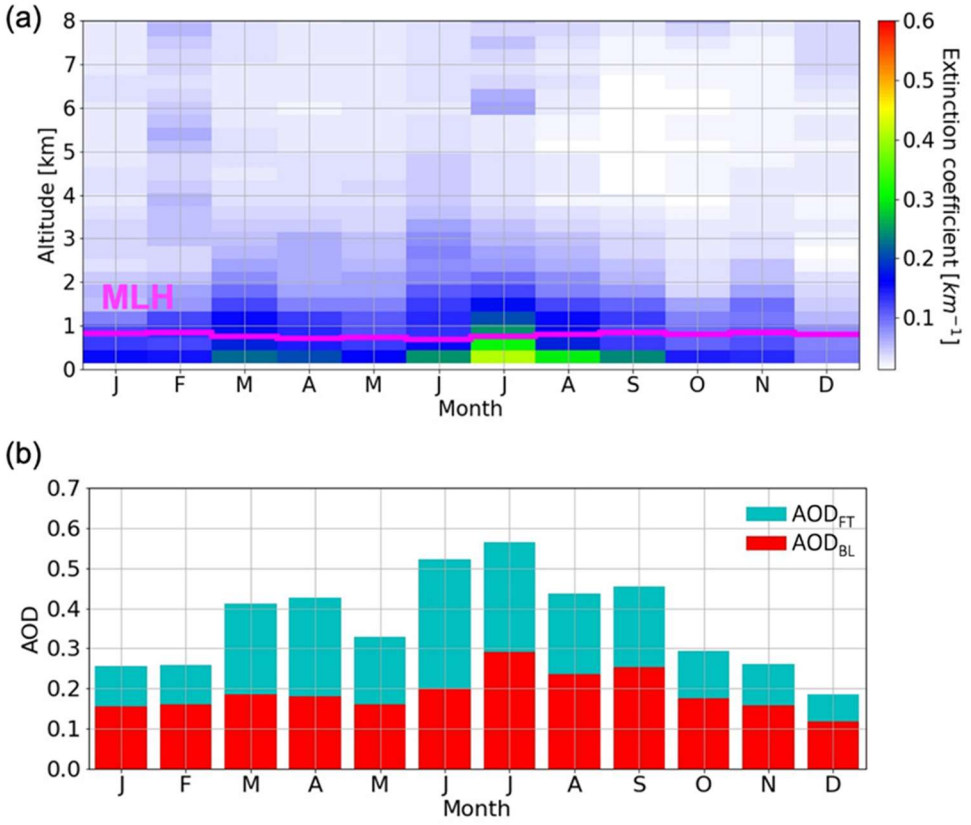


**Figure 4.12** (a) Monthly variation of aerosol extinction coefficient by height overplotted with monthly mean MLH and (b) Monthly variation of $AOD_{BL}$ and $AOD_{FT}$.

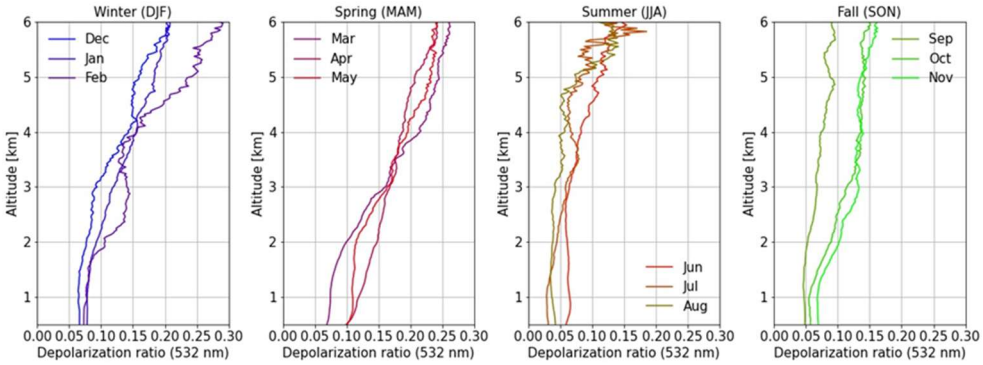


**Figure 4.13** Monthly mean profiles of HSRL depolarization ratio (532 nm).

Although AOD is widely used in evaluating air quality model performances, due to the complexity of aerosol vertical distribution (e.g. **Figures 4.11a** and **4.12a**), vertically-resolved measurements of the aerosol optical properties can provide information for further improvement. Accordingly, the relationship between $AOD_{BL}$ and surface PM concentrations was investigated (**Figure 4.14**). For a comprehensive comparison of the columnar AOD variable and PM mass loading, the $PM_{2.5}$ mass per area (i.e., column-integrated $PM_{2.5}$ mass concentration under the assumption that $PM_{2.5}$ is vertically well-mixed within the BL) was compared. Due to the vertical inhomogeneity of aerosols, the AOD and surface $PM_{2.5}$ displayed poor correlation. On the other hand, $AOD_{BL}$ displayed better correlation with surface $PM_{2.5}$ concentrations, implying that the $AOD_{BL}$ is a better indicator of the amount of aerosol loading near the surface. Thus, supporting the importance of accurate measurements

of the vertical distribution of aerosols to fully understand the relationship between columnar properties and surface air quality.

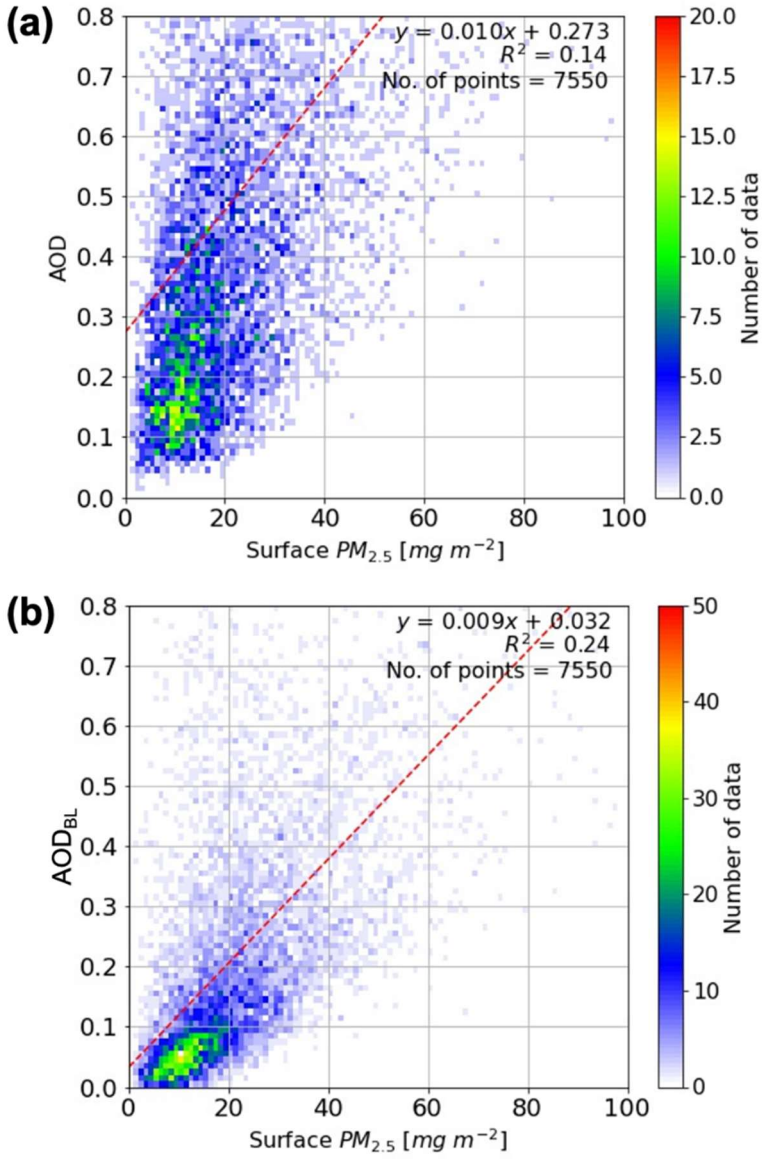


**Figure 4.14** (a) Scatterplot of AOD with $PM_{2.5}$ mass concentration scaled within the ML. (b) Scatterplot of $AOD_{BL}$ with $PM_{2.5}$ mass concentration scaled within the BL.

# Chapter 5 Aerosol mass concentration profiles from Lidar measurements

Studies investigating the feasibility of $PM_{2.5}$ concentration estimation with the use of passive satellite AOD have increased with the growing concern of air quality and health effects of $PM_{2.5}$ (van Donkelaar et al., 2015; Yan et al., 2017). However, lack of nighttime AOD and the complex vertical distribution of aerosols are factors that inhibit accurate definition of surface $PM_{2.5}$ to total column AOD relationship. A major factor used in relating satellite-derived AOD and surface PM concentrations is the height of the vertical mixing of aerosols. The mixing layer height is often taken from models, which is still a controversial element among modelers (Hoff and Christopher, 2009). Taking into account these issues, Toth et al. (2019) attempted to infer PM concentrations from CALIPSO near-surface aerosol extinction retrievals. Introducing a bulk mass scattering scheme to extinction retrievals from lidars, they successfully showed that near-surface CALIOP extinction data can be used to estimate surface $PM_{2.5}$ concentrations with reasonable accuracy. They also concluded that the combined use of several lidar instruments for monitoring regional and global PM pollution is potentially achievable.

Conversion of mass concentrations to their extensive optical properties (e.g., extinction, scattering, absorption, and AOD) is typically

needed when validating chemical transport models (CTMs) with lidar measurements (Andersson and Kahnert, 2016; Koffi et al., 2012; 2016). Uncertainties in aerosol optical property simulations of the model will affect the validation results of CTMs. Due to the large diversity in aerosol optical properties as a function of aerosol species (Kinne et al., 2005; Nemuc et al., 2013) and ambient relative humidity (RH; Pérez-Ramírez et al., 2021; Titos et al., 2021), measurement-based validation of the aerosol modules of CTMs is necessary (Hand and Malm, 2007; Saide et al., 2020).

In Section 3, the improvement of the retrieval of extinction coefficient from Mie-scattering lidar was discussed in conjunction with the understanding of the diverse vertical distribution of various aerosol types observed in Seoul. The diurnal variation of AOD including nighttime AOD in Seoul was investigated and discussed in Section 4.1 through HSRL measurements. Furthermore, the determination of the MLH, which is of importance to understand the vertical redistribution of aerosols near the surface, was implemented on Mie-scattering lidar and HSRL, and the characteristics of aerosols within the BL and FT were investigated. Major implications of the previous results can be found by additional calculation of PM mass concentration for its use in validating model simulation performances or input data for assimilation.

The relationship between the aerosol light extinction coefficient and aerosol mass is discussed in Section 5.1. An essential aerosol optical

property for converting the measured optical properties into aerosol mass concentration information is the mass extinction efficiency (MEE); Ansmann et al., 2012; Lin et al., 2015). MEE, defined as the amount of light extinction per mass concentration, depends on aerosol chemical composition, size distribution, and ambient humidity (Jung et al., 2018; Nemuc et al., 2013). MEE can be calculated using existing software that produces the microphysical and optical properties of designated aerosol types at given relative humidity (e.g. Optical Properties of Aerosol and Clouds; OPAC). MEE can also be directly inferred using extinction and mass concentration measurements. Although the total average MEE of aerosols observed in Seoul has been estimated by Kim et al. (2015) and Yeo et al. (2016), MEE by aerosol type is yet to be investigated.

Using the aerosol type-classification scheme defined in Section 3, we determined the aerosol type-specific MEE of $PM_{10}$ by dividing the HSRL $\sigma_{ext}^{BL}$ with ground-based $PM_{10}$ concentration observations assuming that the atmosphere within the BL was thoroughly mixed. Since the HSRL measures the $\sigma_{ext}$ of aerosols of all sizes, $PM_{10}$ observations were used instead of $PM_{2.5}$ concentration.

## 5.1 Mass extinction efficiency from lidar and in-situ measurements

Aerosols emitted from near the surface are well-mixed within the

boundary layer. From the $AOD_{BL}$ defined in Section 4.2, the MEE for aerosols in Seoul was estimated using surface $PM_{10}$ concentrations obtained from ground-based in-situ measurements 3.6 km from the SNU site (Sillim site; www.airkorea.or.kr).

**Figure 5.1a** shows the frequency distribution of all $PM_{10}$ MEE values from March 2016 to January 2018. The median MEE of 4.28 $m^2\ g^{-1}$ was larger than the values presented by Kim et al. (2015; 3.69 ± 3.0 $m^2\ g^{-1}$) and Yeo et al. (2016; 3.36 ± 2.42 $m^2\ g^{-1}$), who used $\sigma_{ext}$ from Mie-scattering lidar measurements and surface $PM_{10}$ observations in Seoul to calculate MEE. Meanwhile, Joo et al. (2022) reported similar MEE values (5.7–7.3 $m^2\ g^{-1}$ for 2016 and 2017 in Seoul) using visibility and surface $PM_{10}$ observations. An increasing trend in MEE between 2001 and 2020 (0.15 $m^2\ g^{-1}\ yr^{-1}$) was also reported by Joo et al. (2022), implying a change in aerosol particle size and composition in Seoul. Dust aerosols displayed the smallest MEE values, followed by clean aerosols (**Figure 5.1b**). Pollution aerosols displayed the largest light extinction efficiencies, consistent with previous literature (Kim et al., 2021).

The variability of MEE under various conditions was investigated based on frequency distributions of MEE binned by the $PM_{2.5}$ to $PM_{10}$ ratio (i.e. $PM_{2.5}$ concentration divided by $PM_{10}$ concentration; **Figure 5.1c**) and season (**Figure 5.1d**). MEE values displayed an increasing trend with respect to an increasing $PM_{2.5}$ to $PM_{10}$ ratio, indicating that under a fixed

$PM_{10}$ concentration, larger $\sigma_{ext}$ will be observed when smaller particles (i.e., $PM_{2.5}$) are more abundant. This is expected since the extinction efficiency of $PM_{2.5}$ is larger than that of $PM_{10}$ in the Mie-scattering regime (Willeke and Brockmann, 1977). The $PM_{2.5}$ to $PM_{10}$ ratio can also qualitatively describe the relative abundance of dust particles; the lower the $PM_{2.5}$ to $PM_{10}$ ratio, the more marked the contribution of dust particles (Sugimoto et al., 2016). Dust particles are reported to have a smaller MEE (smaller than 1 $m^2\ g^{-1}$) than that of pollution and smoke aerosols (Clarke et al., 2004; Nemuc et al., 2013), which also explains the smaller MEE in the low $PM_{2.5}$ to $PM_{10}$ ratio ranges.

MEE displayed the largest mean values in summer, followed by fall, winter, and spring (**Figure 5.1d**) which shared similar MEE distributions with modal MEE ranging between 3.0–3.5 $m^2\ g^{-1}$. Yet, MEE smaller than 2 $m^2\ g^{-1}$ were most dominant during spring due to the frequent influence of dust aerosols. In summer, the MEE distribution notably shifted towards larger values compared to the other seasons. This is demonstrated in **Figure 5.2** which depicts how MEE increases with RH, whereas high ambient RH conditions most frequently occur during summer.

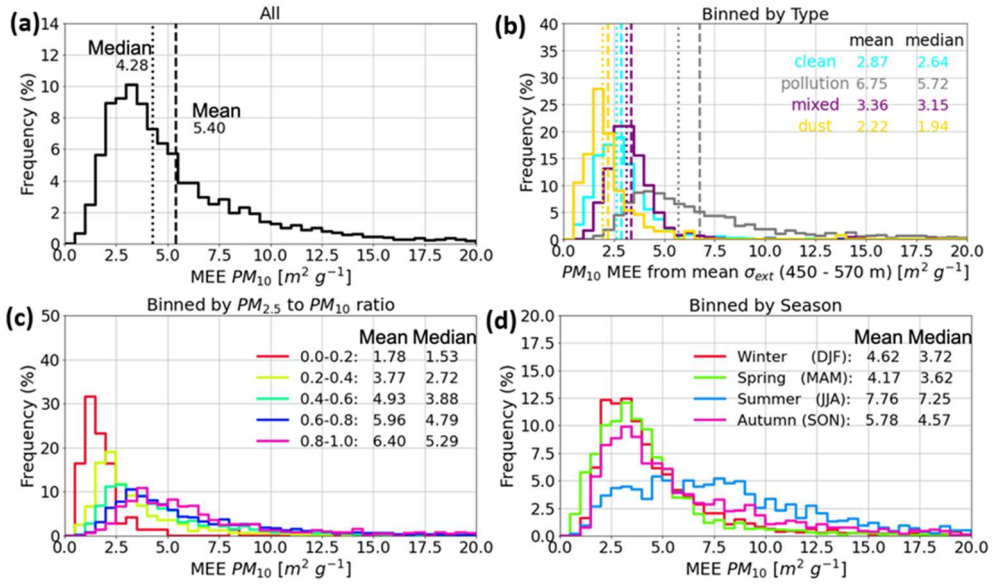


**Figure 5.1** Histograms of (a) $PM_{10}$ MEE, (b) aerosol type-specific $PM_{10}$ MEE, (c) $PM_{10}$ MEE by $PM_{2.5}$ to $PM_{10}$ ratio, and (d) $PM_{10}$ MEE by season.

Since hygroscopic growth of aerosols is a main factor in increasing aerosol extinction, we can expect that MEE retrieved in this study is sensitive to relative humidity (RH; %). Therefore, the seasonal MEE distribution by RH was investigated (**Figure 5.2**). MEE increased with RH since humid conditions are favorable for the hygroscopic growth of aerosols that result in enhanced light extinction efficiency. The slope of RH to MEE differed by season which can be attributed to the fact that the hygroscopic growth factor is dependent on aerosol composition and its hygroscopicity (Li et al., 2021; Pan et al., 2009).

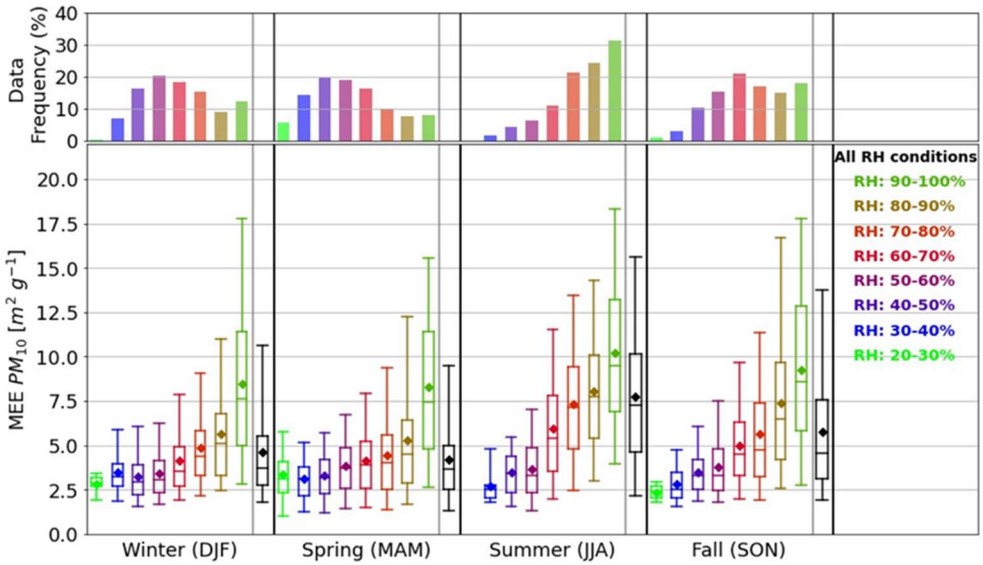


**Figure 5.2** The distribution of data frequency and $PM_{10}$ MEE binned by each RH decile by season. All box plots are color-coded by RH conditions. Whiskers indicate 5 and 95 percentiles, boxes indicate 25, 50, and 75 percentiles and markers indicate the mean MEE values.

The hygroscopicity of aerosols vary by its chemical composition and consequently, aerosol type (Pérez-Ramírez et al., 2021; Titos et al., 2021). Therefore, the distribution of aerosol type-specific MEE and its relationship with ambient RH conditions was investigated (**Figure 5.3**). Dust, which is constituted mainly of hydrophilic compositions (Wu et al., 2020), displayed the smallest variability with RH. MEE of pollution aerosols was found to increase up to 300% with increasing RH.

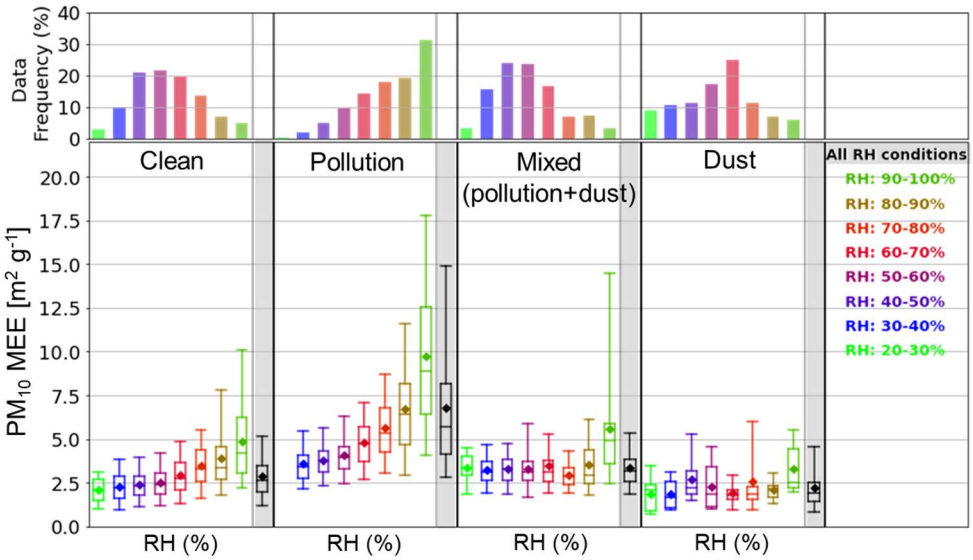


**Figure 5.3** The distribution of data frequency and $PM_{10}$ MEE binned by each RH decile by aerosol type. All box plots are color-coded by RH conditions. Whiskers indicate 5 and 95 percentiles, boxes indicate 25, 50, and 75 percentiles and markers indicate the mean MEE values.

**Table 5.1** Look-up table of the MEE of $PM_{10}$ specified by aerosol type and ambient RH conditions.

| Aerosol type / RH range | Clean | Pollution | Mixed | Dust |
|---|---|---|---|---|
| **Total** | **2.87** | **6.75** | **3.36** | **2.22** |
| 20% ≤ RH < 30% | 2.11 | 2.85 | 3.36 | 1.87 |
| 30% ≤ RH < 30% | 2.26 | 3.57 | 3.22 | 1.83 |
| 40% ≤ RH < 30% | 2.39 | 3.79 | 3.26 | 2.72 |
| 50% ≤ RH < 30% | 2.51 | 4.05 | 3.27 | 2.30 |
| 60% ≤ RH < 30% | 2.90 | 4.82 | 3.46 | 1.90 |
| 70% ≤ RH < 30% | 3.50 | 5.61 | 2.93 | 2.59 |
| 80% ≤ RH < 30% | 3.91 | 6.71 | 3.55 | 2.09 |
| 90% ≤ RH < 30% | 4.88 | 9.71 | 5.57 | 3.28 |

As shown in **Figures 5.2** and **5.3**, the MEE of $PM_{10}$ observed in Seoul displays strong dependency on the ambient RH and aerosol type. **Table 5.1** shows the specific MEE values of type-specific $PM_{10}$ under varying RH conditions. The values given in **Table 5.1** can serve as a look-up table for MEE values of aerosols in the area around Seoul.

## 5.2 Estimating surface PM mass concentration from lidar observations

To assess the uncertainty of estimating surface $PM_{10}$ concentrations from aerosol optical properties using MEE, $PM_{10}$ concentration was estimated by applying the respective MEE values under different conditions to the HSRL $\sigma_{ext}^{BL}$ and validated the results with surface $PM_{10}$ observations (**Figure 5.4**). Applying a single MEE value (the total average) for $PM_{10}$ concentration estimation showed the largest Mean Normalized Bias (MNB) of 10.6%. Improved $PM_{10}$ estimates were achieved when applying the seasonal mean MEE to each corresponding measurement (MNB = 9.0%; **Figure 5.4b**). A further MNB decrease was found when MEE, depending on the RH condition, was used in $PM_{10}$ estimation (MNB = 6.4%; **Figure 5.4c**), indicating that the estimated $PM_{10}$ error is more sensitive to RH MEE dependency than the seasonal variation of MEE. Applying the RH-dependent MEE within each season resulted in an even smaller NMB between the estimated and observed $PM_{10}$ concentration

(NMB = 6.2%; **Figure 5.4d**).

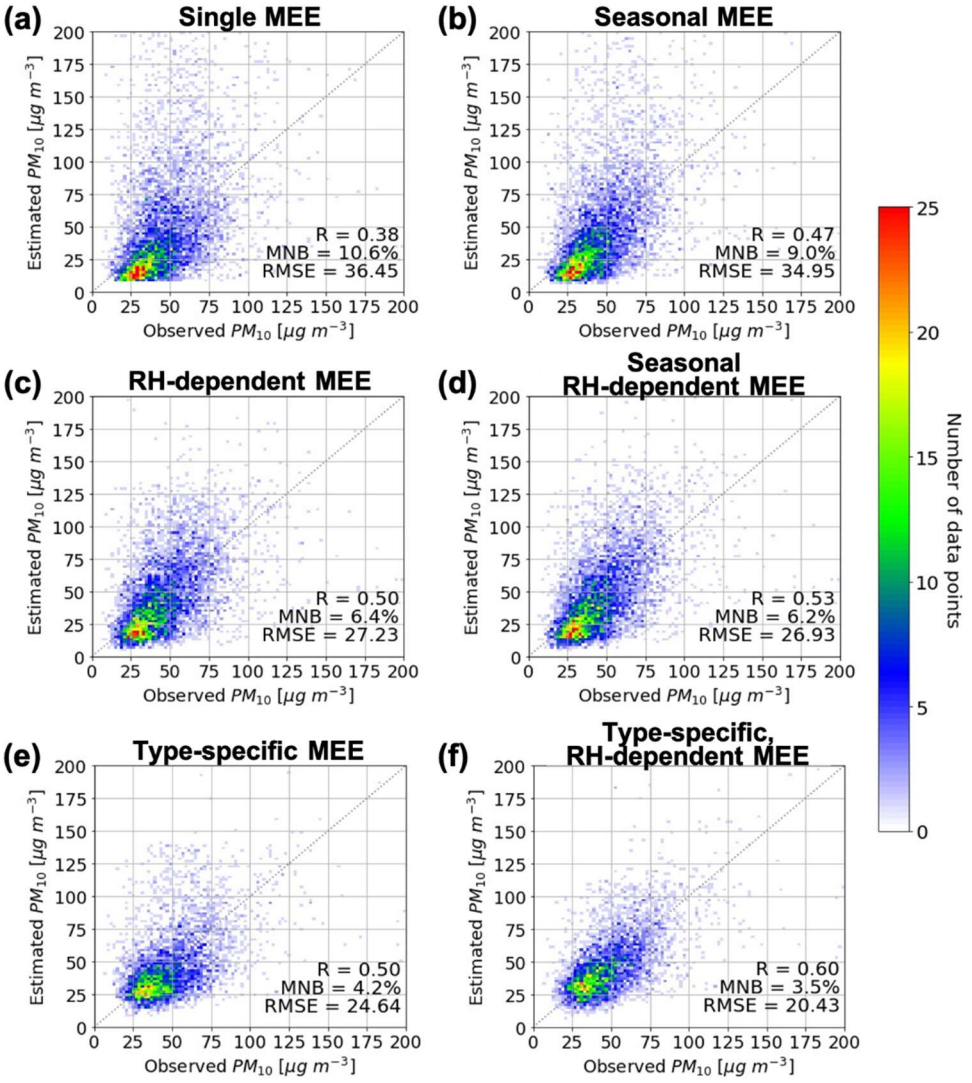


**Figure 5.4** (a) Observed (x-axis) and estimated (y_axis) $PM_{10}$ concentration using a single MEE value; (b), (c), (d), (e), and (f) the same as (a) except the y-axis indicates estimated $PM_{10}$ concentration using MEE values depending on season, RH, seasonal RH, type, and type-RH, respectively.

While Seoul is influenced by aerosols from various sources (e.g., Asian dust, industrial pollution, vehicle emissions, smoke aerosols, etc.), depending on the seasonally varying meteorological conditions (Kim et al., 2022; Seo et al., 2017; Shim et al., 2022), aerosol types are known to vary intra-seasonally in Seoul. Therefore, applying seasonal MEE cannot sufficiently account for the different aerosol optical properties of intra-seasonally-varying aerosol types. Further improvements in the estimation of surface $PM_{10}$ concentrations from lidar measurements were achieved by applying aerosol type-dependent MEE to HSRL measurements (**Figures 5.4e** and **5.4f**).

Estimating surface $PM_{10}$ concentration using the HSRL $\sigma_{ext}^{BL}$ and RH-dependent type-specific MEE (**Figure 5.4f**; mean bias = -1.23 μg $m^{-3}$) showed smaller mean biases compared to a similar study in Seoul (Yeo et al., 2016), which estimated surface $PM_{10}$ from Mie-scattering lidar $\sigma_{ext}$ with a single MEE value (mean bias = -2.75 μg $m^{-3}$). It is noted that the MNBs of this study were lower than that reported by Seo et al. (2015), where estimated surface $PM_{10}$ concentration using AERONET AOD in Seoul by empirical linear models showed MNBs greater than 20%. Instead of columnar measurements, the use of vertically resolved measurements of aerosol optical properties is more appropriate for estimating surface $PM_{10}$ concentration. Compared to Mie-scattering lidar measurements, the use of HSRL data, which contains fewer uncertainties

in the retrieval of $\sigma_{ext}$, can give more accurate estimates of surface $PM_{10}$ concentration. Meanwhile, underestimation of $PM_{10}$ concentration can occur in conditions when the gradient of $\sigma_{ext}$ within the BL is large, due to discrepancies between the surface $\sigma_{ext}$ and mean BL $\sigma_{ext}$.

In conclusion, the application of HSRL $\sigma_{ext}$ and the newly defined aerosol type-specific and RH-dependent MEE for the retrieval of $PM_{10}$ concentrations, provides considerably enhanced performance of PM mass concentration retrieval using remote sensing observations, with an expected MNB of 3.5%. Therefore, MEE values reported in **Table 5.1** were applied to actual HSRL $\sigma_{ext}$ profiles to investigate the $PM_{10}$ mass concentrations vertical distribution and discuss its characteristics in comparison with the temporal variability of $\sigma_{ext}$ profiles discussed in Section 4.2.2. The HSRL signals were classified into each aerosol type using the flowchart of **Figure 3.3**. Here, hourly RH profiles from the 5$^{th}$ generation of European Centre for Medium-Range Weather Forecasts (ECMWF) Reanalysis dataset (ERA5; Hersbach et al., 2020) were used in considering the RH dependency of aerosol type-specific MEE.

**Figure 5.5** shows the $PM_{10}$ concentrations profiles over SNU during 13 – 15 April 2016, calculated from HSRL measurements. As displayed in **Figure 3.6**, the majority of aerosols within the boundary layer were pollution aerosols. Elevated layers of dust and mixed aerosols were observed above the boundary layer during 00 – 06 LST 14 April and 12 –

21 LST 15 April, respectively. It is characteristic that the mass concentration of the elevated aerosol layers exceeds that within the boundary layer. More specifically, the mean concentration of the elevated dust layer on 14 April was 57 μg $m^{-3}$, while the elevated pollution and dust-mixed aerosols on 15 April displayed mean concentrations of 71 μg $m^{-3}$. These concentrations were comparable to the mean surface $PM_{10}$ during the 13 – 15 April period of 62 μg $m^{-3}$.

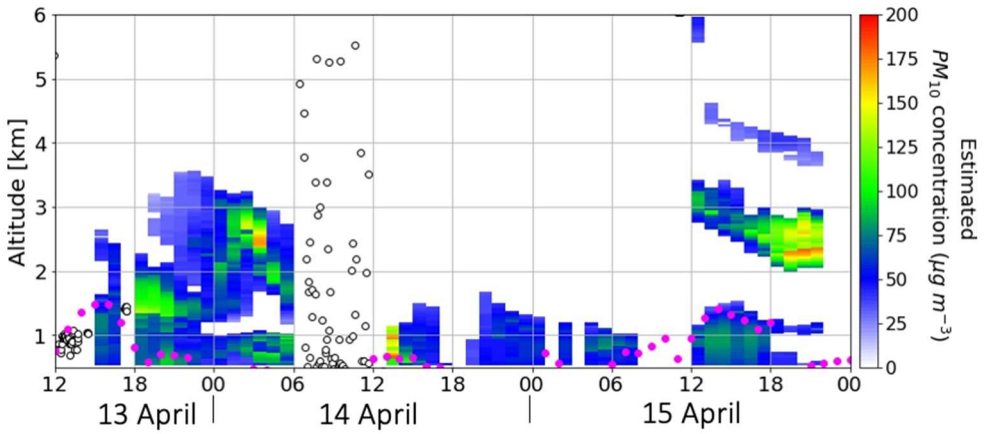


**Figure 5.5** Time-height plots of estimated $PM_{10}$ concentrations from HSRL observations during 13 – 15 April 2016. CBHs and MLHs are overplotted in white and magenta, respectively.

The monthly variation of $PM_{10}$ concentration profiles retrieved from the two-year HSRL measurements is shown in **Figure 5.6a**. Maximum $PM_{10}$ concentration near the surface is observed during spring, especially in March and April. Distinctly large $PM_{10}$ values are observed up to higher altitudes during these months, which can be attributed to the elevated

transboundary dust aerosols. High $PM_{10}$ concentrations were also observed at high altitudes during June and July, which can be the result of stronger turbulence near the surface induced by increased solar radiation. Conversely, $PM_{10}$ was confined within lower altitudes during the winter months as a result of limited thermal convection near the surface. Meanwhile, September and December displayed the smallest mean $PM_{10}$ concentration. The September minimum coincides with the surface in-situ $PM_{2.5}$ and $PM_{10}$ fall minima displayed in **Figure 5.7**. However, the December low $PM_{10}$ observed in the HSRL profile estimations was not apparent in the surface in-situ $PM_{10}$ measurements. This discrepancy can be explained by the limited PM calculation conditions from HSRL measurements. i.e., when HSRL extinction profiles were excluded from the calculation due to low-level clouds.

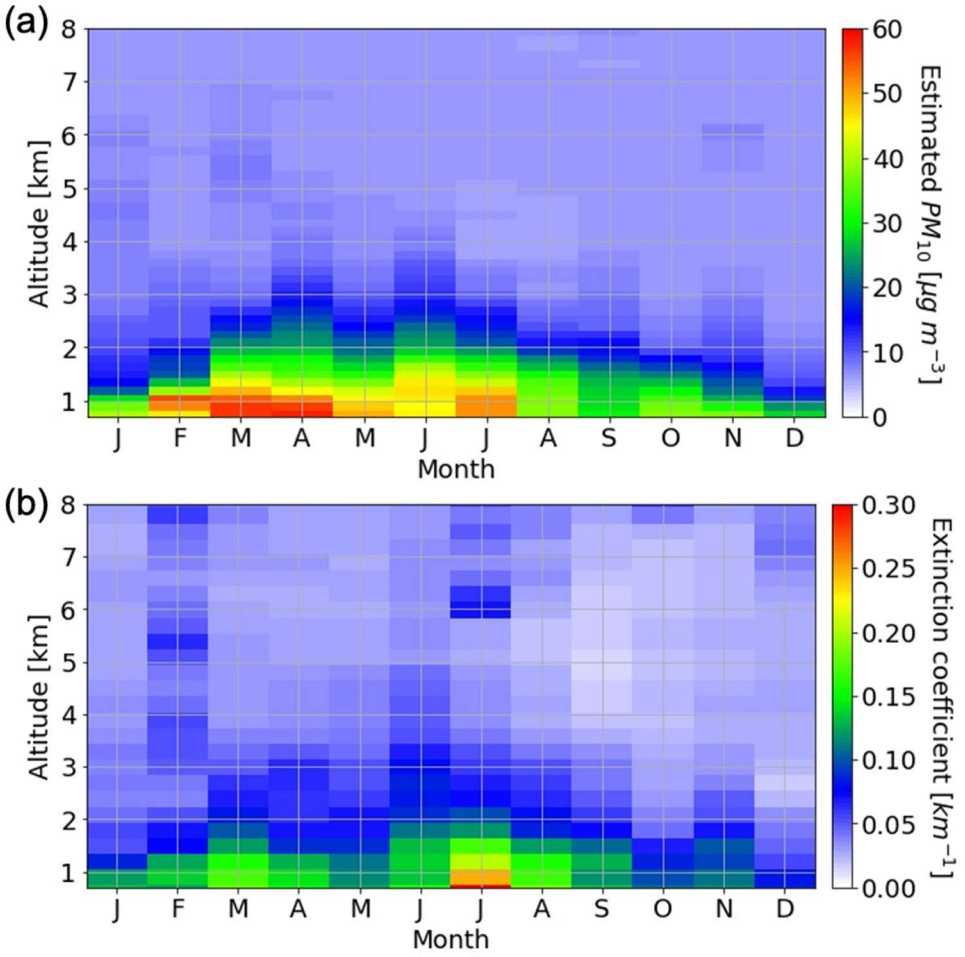


**Figure 5.6** Monthly variation of (a) estimated $PM_{10}$ concentration profiles and (b) extinction coefficient profiles from HSRL observations from March 2016 to January 2018.

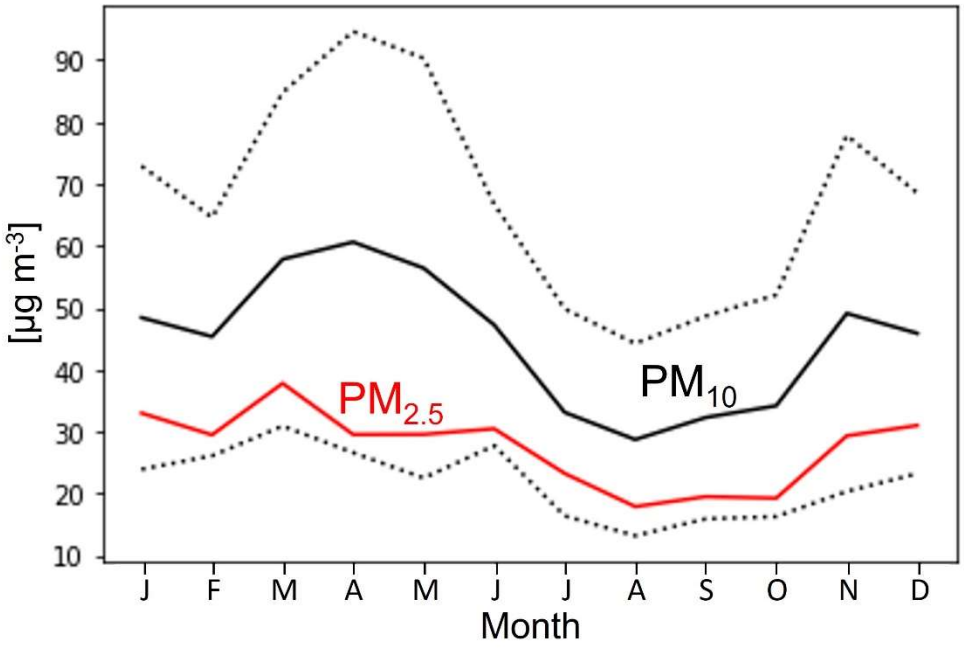


**Figure 5.7** Monthly mean surface $PM_{10}$ (in black) and $PM_{2.5}$ (in red) observed by ground in-situ measurements from the AirKorea Sillim site in Seoul. Dotted black lines represent the one standard deviation from the means.

Meanwhile, the monthly patterns of $PM_{10}$ concentration exhibited different characteristics from that of aerosol extinction coefficient profiles as shown in **Figure 5.6b**. While aerosols were observed to be the most optically thick (i.e., large extinction coefficients) during summer, the mass concentration was not the largest. On the contrary, due to the small mass extinction efficiencies of dust and mixed aerosols, which were most frequently observed during spring, the extinction coefficients were smaller than those in summer, despite the spring maximum in $PM_{10}$ concentration.

As can be expected from the large variability of MEE, consideration of the various factors such as atmospheric conditions (e.g., RH, season) and aerosol characteristics (e.g., size distribution, aerosol type) must be preceded when inferring the mass concentrations from observed extensive aerosol optical properties. Accurate projections of the PM mass concentrations in the upper atmosphere from lidar measurements will be beneficial in evaluating and improving chemical transport model simulations. Furthermore, it is speculated that operational retrievals of the PM mass concentration profiles will provide valuable information on the elevated aerosol masses for surface air quality forecast.

# Chapter 6 Summary and further directions

Due to the heterogeneity in emission sources, aerosol types and their optical properties show large variability by region. Aerosol type-classification from remote sensing measurements has been a long-continuing issue in retrieving accurate properties of aerosols. Therefore, accurate aerosol classification including the environmental characteristics is essential in obtaining accurate aerosol retrievals through remote sensing measurements. Although many studies have investigated lidar ratio values, existing publications on aerosols in East Asia have mostly focused on dust. The lidar ratio for pollution (anthropogenic) and other dominant aerosol types in Seoul is important for increasing the accuracy of aerosol extinction coefficient calculation.

A 23-month deployment of the University of Wisconsin-Madison High Spectral Resolution Lidar (HSRL) alongside a Mie-scattering lidar on the campus of Seoul National University (SNU), Korea, has opened the opportunity to improve the accuracy of Mie-scattering lidar measurements. The HSRL technique enables direct measurements of backscatter and extinction coefficients, lidar ratios, and nighttime AOD which were used to define parameters that are needed in improving extinction coefficient retrieval methods, and in validating the results.

From continuous HSRL measurements, the lidar ratio of typical

aerosol types in Seoul (i.e., pollution, dust, pollution, and dust mixture) were determined. Using collocated surface $PM_{2.5}$ and $PM_{10}$ measurements as references to the aerosol type, an aerosol type classification scheme based on the HSRL backscatter coefficient and depolarization ratio measurements was determined. The resulting type-specific lidar ratio values were reported to be 48 sr, 57 sr, 42 sr, and 49 sr for clean continental particles, pollution particles, dust particles, and mixed particles, respectively. Extinction coefficients from Mie-scattering lidar were retrieved by implementing an objective method of aerosol classification based on Mie-scattering lidar observations and applying type-specific lidar ratios in the extinction coefficient retrieval process. Compared to the primitive extinction coefficient retrieval method, which utilizes a single lidar ratio despite varying aerosol types, errors in aerosol extinction coefficient retrievals were reduced by 7 $Mm^{-1}$ when evaluated with the collocated HSRL measurements. The reported decrease in extinction coefficient mean bias from -0.026 $km^{-1}$ to -0.019 $km^{-1}$ leads to an error reduction of 0.042 in AOD (approximately 10% of the mean AOD in Seoul).

The temporal variability of AOD, including nighttime AOD, was investigated using the 2-year continuous HSRL measurements, and the contributions of boundary layer (BL) and free troposphere (FT) aerosols to AOD were estimated. HSRL AOD compared with simultaneous

AERONET AOD observations showed good agreement, with an $R^2$ value of 0.87 and a mean bias of -0.00. The diurnal variation of AOD was found to peak at 04 LST and gradually decrease to its minimum at 13 LST. Mean daytime AOD displayed lower values than nighttime AOD, (0.40 and 0.45, respectively) greatly due to nighttime conditions favorable to the hygroscopic growth of aerosols. The difference in daytime/nighttime AOD was found to lead to significant differences in the daily mean AOD described by 24-hour measurements of the HSRL and daytime measurements of AERONET.

Unlike the diurnal variation of AOD, the AOD of BL aerosols ($AOD_{BL}$) was found to peak at 15 LST and its diurnal variation resembled the diurnal variation of MLH, displaying lower values at night and its peak around 14-15 LST. However, when comparing the $AOD_{BL}$ with MLH point by point, low correlation was found ($R^2$ = 0.06), indicating that day-to-day aerosol concentration within the BL displayed significantly different temporal variability with the MLH. The contribution of BL aerosols to AOD displayed a similar diurnal variation to that of $AOD_{BL}$ with larger BL contribution during daytime (42 ± 22%) than during nighttime (27 ± 21%). Although $AOD_{BL}$ was largest around noon, the mean extinction coefficient within the BL ($AOD_{BL}$ divided by MLH) decreased during the daytime, demonstrating the dilution of aerosols due to enhanced mixing as the MLH develops during the day.

AOD in summer was observed to be largest, followed by spring, fall and was lowest AOD in winter. Although the mean AOD in winter was the smallest, outliers displayed large AOD values comparable to those of all the other seasons. This implies that although the overall AOD in winter was low, high AOD events with values comparable to any other season still occurred. Higher $AOD_{BL}$ and $AOD_{FT}$ were observed during summer, which could be attributed to the hygroscopic growth of aerosols due to high humidity. A larger contribution of FT aerosols to AOD was found during spring that coincided with larger depolarization ratio values between 2 – 6 km, indicating the frequent existence of elevated dust layers.

Using surface $PM_{10}$ concentrations and the mean extinction coefficient within the BL, the mass extinction efficiency (MEE) of $PM_{10}$ aerosols in Seoul was investigated. MEE showed mean and median values of 5.40 and 4.28 $m^2\ g^{-1}$, respectively. The behaviour of aerosol type-specific MEE with ambient relative humidity was also investigated. Due to the low hygroscopicity of dust aerosols, dust, and mixed aerosol MEE displayed a weak correlation with RH. On the other hand, pollution and clean aerosols displayed strong enhancement of MEE with increasing RH. The estimation results of $PM_{10}$ concentrations using lidar measurements and MEE values were evaluated with surface $PM_{10}$ measurements. Uncertainty of estimating surface $PM_{10}$ concentrations was smallest

when applying different MEE values for each aerosol type and by relative humidity (mean normalized bias decreased from 10.6% to 3.5%).

While an in-depth discussion on the full diurnal variation of aerosol optical properties in Seoul, Korea was presented using HSRL measurements throughout this thesis, the short duration of the HSRL's deployment in Seoul leaves us with the task to expand the study to investigate the climatological characteristics of aerosols in Seoul using the Mie-scattering lidar measurements from 2006. The newly defined type-specific lidar ratios and MEE values, specific for aerosols in Seoul, can lead to elaborate retrievals of the long-term temporal variability of aerosol extinction coefficient profiles, AOD, and the vertical distribution of PM mass concentrations.

# References


Allen, R.J., Landuyt, W., Rumbold, S.T. (2016). An increase in aerosol burden and radiative effects in a warmer world. *Nature Climate Change*, 6, 269-274. https://doi.org/10.1038/nclimate2827

Al-Saadi, J., Carmichael, G., Crawford, J., Emmons, L., Kim, S., Song, C. K., et al. (2015). NASA contributions to KORUS-AQ: An international cooperative air quality field study in Korea, https://espo.nasa.gov/korus-aq/content/KORUS-AQ_Science_Overview_0, Accessed 22 May 2023.

Andersson, E. and Kahnert, M. (2016). Coupling aerosol optics to the MATCH (v5.5.0) chemical transport model and the SALSA (v1) aerosol microphysics module. *Geoscientific Model Development*, 9, 1803-1826. https://doi.org/10.5194/gmd-9-1803-2016

Anderson, T. L., Masonis, S. J., Covert, D. S., Charlson, R. J. (2000). In situ measurement of the aerosol extinction-to-backscatter ratio at a polluted continental site. *Journal of Geophysical Research*. 105(D22), 26907-26915. https://doi.org/10.1029/2000JD900400

Ansmann, A. and Müller, D. (2005). Lidar and Atmospheric Aerosol Particles, in: Lidar: Range-Resolved Optical Remote Sensing of the Atmosphere, 1st edn., edited by: Weitkamp, C., vol. 102 of Springer Series in Optical Sciences, 105-141, Springer, New York, New York, USA.

Ansmann, A., Seifert, P., Tesche, M., Wandinger, U. (2012). Profiling of fine and coarse particle mass: case studies of Saharan dust and Eyjafjallajökull/Grimsvötn volcanic plumes. *Atmospheric Chemistry and Physics*, 12, 9399-9415. https://doi.org/10.5194/acp-12-9399-2012

Banakh, V. A., Smalikho, I. N., Falits, A. V. (2021). Estimation of the height of turbulent mixing layer from data of Doppler lidar measurements using conical scanning by a probe beam. *Atmospheric Measurement Techniques*, 14, 1511–1524. https://doi.org/10.5194/amt-14-1511-2021

Barbaro, E., Arellano, V. G., Krol, M. C., Holtslag, A. A. (2013). Impacts of aerosol shortwave radiation absorption on the dynamics of an idealized convective atmospheric boundary layer. *Bound-Layer Meteorology*, 148, 31-49. https://doi.org/10.1007/s10546-013-9800-7

Barlow, J. F., Dunbar, T. M., Nemitz, E. G., Wood, C. R., Gallagher, M. W., Davies, F., et al. (2011). Boundary layer dynamics over London, UK, as observed using Doppler lidar during REPARTEE-II. *Atmospheric Chemistry and Physics*, 11, 2111–2125. https://doi.org/10.5194/acp-11-2111-2011

Barreto. A., Cuevas, E., Damiri, B., Guirado, C., Berkoff, T., Berjón, A. J., et al. (2013). A new method for nocturnal aerosol measurements with a lunar photometer prototype. *Atmospheric Measurement Techniques*, 6, 585-598. https://doi.org/10.5194/amt-6-585-2013

Berjón, A., Barreto, A., Hernández, Y., Yela, M., Toledano, C., Cuevas, E. (2019). A 10-year characterization of the Saharan Air Layer lidar ratio in the subtropical North Atlantic. *Atmospheric Chemistry and Physics*, 19, 6331-6349. https://doi.org/10.5194/acp-19-6331-2019

Berkoff, T. A., Sorokin, M., Stone, T., Eck, T. F., Raymond, H., Welton, E., Holben, B. (2011). Nocturnal Aerosol Optical Depth Measurements with a Small-Aperture Automated Photometer Using the Moon as a Light Source. *Journal of Atmospheric and Oceanic Technology*, 28, 1297-1306. https://doi.org/10.1175/JTECH-D-10-05036.1

Bréon, F. -M. (2013). Aerosol extinction-to-backscatter ratio derived from passive satellite measurements. *Atmospheric Chemistry and Physics*, 13, 8947-8954. https://doi.org/10.5194/acp-13-8947-2013

Brooks, I. M. (2003). Finding Boundary Layer Top: Application of a Wavelet Covariance Transform to Lidar Backscatter Profiles. *Journal of Atmospheric and Oceanic Technology*, 20, 1092-1105. https://doi.org/10.1175/1520-0426(2003)020<1092:FBLTAO>2.0.CO;2

Burton, S. P., Ferrare, R. A., Hostetler, C. A., Hair, J. W., Rogers, R. R., Obland, M. D., et al. (2012). Aerosol classification using airborne High Spectral Resolution Lidar measurements – methodology and examples. *Atmospheric Measurement Techniques*, 5, 73-98. https://doi.org/10.5194/amt-5-73-2012

Burton, S. P., Ferrare, R. A., Vaughan, M. A., Omar, A. H., Rogers, R. R., Hostetler, C. A., Hair, J. W. (2013). Aerosol classification from airborne HSRL and comparisons with the CALIPSO vertical feature mask. *Atmospheric Measurement Techniques*, 6, 1397-1412. https://doi.org/10.5194/amt-6-1397-2013

Caicedo, V., Rappenglück, B., Lefer, B., Morris, G., Toledo, D., Delgado, R. (2017). Comparison of aerosol lidar retrieval methods for boundary layer height detection using ceilometer aerosol backscatter data. *Atmospheric Measurement Techniques*, 10, 1609–1622. https://doi.org/10.5194/amt-10-1609-2017

Campbell. J. R., Tackett, J. L., Reid, J. S., Zhang, J., Curtis, C. A., Hyer, E. J., et al. (2012). Evaluating nighttime CALIOP 0.532 μm aerosol optical depth and

extinction coefficient retrievals. *Atmospheric Measurement Techniques,* 5, 2143-2160. https://doi.org/10.5194/amt-5-2143-2012

Chaikovsky, A., Dubovik, O., Holben, B., Bril, A., Goloub, P., Tanré, D., et al. (2016). Lidar-Radiometer Inversion Code (LIRIC) for the retrieval of vertical aerosol properties from combined lidar/radiometer data: development and distribution in EARLINET. *Atmospheric Measurement Techniques*, 9, 1181-1205. https://doi.org/10.5194/amt-9-1181-2016

Chen, W. -N., Chen, Y. -W., Chou, C. C. K., Chang, S. -Y., Lin, P. -H., Chen, J. -P. (2009). Columnar optical properties of tropospheric aerosol by combined lidar and sunphotometer measurements at Taipei, Taiwan. *Atmospheric Environment*, 43(17), 2700-2708. https://doi.org/10.1016/j.atmosenv.2009.02.059

Choo, G. -H., and Jeong, M. -J. (2016). Estimation of nighttime aerosol optical thickness from Suomi-NPP DNB observations over small cities in Korea. *Korean Journal of Remote Sensing*, 32(2), 73-86. https://doi.org/10.7780/KJRS.2016.32.2.1. (In Korean with an English Abstract.)

Clarke, A. D., Shinozuka, Y., Kapustin, V. N., Howell, S., Huebert, B., Doherty, S., et al. (2004). Size distributions and mixtures of dust and black carbon aerosol in Asian outflow: Physiochemistry and optical properties. *Journal of Geophysical Research: Atmospheres*, 109, D15S09. https://doi.org/10.1029/2003JD004378

Compton, J. C., Delgado, R., Berkoff, T. A., Hoff, R. M. (2013). Determination of Planetary Boundary Layer Height on Short Spatial and Temporal Scales: A Demonstration of the Covariance Wavelet Transform in Ground-Based Wind Profiler and Lidar Measurements. *Journal of Atmospheric and Oceanic Technology*, 30, 1566-1575. https://doi.org/10.1175/JTECH-D-12-00116.1

Crawford, J. H., Ahn, J. -Y., Al-Saadi, J., Chang, L., Emmons, L. K., Kim, J., et al. (2021). The Korea-United States Air Quality (KORUS-AQ) field study. *Elementa Science of the Anthropocene*, 9 (1), 00163. https://doi.org/10.1525/elementa.2020.00163

Cuchiara, G. C., Li, X., Carvalho, J., Rappenglück, B. (2014). Intercomparison of planetary boundary layer parameterization and its impacts on surface ozone concentration in the WRF/Chem model for a case study in Houston/Texas. *Atmospheric Environment*, 96, 175–185. https://doi.org/10.1016/j.atmosenv.2014.07.013

Curci, G., Ferrero, L., Tuccella, P., Barnaba, F., Angelini, F., Bolzacchini, E., et al. (2015). How much is particulate matter near the ground influenced by upper-level processes within and above the PBL? A summertime case study in Milan (Italy) evidences the distinctive role of nitrate. *Atmospheric Chemistry and Physics*, 15(5), 2629–2649. https://doi.org/10.5194/acp-15-2629-2015

Dang, R., Yang, Y., Hu, X. -M., Wang, Z., Zhang, S. (2019). A review of techniques for diagnosing the atmospheric boundary layer height (ABLH) using aerosol lidar data. *Remote Sensing*, 11, 1590. https://doi.org/10.3390/rs11131590

Davis, K. J., Gamage, N., Hagelberg, C. R., Kiemle, C., Lenschow, D. H., Sullivan, P. P. (2000). An objective method for deriving atmospheric structure from airborne lidar observations. *Journal of Atmospheric and Oceanic Techniques*, 17, 1455–1468. https://doi.org/10.1175/1520-0426(2000)017<1455:AOMFDA>2.0.CO;2

Dong, Z., Li, Z., Yu, X., Cribb, M., Li, X., Dai, J. (2017). Opposite long-term trends in aerosols between low and high altitudes: a testimony to the aerosol-PBL feedback. *Atmospheric Chemistry and Physics*, 17: 7997-8009. https://doi.org/10.5194/acp-17-7997-2017

Du, C., Liu, S., Yu, X., Li, X., Chen, C., Peng, Y., et al. (2013). Urban boundary layer height characteristics and relationship with particulate matter mass concentrations in Xi'an, Central China. *Aerosol Air Quality Research*, 13, 1598–1607. https://doi.org/10.4209/aaqr.2012.10.0274

Dupont, J.-C., Haeffelin, M., Badosa, J., Elias, T., Favez, O., Petit, J. E., et al. (2016). Role of the boundary layer dynamics effects on an extreme air pollution event in Paris. *Atmospheric Environment*, 141, 571–579. https://doi.org/10.1016/j.atmosenv.2016.06.061

Düsing, S., Ansmann, A., Baars, H., Corbin, J. C., Denjean, C., Gysel-Beer, M., et al. (2021). Measurement report: Comparison of airborne, in situ measured, lidar-based, and modeled aerosol optical properties in the central European background - identifying sources of deviations. *Atmospheric Chemistry and Physics*, 21, 16745-16773. https://doi.org/10.5194/acp-21-16745-2021

Eck, T. F., Holben, B. N., Reid, J. S., Arola, A., Ferrare, R. A., Hostetler, C. A., et al. (2014). Observations of rapid aerosol optical depth enhancements in the vicinity of polluted cumulus clouds. *Atmospheric Chemistry and Physics*, 14, 11633-11656. https://doi.org/10.5194/acp-14-11633-2014

Eck, T. F., Holben, B. N., Reid, J. S., Dubovik, O., Smirnov, A., O'Neill, N. T., et al. (1999). Wavelength dependence of the optical depth of biomass burning, urban and desert dust aerosols. *Journal of Geophysical Research*. 104(D24), 31333-31349. https://doi.org/10.1029/1999JD900923

Eloranta, E. (2014). High Spectral Resolution lidar Measurements of atmospheric extinction: Progress and challenges. IEEE. 1-6. doi: 10.1109/AERO.2014.6836214.

Eloranta, E. (2018). Extinction measurements with low-power HSRL systems—error limits. *EPJ Web Conference*, 176, 05011, DOI: 10.1051/epjconf/201817605011.

Fernald, F. K. (1984). Analysis of atmospheric lidar observations: some comments. *Applied Optics*. 41(30), 6470-6476. https://doi.org/10.1364/AO.23.000652

Ferrare, R. A., Turner, D. D., Brasseur, L. H., Feltz, W. F., Dubovik, O., Tooman, T. P. (2001). Raman lidar measurements of the aerosol extinction-to-backscatter ratio over the Southern Great Plains. *Journal of Geophysical Research*, 106(D17), 20333-20347. https://doi.org/10.1029/2000JD000144

Floutsi, A. A., Baars, H., Engelmann, R., Althause, D., Ansmann, A., Bohlmann, S., et al. (2023). DeLiAn – a growing collection of depolarization ratio, lidar ratio and Angstrom exponent for different aerosol types and mixtures from ground-based lidar observations. *Atmospheric Measurement Techniques*, 16, 2353-2379. https://doi.org/10.5194/amt-16-2353-2023

Freudenthaler, V. M., Esselborn, M. Wiegner, B. Heese, M. Tesche, A. Ansmann, D., et al. (2009). Depolarization ratio profiling at several wavelengths in pure Saharan dust during SAMUM 2006. *Tellus B*, 61, 165-179. https://doi.org/10.1111/j.1600-0889.2008.00396.x

Garratt, J.R. (1992). The Atmospheric Boundary Layer. Cambridge University Press, Cambridge, UK.

Giles, D. M., Sinyuk, A., Sorokin, M. G., Schafer, J. S., Smirov, A., Slutsker, I., et al. (2019). Advancements in the Aerosol Robotic Network (AERONET) Version 3 database – automated near-real-time quality control algorithm with improved cloud screening for Sun photometer aerosol optical depth (AOD) measurements. *Atmospheric Measurement Techniques*, 12, 169-209. https://doi.org/10.5194/amt-12-169-2019

Gonçalves, W. A., Machado, L. A. T., Kirstetter, P. -E. (2015). Influence of biomass aerosol on precipitation over the Central Amazon: an observational study.

*Atmospheric Chemistry and Physics*, 15, 6789-6800. https://doi.org/10.5194/acp-15-6789-2015

Grell, G. A., Peckham, S. E., Schmitz, R., McKeen, S. A., Frost, G., Skamarock, W. C., Eder, B. (2005). Fully coupled "online" chemistry within the WRF model. *Atmospheric Environment*, 39, 6957–6975. https://doi.org/10.1016/j.atmosenv.2005.04.027

Guo, H., Cheng, T., Gu, X., Wang, Y., Chen, H., Bao, F., et al. (2017). Assessment of $PM_{2.5}$ concentrations and exposure throughout China using ground observations. *Science of the Total Environment*. 601-602, 1024-1030. https://doi.org/10.1016/j.scitotenv.2017.05.263

Haman, C. L., Lefer, B., Morris, G. A. (2012). Seasonal variability in the diurnal evolution of the boundary layer in a near-coastal urban environment. *Journal of Atmospheric and Oceanic Technology*, 29 (5), 697–710. https://doi.org/10.1175/JTECH-D-11-00114.1

Hand, J. L. and Malm, W. C. (2007). Review of aerosol mass scattering efficiencies from ground-based measurements since 1990. *Journal of Geophysical Research: Atmospheres*, 112, D16203. https://doi.org/10.1029/2007JD008484

Hegarty, J. D., Lewis, J., McGrath-Spangler, E. L., Henderson, J., Scarino, A. J., DeCola, P., et al. (2018). Analysis of the Planetary Boundary Layer Height during DISCOVER-AQ Baltimore-Washington, D. C., with Lidar and High-Resolution WRF Modeling. *Journal of Applied Meteorology and Climatology*, 57, 2679-2696. https://doi.org/10.1175/JAMC-D-18-0014.1

Hersbach, H., Bell, B., Berrisford, P., Hirahara, S., Horányi, A., Muñoz-Sabater, J., et al. (2020). The ERA5 global reanalysis. *Quarterly Journal of the Royal Meteorological Society*, 146, 1999-2049. https://doi.org/10.1002/qj.3803

Hofer, J., D. Althausen, S. F. Abdullaev, A. N. Makhmudov, B. I. Nazarov, G. Schettler, R., et al. (2017). Long-term profiling of mineral dust and pollution aerosol with multiwavelength polarization Raman lidar at the Central Asian site of Dushanbe, Tajikistan: case studies, *Atmospheric Chemistry and Physics*, 17, 14559-14577. https://doi.org/10.5194/acp-17-14559-2017

Hoff, R. M., and Christopher, S. A. (2009). Remote sensing of particulate pollution from space: have we reached the promised land?. *Journal of the Air and Waste Management Association*. 59(6), 645-675. https://doi.org/10.3155/1047-3289.59.6.645

Holben, B. N., Eck, T. F., Slutsker, I., Tanré, D., Buis, J. P., Setzer, A., et al. (1998). AERONET – A Federated Instrument Network and Data Archive for Aerosol Characterization. *Remote Sensing of Environment*, 66(1), 1-16. https://doi.org/10.1016/S0034-4257(98)00031-5

Hong, S. Y., Noh, Y., Dudhia, J. (2006). A New Vertical Diffusion Package with an Explicit Treatment of Entrainment Processes. *Monthly Weather Review*. 134, 2318-2341. https://doi.org/10.1175/MWR3199.1

Hubert, L. and Arabie, P. (1985). Comparing partitions. *Journal of Classification*, 2, 193-218. https://doi.org/10.1007/BF01908075

Hung, W. -T., Lu, C. -H., Shrestha, B., Lin, H. -C., Lin, C. -A., Grogan, D., et al. (2020). The impacts of transported wildfire smoke aerosols on surface air quality in New York State: A case study in summer 2018. *Atmospheric Environment*, 227, 117415. https://doi.org/10.1016/j.atmosenv.2020.117415

Jeon, W., Lee, H. W., Lee, T. -J,. Yoo, J. -W., Mun, J., Lee, S. -H., Choi, Y. (2019). Impact of Varying Wind Patterns on $PM_{10}$ Concentrations in the Seoul Metropolitan Area in South Korea from 2012 to 2016. *Journal of Applied Meteorology and Climatology*, 58, 2743-2754. https://doi.org/10.1175/JAMC-D-19-0102.1

Jiang, Y., Xin, J., Zhao, D., Jia, D., Tang, G., Quan, J., et al. (2021). Analysis of differences between thermodynamic and material boundary layer structure: comparison of detection by ceilometer and microwave radiometer. *Atmospheric Research*, 248, 105179. https://doi.org/10.1016/j.atmosres.2020.105179

Jo, H. -Y., Lee, H. -J., Jo, Y. -J., Lee, J. -J., Ban, S., Lee, J. -J., et al. (2019). Nocturnal fine particulate nitrate formation by $N_2O_5$ heterogeneous chemistry in Seoul Metropolitan Area, Korea. *Atmospheric Research*, 225, 58-69. https://doi.org/10.1016/j.atmosres.2019.03.028

Johnson, R. S., Zhang, J., Hyer, E. J., Miller, S. D., Reid, J. S. (2013). Preliminary investigations toward nighttime aerosol optical depth retrievals from the VIIRS Day/Night Band. *Atmospheric Measurement Techniques*. 6, 1245-1255. https://doi.org/10.5194/amt-6-1245-2013

Joo, S., Dehkhoda, N., Shin, J., Park, M. E., Sim, J., Noh, Y. (2022). A study on the long-term variations in mass extinction efficiency using visibility data in South Korea. *Remote Sensing*, 14(7), 1592. https://doi.org/10.3390/rs14071592

Jordan, C. E., Crawford, J. H., Beyersdorf, A. J., Eck, T. F., Halliday, H. S., Nault, B. A., et al. (2020). Investigation of factors controlling $PM_{2.5}$ variability across the South Korean Peninsula during KORUS-AQ. *Elementa Science of the Anthropocene*, 8, 28. https://doi.org/10.1525/elementa.424

Jung, C. H., Um, J., Bae, S. Y., Yoon, Y. J., Lee, S. S., Lee, J. Y., Kim, Y. P. (2018). Analytic expression for the aerosol mass efficiencies for polydispersed accumulation mode. *Aerosol and Air Quality Research*, 18(6), 1503–1514. https://doi.org/10.4209/aaqr.2018.02.0067

Kang, H., Zhu, B., van der A, R. J., Zhu, C., de Leeuw, G., Hou, X., Gao, J. (2019). Natural and anthropogenic contributions to long-term variations of $SO_2$, $NO_2$, CO and AOD over East China, *Atmospheric Research*, 215, 284-293. https://doi.org/10.1016/j.atmosres.2018.09.012

Kim, H. -S., Chung, Y. -S., Kim, J. -T. (2014). Spatio-temporal variations of optical properties of aerosols in East Asia measured by MODIS and relation to the ground-based mass concentrations observed in Central Korea during 2001~2010. *Asia-Pacific Journal of Atmospheric Sciences*, 50(2), 191–200. https://doi.org/10.1007/s13143-014-0007-8

Kim, H., Kim, J. Y., Jin, H. C., Lee, J. Y., Lee, S. P. (2016). Seasonal variations in the light-absorbing properties of water-soluble and insoluble organic aerosols in Seoul, Korea. *Atmospheric Environment*, 129, 24-242. https://doi.org/10.1016/j.atmosenv.2016.01.042

Kim, H., Zhang, Q., Heo, J. (2018). Influence of intense secondary aerosol formation and long-range transport on aerosol chemistry and properties in the Seoul Metropolitan Area during spring time: results from KORUS-AQ. *Atmospheric Chemistry and Physics*, 18, 7149-7168. https://doi.org/10.5194/acp-18-7149-2018

Kim, M. -H., Kim, S. -W., Yoon, S. -C., Sugimoto, N., Sohn, B. -J. (2011). Characteristics of the Lidar Ratio Determined from Lidar and Sky Radiometer Measurements in Seoul. *Atmosphere*. 21(1), 57-67. (In Korean with English Abstract)

Kim, M. -H., Yeo, H., Sugimoto, N., Lim, H. -C., Lee, C. -K., Heo, B. -H., et al. (2015). Estimation of particle mass concentration from lidar measurement. *Atmosphere*. 25(1), 169-177. (In Korean with English Abstract)

Kim, M. -H., Omar, A. H., Tackett, J. L., Vaughan, M. A., Winker, D. M., Trepte, C. R., et al. (2018). The CALIPSO Version 4 Automated Aerosol Classification and Lidar Ratio Selection Algorithm. *Atmospheric Measurement Techniques*, 11, 6107-6135. https://doi.org/10.5194/amt-11-6107-2018

Kim, M. -H., Kim, S. -W., Omar, A. H. (2020). Dust Lidar Ratios Retrieved from the CALIPSO Measurements Using the MODIS AOD as a Constraint. *Remote Sensing*, 12(2), 251. https://doi.org/10.3390/rs12020251

Kim, S., Hong, K. -H., Jun, H., Park, Y. -J., Park, M., Young, S. (2014). Effect of Precipitation on Air Pollutant Concentration in Seoul, Korea. *Asian Journal of Atmospheric Environment,* 8(4), 202-211. Doi: http://dx.doi.org/10.5572/ajae.2014.8.4.202

Kim, S. -W., Yoon, S. -C., Kim, J., Kim, S. -Y. (2007a). Seasonal and monthly variations of columnar aerosol optical properties over east Asia determined from multi-year MODIS, LIDAR, and AERONET Sun/sky radiometer measurements. *Atmospheric Environment*, 41, 1634-1651. https://doi.org/10.1016/j.atmosenv.2006.10.044

Kim, S. -W., Yoon, S. -C., Won, J. -G., Choi, S. -C. (2007b). Ground-based remote sensing measurements of aerosol and ozone in an urban area: A case study of mixing height evolution and its effect on ground-level ozone concentrations. *Atmospheric Environment*, 41, 7069-7081. https://doi.org/10.1016/j.atmosenv.2007.04.063

Kim, S. -W., Yoon, S. -C., Kim, J., Kang, J. -Y., Sugimoto, N. (2010). Asian dust event observed in Seoul, Korea during 29-31 May 2008: Analysis of transport and vertical distribution of dust particles from lidar and surface measurements. *Science of the Total Environment*, 408, 1707-1718. DOI: 10.1016/j.scitotenv.2009.12.018

Kim, S. -W., Heo, J., Kim, J. Y. (2022). $PM_{2.5}$ source apportionment in Seoul, Korea: a comparison of PMF and SMP receptor modelling results. *International Journal of Environmental Science and Technology*, https://doi.org/10.1007/s13762-022-04183-y

Kim, T., Joo, S., Kim, G., Noh, Y. (2021). The Study of $PM_{10}$, $PM_{2.5}$ Mass Extinction Efficiency Characteristics Using LIDAR Data. *Korean Journal of Remote Sensing,* 37, 1793-1801. https://doi.org/10.7780/kjrs.2021.37.6.2.2 (In Korean with English Abstract)

Kinne, S., Schulz, M., Textor, C., Guibert, S., Balkanski, Y., Bauer, S. E., et al. (2006). An AeroCom initial assessment – Optical properties in aerosol component modules of global models. *Atmospheric Chemistry and Physics*, 6(7), 1815–1834. https://doi.org/10.5194/acp-6-1815-2006

Klett, J. D., (1981). Stable analytical inversion solution for processing lidar returns. *Applied Optics*, 20(2), 211-220. https://doi.org/10.1364/AO.20.000211

Klett, J. D., (1985). Lidar Inversion with Variable/Extinction Ratios, *Applied Optics*, 24, 1638. https://doi.org/10.1364/AO.24.001638

KMA. (2022). Guidelines for Surface Weather Observations (Korean). https://data.kma.go.kr/resources/images/publication/%EC%A7%80%EC%83%81%EA%B8%B0%EC%83%81%EA%B4%80%EC%B8%A1%EC%A7%80%EC%B9%A8(2022.12.).pdf. Accessed 23 July 2023.

Koffi, B., Schulz, M., Bréon, F. -M., Griesfeller, J., Winker, D., Balkanski, Y., et al. (2012). Application of the CALIOP layer product to evaluate the vertical distribution of aerosols estimated by global models: AeroCom phase I results. *Journal of Geophysical Research: Atmospheres*, 117, D10201. https://doi.org/10.1029/2011JD016858

Koffi, B., Schulz, M., Bréon, F. -M., Dentener, F., Steensen, B. M., Griesfeller, J., et al. (2016). Evaluation of the aerosol vertical distribution in global aerosol models through comparison against CALIOP measurements: AeroCom phase II results. *Journal of Geophysical Research: Atmospheres*, 121, 7254-7283. https://doi.org/10.1002/2015JD024639

Lampilahti, J., Leino, K., Manninen, A., Poutanen, P., Franck, A., Peltola, M., et al. (2021). Aerosol particle formation in the upper residual layer. *Atmospheric Chemistry and Physics*, 21(10), 7901–7915. https://doi.org/10.5194/acp-21-7901-2021

Lareau, N. P., Zhang, Y., Klein, S. A. (2018). Observed boundary layer controls on shallow cumulus at the ARM Southern Great Plains Site. *Journal of the Atmospheric Sciences*, 75(7), 2235–2255. https://doi.org/10.1175/jas-d-17-0244.1

Lee, G., Lee, Y. G., Jeong, E., Ho, C. -H. (2021). Roles of meteorological factors in inter-regional variations of fine and coarse PM concentrations over the Republic of Korea. *Atmospheric Environment*, 264, 118706. https://doi.org/10.1016/j.atmosenv.2021.118706

Lee, H. -J., Jo, H. -Y., Kim, S. -W., Park, M. -S., Kim, C. -H. (2019). Impacts of atmospheric vertical structures of transboundary aerosol transport from China to South Korea. *Scientific Reports*, 9, 13040. https://doi.org/10.1038/s41598-019-49691-z

Lee, H. -J., Jo, H. -Y., Song, C. -K., Jo, Y. -J., Park, S. -Y., Kim, C. -H. (2020). Sensitivity of simulated $PM_{2.5}$ concentrations over northeast Asia to different secondary organic aerosol modules during the KORUS-AQ campaign. *Atmosphere*, 11, 1004. https://doi.org/10.3390/atmos11091004

Lee, J., Hong, J.-W., Lee, K., Hong, J., Velasco, E., Lim, Y. J., et al. (2019). ceilometer monitoring of boundary-layer height and its application in evaluating the dilution effect on air pollution. *Boundary-Layer Meteorology*, 172(3), 435–455. https://doi.org/10.1007/s10546-019-00452-5

Lee, S., Ho, C. -H., Choi, Y.-S. (2011). High-$PM_{10}$ concentration episodes in Seoul, Korea: Background sources and related meteorological conditions. *Atmospheric Environment*, 45(39), 7240–7247. https://doi.org/10.1016/j.atmosenv.2011.08.071

Lee, S., Kim, J., Choi, M., Hong, J., Kim, H., Eck, T. F., et al. (2019). Analysis of long-range transboundary transport (LRTT) effect on Korean aerosol pollution during the KORUS-AQ campaign. *Atmospheric Environment,* 204, 53-67. https://doi.org/10.1016/j.atmosenv.2019.02.020

Lee, S., Kim, M., Kim, S. -Y., Lee, D. -W., Lee, H., Kim, J., et al. (2021). Assessment of long-range transboundary aerosols in Seoul, South Korea from Geostationary Ocean Color Imager (GOCI) and ground-based observations. *Environmental Pollution*, 269, 115924. https://doi.org/10.1016/j.envpol.2020.115924

Lennartson, E. M., Wang, J., Gu, J., Garcia, L. C., Ge, C., Gao, M., et al. (2018). Diurnal variation of aerosol optical depth and $PM_{2.5}$ in South Korea: a synthesis from AERONET, satellite (GOCI), KORUS-AQ observation, and the WRF-Chem model. *Atmospheric Chemistry and Physics,* 18, 15125-15144. https://doi.org/10.5194/acp-18-15125-2018

Li, J., Zhang, Z., Wu, Y., Tao, J., Xia, Y., Wang, C., Zhang, R. (2021). Effects of chemical compositions in fine particles and their identified sources on hygroscopic growth factor during dry season in urban Guangzhou of South China. *Science of the Total Environment*, 801, 149749. https://doi.org/10.1016/j.scitotenv.2021.149749

Li, S., Garay, M. J., Chen, L., Rees, E., Liu, Y. (2013). Comparison of GEOS-Chem aerosol optical depth with AERONET and MIST data over the contiguous United States. *Journal of Geophysical Research: Atmospheres*, 118, 11228-11241. DOI:10.1002/jgrd.50867

Li, Z., Li, K., Li, D., Yang, J., Xu, H., Goloub, P. (2016). Simple transfer calibration method for a Cimel Sun-Moon photometer: calculating lunar calibration coefficients from Sun calibration constants. *Applied Optics*, 55, 7624-7630. https://doi.org/10.1364/AO.55.007624

Lin, C., Li, Y., Yuan, Z., Lau, A. K. H., Li, C., Fung, J. C. H. (2015). Using satellite remote sensing data to estimate the high-resolution distribution of

ground-level $PM_{2.5}$. *Remote Sensing of Environment*, 156, 117–128. https://doi.org/10.1016/j.rse.2014.09.015

Liu, Z., Sugimoto, N., Murayama, T. (2002). Extinction-to-backscatter ratio of Asian dust observed by high-spectral-resolution lidar and Raman lidar. *Applied Optics*, 41, 2760-2767. https://doi.org/10.1364/AO.41.002760

Lothon, M., Lohou, F., Pino, D., Couvreux, F., Pardyjak, E. R., Reuder, J., et al. (2014). The BLLAST field experiment: Boundary-Layer Late Afternoon and Sunset Turbulence. Atmospheric Chemistry and Physics, 14, 10931-10960. https://doi.org/10.5194/acp-14-10931-2014

Ma, X., Yu, F., Quass, J. (2014). Reassessment of satellite-based estimate of aerosol climate forcing. *Journal of Geophysical Research: Atmospheres*, 119, 10394-10409. Doi:10.1002/2014JD021670

Ma, Q., Wu, Y., Zhang, D., Wang, X., Xia, Y., Liu, X., et al. (2017). Roles of regional transport and heterogeneous reactions in the $PM_{2.5}$ increase during winter haze episodes in Beijing. *Science of the Total Environment*, 599-600, 246-253. https://doi.org/10.1016/j.scitotenv.2017.04.193

Manning, M. I., Martin, R. V., Hasenkopf, C., Flasher, J., Li, C. (2018). Diurnal Patterns in Global Fine Particulate Matter Concentration. *Environmental Science and Technology Letters*, 5(11), 687-691. https://doi.org/10.1021/acs.estlett.8b00573

Manninen, A. J., Marke, T., Tuononen, M., O'Connor, E. J. (2018). Atmospheric Boundary Layer Classification with Doppler Lidar. *Journal of Geophysical Research: Atmospheres*, 123: 8172-8189. https://doi.org/10.1029/2017JD028169

Marinescu, P. J., Heever, S. C. v. d., Saleeby, S. M., Kreidenweis, S. M., DeMott, P. J. (2017). The Microphysical Roles of Lower-Tropospheric versus Midtropospheric Aerosol Particles in Mature-Stage MCS Precipitation. *Journal of Atmospheric Sciences*, 74, 3657-3678. https://doi.org/10.1175/JAS-D-16-0361.1

McHardy, T. M., Zhang, J., Reid, J. S., Miller, S. D., Hyer, E. J., Kuehn, R. E. (2015). An improved method for retrieving nighttime aerosol optical thickness from the VIIRS Day/Night Band. *Atmospheric Measurement Techniques*, 8, 4773-4783. https://doi.org/10.5194/amt-8-4773-2015

Ministry of Environment of Korea, National Institute of Environmental Research. (2022). Guidelines for Installation and Operation of Air Pollution Monitoring Network (Korean).

https://www.airkorea.or.kr/web/board/3/769/?pMENU_NO=145. Accessed 23 July 2023.

Mishra, S., Tripathi, S. N., Kanawade, V. P., Haslett, S. L., Dada, L., Ciarelli, G., et al. (2023). Rapid night-time nanoparticle growth in Delhi driven by biomass-burning emissions. *Nature Geoscience*, 16, 224–230, https://doi.org/10.1038/s41561-023-01138-x

Müller, D., Ansmann, A., Mattis, I., Tesche, M., Wandinger, U., Althausen, D., Pisani, G. (2007). Aerosol-type-dependent lidar ratios observed with Raman lidar. *Journal of Geophysical Research*, 112, D16202. https://doi.org/10.1029/2006JD008292

Murayama, T., Masonis, S. J., Redemann, J., Anderson, T. L., Schmid, B., Livingston, J. M., et al. (2003). An intercomparison of lidar-derived aerosol optical properties with airborne measurements near Tokyo during ACE-Asia. *Journal of Geophysical Research*, 108, (D23) 8651. https://doi.org/10.1029/2002JD003259

Myhre, G., Samset, B.H., Schulz, M., Balkanske, Y., Bauer, S., Berntsen, T.K., et al. (2013). Radiative forcing of the direct aerosol effect from AeroCom Phase II simulations. *Atmospheric Chemistry and Physics*, 13, 1853-1877. https://doi.org/10.5194/acp-13-1853-2013

Nam, J., Kim, S. -W., Park, R. J., Park, J. -S., Park, S. S. (2018). Changes in column aerosol optical depth and ground-level particulate matter concentration over East Asia. *Air Quality, Atmosphere and Health*, 11(1), 49–60. https://doi.org/10.1007/s11869-017-0517-5

Nemuc, A., Vasilescu, J., Talianu, C., Belegante, L., Nicolae, D. (2013). Assessment of aerosol's mass concentrations from measured linear particle depolarization ratio (vertically resolved) and simulations. *Atmospheric Measurement Techniques*, 6, 3243-3255. https://doi.org/10.5194/amt-6-3243-2013

Nishizawa, T., Sugimoto, N., Matsui, I., Shimizu, A., Higurashi, A., Jin, Y. (2016). The Asian Dust and Aerosol Lidar Observation Network (AD-NET): Strategy and Progress, EPJ Web of Conferences 119 19001, doi: 10./1051/epjconf/201611919001

Oak, Y. J., Park, R. J., Schroeder, J. R., Crawford, J. H., Blake, D. R., Weinheimer, A. J., et al. (2019). Evaluation of simulated $O_3$ production efficiency during the KORUS-AQ campaign: Implications for anthropogenic NOx emissions in Korea. *Elementa Science of the Anthropocene*, 7, 56. https://doi.org/10.1525/elementa.394

Omar, A. H., Winker, D. M., Kittaka, C., Vaughan, M. A., Liu, Z., Hu, Y., et al. (2009). The CALIPSO Automated Aerosol Classification and Lidar Ratio Selection Algorithm. *Journal of Atmospheric and Oceanic Technology*, 26, 1994-2014. https://doi.org/10.1175/2009JTECHA1231.1

Painemal, D., Clayton, M., Ferrare, R., Burton, S., Josset, D., Vaughan, M. (2019). Novel aerosol extinction coefficients and lidar ratios over the ocean from CALIPSO-CloudSat: evaluation and global statistics. *Atmospheric Measurement Techniques*, 12, 2201-2217. https://doi.org/10.5194/amt-12-2201-2019

Pal, S., Lee, T. R., Phelps, S., De Wekker, S. F. J. (2014). Impact of atmospheric boundary layer depth variability and wind reversal on the diurnal variability of aerosol concentration at a valley site. *Science of the Total Environment*, 496, 424-434, doi:10.1016/j.scitotenv.2014.07.067

Pan, X. L., Yan, P., Tang, J., Ma, J. Z., Wang, Z. F., Gbaguidi, A., Sun, Y. L. (2009). Observational study of influence of aerosol hygroscopic growth on scattering coefficient over rural area near Beijing mega-city. *Atmospheric Chemistry and Physics*, 9, 7519–7530, https://doi.org/10.5194/acp-9-7519-2009

Papagiannopoulos, N., Mona, L., Alados-Arboldas, L., Amiridis, V., Baars, H., Binietoglou, I., et al. (2016). CALIPSO climatological products: evaluation and suggestions from EARLINET. *Atmospheric Chemistry and Physics*, 16, 2341-2357. https://doi.org/10.5194/acp-16-2341-2016

Pappalardo, G., Amodeo, A., Apituley, A., Comeron, A., Freudenthaler, V., Linné, H., et al. (2014). EARLINET: towards an advanced sustainable European aerosol lidar network, *Atmospheric Measurement and Techniques*., 7, 2389–2409, https://doi.org/10.5194/amt-7-2389-2014

Park, M. E., Song, C. H., Park, R. S., Lee, J., Kim, J., Lee, S., et al. (2014). New approach to monitor transboundary particulate pollution over Northeast Asia. *Atmospheric Chemistry and Physics*, 14(2), 659–674. https://doi.org/10.5194/acp-14-659-2014

Park, S., Shin, M., Im, J., Song, C. -K., Choi, M., Kim, J., et al. (2019). Estimation of ground-level particulate matter concentrations through the synergistic use of satellite observations and process-based models over South Korea. *Atmospheric Chemistry and Physics*, 19, 1097-1113. https://doi.org/10.5194/acp-19-1097-2019

Park, S., Kim, S. -W., Park, M. -S., Song, C. -K. (2018). Measurement of Planetary Boundary Layer Winds with Scanning Doppler Lidar. *Remote Sensing*, 10, 1261. doi: 10.3390/rs10081261

Park, S., Kim, S. -W., Lin, N. -H., Pani, S. K., Sheridan, P. J., Andrews, E. (2019). Variability of Aerosol Optical Properties Observed at a Polluted Marine (Gosan, Korea) and a High-altitude Mountain (Lulin, Taiwan) Site in the Asian Continental Outflow. *Aerosol Air Quality Research*, 19, 1272-1283. https://doi.org/10.4209/aaqr.2018.11.0416

Park, S., Kim, M. -H., Yeo, H., Shim, K., Lee, H. -J., Kim, C. -H., Song, C. -K., Park, M. -S., Shimizu, A., Nishizawa, T., Kim, S. -W. (2022). Determination of mixing layer height from co-located lidar, ceilometer and wind Doppler lidar measurements: Intercomparison and implications for $PM_{2.5}$ simulations. *Atmospheric Pollution Research*, 12(2), 101310. https://doi.org/10.1016/j.apr.2021.101310

Pearson, G., Davies, F., Collier, C. (2010). Remote sensing of the tropical rain forest boundary layer using pulsed Doppler lidar. *Atmospheric Chemistry and Physics*, 10, 5891–5901. https://doi.org/10.5194/acp-10-5891-2010

Pérez-Ramírez, D., Whiteman, D. N., Veselovskii, I., Ferrare, R., Titos, G., Granados-Muñoz, M. J., et al. (2021). Spatiotemporal changes in aerosol properties by hygroscopic growth and impacts on radiative forcing and heating rates during DISCOVER-AQ 2011. *Atmospheric Chemistry and Physics*, 21(15), 12021–12048. https://doi.org/10.5194/acp-21-12021-2021

Peterson, E. A., Hyer, E. J., Han, S. -O., Crawford, J. H., Park, R. J., Holz, R., et al. (2019). Meteorology influencing springtime air quality, pollution transport, and visibility in Korea. *Elementa Science of the Anthropocene*, 7, 57. https://doi.org/10.1525/elementa.395

Phillips, C. (2019). Aerosol optical properties in Seoul measured using the UW-Madison HSRL. Masters Thesis, University of Wisconsin-Madison.

Quan, J., Gao, Y., Zhang, Q., Tie, X., Cao, J., Han, S., et al. (2013). Evolution of planetary boundary layer under different weather conditions, and its impact on aerosol concentrations. *Particuology*, 11, 34–40. https://doi.org/10.1016/j.partic.2012.04.005

Ramanathan, V., Crutzen, P.J., Kiehl, J.T., Rosenfeld, D. (2001). Aerosols, Climate, and the Hydrological cycle. *Science*, 294, 2119-2124. DOI: 10.1126/science.1064034

Reid, J. S., Kuehn, R. E., Holz, R. E., Eloranta, E. W., Kaku, K. C., Kuang, S., et al. (2017). Ground-based High Spectral Resolution Lidar observation of aerosol vertical distribution in the summertime Southeast United States. *Journal of Geophysical Research: Atmospheres,* 122, 2970-3004. https://doi.org/10.1002/2016JD025798

Rogers, R. R., Vaughan, M. A., Hostetler, C. A., Burton, S. P., Ferrare, R. A., Young, S. A., et al. (2014). Looking through the haze: evaluating the CALIPSO level 2 aerosol optical depth using airborne high spectral resolution lidar data. *Atmospheric Measurement Techniques*, 7, 4317-4340. https://doi.org/10.5194/amt-7-4317-2014

Sasano, Y., Browell, E. V. and Ismail, S. (1985). Error caused by using a constant extinction/backscattering ratio in the lidar solution. *Applied Optics*, 24(22), 3929-3932. https://doi.org/10.1364/AO.24.003929

Saide, P. E., Gao, M., Lu, Z., Goldberg, D. L., Streets, D. G., Woo, J.-H., et al. (2020). Understanding and improving model representation of aerosol optical properties for a Chinese haze event measured during KOURS-AQ. *Atmospheric Chemistry and Physics*, 20(11), 6455–6478. https://doi.org/10.5194/acp-20-6455-2020

Schotland, R. M., Sassen, K., Stone, R. (1971). Observations by Lidar of Linear Depolarization Ratios for Hydrometeors. *Journal of Applied Meteorology and Climatology*, 10, 1011-1017. https://doi.org/10.1175/1520-0450(1971)010<1011:OBLOLD>2.0.CO;2

Schuster, G., Toth, T., Trepte, C., Chin, M., Bian, H., Kim, D., et al. (2022). Mapping Modeled Aerosol Species to Measured Lidar Ratios for the MIRA Project, The 30th International Laser Radar Conference, 26 June-1 July 2022, Montana, USA, https://science.larc.nasa.gov/mira-wg/

Schutgens, N. A. J., Partridge, D. G. and Stier, P. (2016). The importance of temporal collocation for the evaluation of aerosol models with observations. *Atmospheric Chemistry and Physics*, 16, 1065-1079. doi:10.5196/acp-16-1065-2016.

Schween, J. H., Hirsikko, A., Löhnert, U., Crewell, S. (2014). Mixing-layer height retrieval with ceilometer and Doppler lidar: from case studies to long-term assessment. *Atmospheric Measurement Techniques*, 7, 3685–3704. https://doi.org/10.5194/amt-7-3685-2014

Seibert, P., Beyrich, F., Gryning, S.E., Joffre, S., Rasmussen, A., Tercier, P. (2000). Review and intercomparison of operational methods for the

determination of the mixing height. *Atmospheric Environment*, 34 (7), 1001–1027. https://doi.org/10.1016/S1352-2310(99)00349-0

Seo, J., Kim, J. Y., Youn, D., Lee, J. Y., Kim, H., Lim, Y. B., et al. (2017). On the multiday haze in the Asian continental outflow: the important role of synoptic conditions combined with regional and local sources. *Atmospheric Chemistry and Physics*, 17, 9311-9332. https://doi.org/10.5194/acp-17-9311-2017

Seo, S., Kim, J., Lee, H., Jeong, U., Kim, W., Holben, B. N., et al. (2015). Estimation of $PM_{10}$ concentrations over Seoul using multiple empirical models with AERONET and MODIS data collected during the DRAGON-Asia campaign. *Atmospheric Chemistry and Physics*, 15, 319-334. https://doi.org/10.5194/acp-15-319-2015

Shim, K., Kim, M. -H., Lee, H. -J., Nishizawa, T., Shimizu, A., Kobayashi, H., et al. (2022). Exacerbation of $PM_{2.5}$ concentration due to unpredictable weak Asian dust storm: A case study of an extraordinarily long-lasting spring haze episode in Seoul, Korea. *Atmospheric Environment*, 287, 119261. https://doi.org/10.1016/j.atmosenv.2022.119261

Shimizu, A., Sugimoto, N., Matsui, I., Arao, K., Uno, I., Murayama, T., et al. (2004). Continuous observations of Asian dust and other aerosols by polarization lidars in China and Japan during ACE-Asia. *Journal of Geophysical Research*, 109, D19S17. https://doi.org/10.1029/2002JD003253

Shindell, D. T., Lamarque, J.-F., Schulz, M., Flanner, M., Jiao, C., Chin, M., et al. (2013). Radiative forcing in the ACCMIP historical and future climate simulations. *Atmospheric Chemistry and Physics*, 13, 2939–2974, https://doi.org/10.5194/acp-13-2939-2013.

Sicard, P., Crippa, P., De Marco, A., Castruccio, S., Giani, P., Cuesta, J., et al. (2021). High spatial resolution WRF-Chem model over Asia: physics and chemistry evaluation. *Atmospheric Environment*, 244, 118004, https://doi.org/10.1016/j.atmosenv.2020.118004.

Smirnov, A., Holben, B. N., Eck, T. F., Dubovik, O., Slutsker, I. (2000). Cloud-Screening and Quality Control Algorithms for the AERONET Database. *Remote Sensing of Environment*, 73, 337-349. https://doi.org/10.1016/S0034-4257(00)00109-7

Stull, R. B. (1998). An Introduction to Boundary layer Meteorology, Kluwer Academic Publishers, Dordrecht, The Nederlands.

Su, T., Li, J., Li, C., Lau, A. K. -H., Yang, D., Shen, C. (2017). An intercomparison of AOD converted $PM_{2.5}$ concentrations using different approaches for

estimating aerosol vertical distribution. *Atmospheric Environment*, 166, 531–542. https://doi.org/10.1016/j.atmosenv.2017.07.054

Su, T., Li, Z., Kahn, R. (2018). Relationships between the planetary boundary layer height and surface pollutants derived from lidar observations over China: regional pattern and influencing factors. *Atmospheric Chemistry and Physics*, 18, 15921–15935. https://doi.org/10.5194/acp-18-15921-2018

Sugimoto, N. and Lee, C. H. (2006). Characteristics of dust aerosols inferred from lidar depolarization measurements at two wavelengths. *Applied Optics*, 45(28), 7468-7474. https://doi.org/10.1364/AO.45.007468

Sugimoto, N., Shiumizu, A., Matsui, I., Nishikawa, M. (2016). A method for estimating the fraction of mineral dust in particulate matter using $PM_{2.5}$-to-$PM_{10}$ ratios, *Particuology*, 28, 114-120. https://doi.org/10.1016/j.partic.2015.09.005

Tangborn, A., Demoz, B., Carroll, B. J., Santanello, J., Anderson, J. L. (2021). Assimilation of lidar planetary boundary layer height observations. *Atmospheric Measurement Techniques*, 14, 1099–1110. https://doi.org/10.5194/amt-14-1099-2021

Tesche, M., Ansmann, A., Müller, D., Althausen, D., Mattis, I., Heese, B., et al. (2009). Vertical profiling of Saharan dust with Raman lidars and airborne HSRL in southern Morocco during SAMUM. *Tellus B*., 61: 144-164. https://doi.org/10.1111/j.1600-0889.2008.00390.x

Tian, P., Liu, D., Zhao, D., Yu, C., Liu, Q., Huang, M., et al. (2020). In situ vertical characteristics of optical properties and heating rates of aerosol over Beijing. *Atmospheric Chemistry and Physics*, 20, 2603-2622. https://doi.org/10.5194/acp-20-2603-2020

Titos, G., Burgos, M. A., Zieger, P., Alados-Arboledas, L., Baltensperger, U., Jefferson, A., et al. (2021). A global study of hygroscopicity-driven light-scattering enhancement in the context of other in situ aerosol optical properties, *Atmospheric Chemistry and Physics*, 21, 13031-13050. https://doi.org/10.5194/acp-21-13031-2021

Toth, T. D., Zhang, J., Campbell, J. R., Hyer, E. J., Reid, J. S., Shi, Y., Westphal, D. L. (2014). Impact of data quality and surface-to-column representativeness on the $PM_{2.5}$ / satellite AOD relationship for the contiguous United States. *Atmospheric Chemistry and Physics*, 14, 6049–6062, https://doi.org/10.5194/acp-14-6049-2014

Toth, T. D., Zhang, J., Reid, J. S., Vaughan, M. A. (2019). A bulk-mass-modeling-based method for retrieving particulate matter pollution using CALIOP observations. *Atmospheric Measurement Techniques,* 12, 1739-1754. https://doi.org/10.5194/amt-12-1739-2019

Träumner, K., Kottmeier, C., Corsmeier, U., Wieser, A., (2011). Convective Boundary-Layer Entrainment: Short Review and Progress using Doppler Lidar. *Boundary-Layer Meteorology*, 141, 369-391. https://doi.org/10.1007/s10546-011-9657-6

Tucker, S. C., Brewer, W. A., Banta, R. M., Senff, C. J., Sandberg, S. P., Law, D. C., et al. (2009). Doppler Lidar Estimation of Mixing Height Using Turbulence, Shear, and Aerosol Profiles. *Journal of Atmospheric and Oceanic Technology*, 26, 673-688. https://doi.org/10.1175/2008JTECHA1157.1

Uchiyama, A., Shiobara, M., Kobayashi, H., Matsunaga, T., Yamazaki, A., Inei, K., et al. (2019). Nocturnal aerosol optical depth measurements with modified sky radiometer POM-02 using the moon as a light source. *Atmospheric Measurement Techniques*, 12, 6465-6488. https://doi.org/10.5194/amt-12-6465-2019

Ukhov, A., Ahmadov, R., Grell, G., Stenchikov, G. (2021). Improving dust simulations in WRF-Chem v4.1.3 coupled with the GOCART aerosol module. *Geoscientific Model Development*, 14, 473–493. https://doi.org/10.5194/gmd-14-473-2021

van Donkelaar, A., Martin, R. V., Spurr, R. J., Burnett, R. T. (2015). High-resolution satellite-derived $PM_{2.5}$ from optimal estimation and geographically weighted regression over North America. *Environmental Science and Technology*. 49, 10482-10491. https://doi.org/10.1021/acs.est.5b02076

Wang, H., Wang, H., Lu, X., Lu, K., Zhang, L., Tham, Y. J., et al. (2023). Increased night-time oxidation over China despite widespread decrease across the globe. *Nature Geoscience*, 16, 217–223, https://doi.org/10.1038/s41561-022-01122-x

Ware, J., Kort, E. A., DeCola, P., Duren, R. (2018). Aerosol lidar observations of atmospheric mixing in Los Angeles: climatology and implications for greenhouse gas observations. *Journal of Geophysical Research: Atmospheres*, 121, 9862–9878. doi: 10.1002/2016JD024953

Welton, E. J., Campbell, J. R., Lewis, J. R., Lolli, S., Stewart, S. A., Belcher, L. R., et al. (2021). "The NASA Micro Pulse Lidar Network (MPLNET): Early Results from Development of Diurnal Climatologies," *2021 IEEE International*

*Geoscience and Remote Sensing Symposium IGARSS*, Brussels, Belgium, 2021, pp. 1432-1433.

Willeke, K., and Brockmann, J. E. (1977). Extinction coefficients for multimodal atmospheric particle size distributions. *Atmospheric Environment* (1967), 11(10), 995-999. https://doi.org/10.1016/0004-6981(77)90029-4

Winker, D. M., Vaughan, M. A., Omar, A., Hu, Y., Powell, K. A. (2009). Overview of the CALIPSO Mission and CALIOP Data Processing Algorithm. *Journal of Atmospheric and Oceanic Technology,* 26, 2310-2323. https://doi.org/10.1175/2009JTECHA1281.1

Winker, D. M., Tackett, J. L., Getzewich, B. J., Liu, Z. Vaughan, M. A., Rogers, R. R. (2013). The global 3-D distribution of tropospheric aerosols as characterized by CALIOP. *Atmospheric Chemistry and Physics*, 13, 3345-3361. https://doi.org/10.5194/acp-13-3345-2013

Won, J. -G., Yoon, S. -C., Kim, S. -W., Jefferson, A., Dutton, E. G., Holben, B. N. (2004). Estimations of Direct Radiative Forcing of Asian Dust Aerosols with Sun/Sky Radiometer and Lidar Measurements at Gosan, Korea. *Journal of the Meteorological Society of Japan*, 82(1), 115-130. https://doi.org/10.2151/jmsj.82.115

Wu, T., Li, Z., Chen, J., Wang, Y., Wu, H., Jin, X., et al. (2020). Hygroscopicity of Different Types of Aerosol Particles: Case Studies Using Multi-Instrument Data in Megacity Beijing, China. *Remote Sensing*, 12(5), 785. https://doi.org/10.3390/rs12050785

Wu, Y., de Graaf, M. and Menenti, M. (2016). The Sensitivity of AOD Retrieval to Aerosol Type and Vertical Distribution over Land with MODIS Data. *Remote Sensing*, 8, 765. https://doi.org/10.3390/rs8090765

Xu, J. -W., Martin, R. V., van Donkelaar, A., Kim, J., Choi, M., Zhang, Q., et al. (2015). Estimating ground-level $PM_{2.5}$ in eastern China using aerosol optical depth determined from the GOCI satellite instrument. *Atmospheric Chemistry and Physics*, 15, 13133-13144. https://doi.org/10.5194/acp-15-13133-2015

Yahya, K., Campbell, P., Zhang, Y. (2017). Decadal application of WRF/chem for regional air quality and climate modeling over the U.S. under the representative concentration pathways scenarios. Part 2: current vs. future simulations. *Atmospheric Environment*, 152, 584–604. https://doi.org/10.1016/j.atmosenv.2016.12.029

Yan, X., Shi, W., Li, Z., Li, Z., Luo, N., Zhao, W., et al. (2017). Satellite-based $PM_{2.5}$ estimation using fine-mode aerosol optical thickness over China.

*Atmospheric Environment*, 170, 290-302. https://doi.org/10.1016/j.atmosenv.2017.09.023

Yang, S. H., Jeong, J. I., Park, R. J., Kim, M. J. (2020). Impact of meteorological changes on particulate matter and aerosol optical depth in Seoul during the Months of June over recent decades. Atmosphere, 11(12), 1282. https://doi.org/10.3390/atmos11121282

Yeo, H., Kim, S. -W., Lee, C., Kim, D., Kim, B. -G., Kim, S., et al. (2016). The KALION Automated Aerosol Type Classification and Mass Concentration Calculation Algorithm. *Korean Journal of Remote Sensing,* 32(2), 119-131. (In Korean with English Abstract).

Yerramilli, A., Challa, V. S., Dodla, V. B. R., Dasari, H. P., Young, J. H., Patrick, C., et al. (2010). Simulation of surface ozone pollution in the central gulf coast region using WRF/chem model: sensitivity to PBL and land surface physics. *Advances in Meteorology*, 2010, 319138 https://doi.org/10.1155/2010/319138.

Yoo, J. -M., Lee, Y. -R., Kim, D., Jeong, M. -J., Stockwell, W. R., Kundu, P. K., et al. (2014). New indices for wet scavenging of air pollutants ($O_3$, CO, $NO_2$, $SO_2$, and $PM_{10}$) by summertime rain. *Atmospheric Environment*, 82, 226-237. https://doi.org/10.1016/j.atmosenv.2013.10.022

Yoon, S. -C., Kim, S. -W., Choi, S. -J., Choi, I. -J. (2010). Regional-scale Relationship Between Aerosol and Summer Monsoon Circulation, and Precipitation Over Northeast Asia. *Asia-Pacific Journal of Atmospheric Sciences*, DOI:10.1007/s13143-010-0018-X

Young, S. A., and Vaughan, M. A. (2009). The Retrieval of Profiles of Particulate Extinction from Cloud-Aerosol Lidar Infrared Pathfinder Satellite Observations (CALIPSO) Data: Algorithm Description. *Journal of Atmospheric and Oceanic Technology*, 26, 1105-1119. https://doi.org/10.1175/2008JTECHA1221.1

Young, S. A., Vaughan, M. A., Garnier, A., Tackett, J. L., Lambeth, J. D., Powell, K. A. (2018). Extinction and optical depth retrievals for CALIPSO's Version 4 data release. *Atmospheric Measurement Techniques*, 11, 5701-5727. https://doi.org/10.5194/amt-11-5701-2018

Zhai, S., Jacob, D. J., Brewer, J. F., Li, K., Moch, J. M., Kim, J., et al. (2021). Relating geostationary satellite measurements of aerosol optical depth (AOD) over East Asia to fine particulate matter ($PM_{2.5}$): insights from the KORUS-AQ aircraft campaign and GEOS-Chem model simulations. *Atmospheric*

*Chemistry and Physics*, 21, 16775-16791. https://doi.org/10.5194/acp-21-16775-2021

Zhan, B., Zhong, H., Chen, H., Chen, Y., Li, X., Wang, L., et al. (2021). The roles of aqueous-phase chemistry and photochemical oxidation in oxygenated organic aerosols formation. *Atmospheric Environment*, 266, 118738. https://doi.org/10.1016/j.atmosenv.2021.118738

Zhang, J., Reid, J. S., Westphal, D. L., Baker, N. L., Hyer, E. J. (2008). A system for operational aerosol optical depth data assimilation over global oceans. *Journal of Geophysical Research: Atmospheres*, 113, D10208. https://doi.org/10.1029/2007JD009065

Zhang, Y., Yu, H., Eck, T. F., Smirnov, A., Chin, M., Remer, L. A., et al. (2012). Aerosol daytime variations over North and South America derived from multiyear AERONET measurements. *Journal of Geophysical Research*, 117, D05211. https://doi.org/10.1029/2011JD017242

Zhao, H., Che, H., Xia, X., Wang, Y., Wang, H., Wang, P., et al. (2019). Climatology of mixing layer height in China based on multi-year meteorological data from 2000 to 2013. *Atmospheric Environment*, 213, 90–103. https://doi.org/10.1016/j.atmosenv.2019.05.047

Ziemba, L. D., Thornhill, K. L., Ferrare, R., Barrik, J., Beyersdorf, A. J., Chen, G., et al. (2013). Airborne observations of aerosol extinction by in situ and remote-sensing techniques: Evaluation of particle hygroscopicity. *Geophysical Research Letters*, 40, 471-422. https://doi.org/10.1029/2012GL054428

# 국문 초록

에어로졸의 광학적 특성과 질량 농도의 연직 분포에 대한 정보는 정확한 대기질 모의 및 예보와 에어로졸의 복사 및 기후 영향 평가에 있어서 매우 중요하다. 다양한 에어로졸 배출원과 복잡한 에어로졸의 이동 및 수송 경로로 인해, 라이다(Lidar)와 같은 지상 원격 관측자료가 연속적인 에어로졸의 연직 분포에 대한 직접적인 관측 자료를 제공하는데 있어서 쓰임새가 널리 알려져 있다. 하지만, 라이다 측정을 기반으로 에어로졸의 특성을 정확하게 파악하는데 있어서 필수인 지역에 따른 에어로졸의 유형별 구분과 유형별 특성에 대한 상세한 연구는 부족한 실정이다. 따라서, 본 연구에서는 에어로졸에 의한 환경 및 기후 효과에 대한 논의가 활발하게 이루어지고 있는 동아시아 중, 특히, 서울에서의 다수의 지상 기반 라이다 관측자료를 통해 에어로졸의 연직 분포와 광학적 특성을 조사하였다. 본 연구에서는 2016년 3월부터 2018년 1월까지 서울대학교에서 동시 관측을 수행한 고분광해상라이다(High Spectral Resolution Lidar; HSRL)와 미산란 라이다(Mie-scattering lidar) 관측자료를 활용하여 에어로졸의 유형별 라이다 상수와 질량 소산 효율을 산출하였다.

라이다 관측 자료를 기반으로 한 에어로졸의 유형 구분에 앞서, 본 연구에서는 신림 지상 관측소에서 관측된 $PM_{2.5}$와 $PM_{10}$

질량 농도를 사용하여 본 연구 기간 동안의 에어로졸 유형 구분을 수행하였다. 지상 $PM_{2.5}$와 $PM_{10}$ 자료를 바탕으로 에어로졸의 유형을 청정기원 에어로졸(이하 청정), 오염 입자(이하 오염), 황사, 황사와 오염 입자의 혼합된 에어로졸(이하 혼합)로 구분하였다. 이를 바탕으로 HSRL과 미산란 라이다 각각의 후방산란계수와 편광소멸도 관측자료와의 비교를 통하여 라이다 관측자료를 바탕으로 에어로졸의 유형 구분을 실시하였으며, 그 결과 HSRL에서 산출된 에어로졸 유형별 라이다 상수(532 nm)는 청정 에어로졸이 48 sr, 오염 에어로졸이 57 sr, 황사가 42 sr, 그리고 혼합 에어로졸이 49 sr으로 보고되었다. 이렇게 산출된 에어로졸 유형별 라이다 상수를 미산란 라이다 관측 자료에 적용하여 에어로졸 소산 계수를 산출하였다. 에어로졸의 유형구분이 필요 없는, 더 간단하고 보편적인 방법은 하나의 라이다 상수를 사용하여 에어로졸 소산계수를 산출하는 방법이다. 본 연구에서 적용한 에어로졸의 유형별 구분 및 유형별 라이다 상수를 적용한 결과, 일반적인 단일 라이다 상수를 이용했을 때보다 에어로졸 소산 계수의 현저한 개선을 확인할 수 있었다. 동시 관측을 수행한 HSRL의 소산 계수 측정값과 비교했을 때, 본 연구에서 사용한 방법이 에어로졸 소산 계수 오차를 $-0.026\ km^{-1}$에서 $-0.019\ km^{-1}$으로 줄였다. 이러한 7 $Mm^{-1}$의 소산 계수

오차 감소는 에어로졸 광학 두께(AOD)의 오차를 0.042 줄이는 효과이며, 이는 서울의 평균 에어로졸 광학 두께의 약 10%에 해당한다.

HSRL의 2016년 3월부터 2018년 1월까지의 에어로졸 소산계수 관측 결과를 이용하여 에어로졸 광학 두께의 시간적 변동성을 조사하고, 대기경계층(BL) 및 자유대기(FT)에 분포한 에어로졸이 에어로졸 광학 두께에 기여하는 정도를 추정하였다. HSRL에서 관측한 에어로졸 광학 두께는 서울대학교에서 동시 관측을 이룬 AERONET의 스카이라디오미터 관측값과 잘 일치하는 결과를 보였다(평균편차= −0.00, $R^2$ = 0.87). 야간 에어로졸 광학 두께는 주간에 비해 더 큰 평균과 표준 편차를 보여주었다(0.45 ± 0.47 대비 0.40 ± 0.29). 상대습도가 높은 습한 조건에서의 에어로졸의 흡습성 성장은 야간 에어로졸 광학 두께의 상대적 증가에 중요한 영향을 미치는 요인인 것으로 확인되었다. 에어로졸 광학 두께는 04시에 가장 높게 관측되었으며, 13시에 가장 낮게 관측되는 일변화를 보였다. 서울에서 관측되는 주간과 야간 에어로졸 광학 두께의 유의미한 차이로 인해 24시간 동안의 HSRL 측정과 AERONET 스카이라디오미터의 주간 측정에서 관측된 일일 평균 에어로졸 광학 두께에 상당한 격차가 발생하는 것으로 나타났다.

HSRL의 연직 측정을 활용하여 대기경계층(BL)과 자유대기층(FT) 내 에어로졸 광학 두께의 시간 변동성을 조사하였다. AOD의 일변동성과 달리, 대기경계층 내의 에어로졸 광학 두께($AOD_{BL}$)는 야간 동안에 낮고 14–15시에 최고값을 보이는 혼합층 높이와 더 비슷한 일변동성을 보였다. 하지만 혼합층 높이와 $AOD_{BL}$ 간의 낮은 상관관계($R^2$ = 0.06)는 혼합층의 높이가 $AOD_{BL}$의 유일한 결정 요인이 아니며, 대기경계층 내 에어로졸 농도가 혼합층의 높이와 매우 다른 시간적 변동성을 보인다는 것을 시사하였다. $AOD_{BL}$는 정오에 가장 크지만, BL 내 평균 에어로졸 소산 계수($AOD_{BL}$을 혼합층 높이로 나눈 값)는 낮에 낮은 값을 보여 이를 통해 대기경계층 내 활발한 난류로 인한 에어로졸 농도의 희석을 확인할 수 있었다. $AOD_{BL}$과 에어로졸 광학 두께 사이의 비율은 주간(42 ± 22%)보다 야간(27 ± 21%)에 더 큰 값을 보였다.

에어로졸 광학 두께는 여름, 봄, 가을, 겨울 순으로 크게 나타났다. 겨울철 평균 에어로졸 광학 두께가 가장 작게 관측된데 반해, 겨울철의 일평균 에어로졸 광학 두께의 최댓값이 다른 계절의 최대 일평균 에어로졸 광학 두께 값과 비슷하게 관측되었다. 이는 겨울동안 전반적으로 에어로졸 광학 두께가 낮지만, 에어로졸 광학 두께 값이 크게 관측되는 고농도 에어로졸

사례들이 빈번하게 발생함을 시사하는 결과다. 여름에는 $AOD_{BL}$과 $AOD_{FT}$도 크게 나타났으며, 이는 상대습도가 높은 환경에서 활발한 에어로졸의 흡습 성장으로 설명된다. 봄에는 $AOD_{FT}$와 $AOD_{FT}$ 대 에어로졸 광학 두께의 비가 크고, 2 km에서 6 km 사이의 편광 소멸도가 크게 나타나는 것으로 보아 빈번하게 서울 대기경계층 위로 지나가는 황사층의 영향으로 보인다.

서울 HSRL로 관측한 대기경계층 내 에어로졸의 평균 소산계수와 지표면 $PM_{10}$ 농도를 사용하여 에어로졸의 질량 소산 효율(Mass Extinction Efficiency, MEE)를 산출하였다. $PM_{10}$ MEE의 평균값과 중앙값은 각각 5.40 $m^2 g^{-1}$과 4.28 $m^2 g^{-1}$으로 나타났다. $PM_{2.5}$ 대 $PM_{10}$ 비율, 계절, 상대 습도, 그리고 에어로졸 유형에 따라 MEE는 큰 변동성이 보였다. 황사와 혼합 에어로졸은 흡습성이 낮은 성분들로 이루어져 있어 MEE와 상대 습도 간에 약한 상관관계가 확인되었지만, 오염과 청정 에어로졸들은 상대 습도가 증가함에 따라 MEE가 급격하게 성장하는 것을 확인할 수 있었다. 이러한 에어로졸 유형별, 그리고 상대 습도에 따른 MEE 값을 사용하는 것이 라이다 관측 자료로부터의 지표면 $PM_{10}$ 농도 산출물의 불확실성이 가장 낮게 나타났다(단일 MEE 값을 사용할 때의 평균표준편차(Mean Normalized Bias; MNB)가 10.6%에서 3.5%로 감소). 본 연구에서 제시한 에어로졸의 유형 및 상대

습도에 따른 MEE 값의 조견표(Lookup Table)을 사용하여 월별 $PM_{10}$ 농도 프로파일을 추출하였다. 에어로졸 소산 계수의 계절 변동성과는 달리, $PM_{10}$ 농도는 봄에 가장 크게 나타났으며, 이는 에어로졸의 광학적 특성과 질량 농도 사이의 차이를 명확하게 보이는 결과다.

**핵심어:** 고분광해상 라이다, 미산란 라이다, 라이다 상수, 질량 소산 효율, 에어로졸

**학 번:** 2017-34942